

Quasi Three-Dimensional Flutter Analysis of Single-row STCF4

Turbine Blade Cascade in Supersonic Flow

by

Jiadong Yin

Department of Mechanical Engineering and Materials Science  
Duke University

Date: \_\_\_\_\_

Approved:

\_\_\_\_\_  
Robert E. Kielb, Supervisor

\_\_\_\_\_  
Earl H. Dowell

\_\_\_\_\_  
Donald B. Bliss

\_\_\_\_\_  
Wilkins Aquino

Thesis submitted in partial fulfillment of the  
requirements for the degree of  
Master of Science in the Department of  
Mechanical Engineering and Materials Science  
in the Graduate School of  
Duke University

2013

ABSTRACT

Quasi Three-Dimensional Flutter Analysis of Single-row STCF4

Turbine Blade Cascade in Supersonic Flow

by

Jiadong Yin

Department of Mechanical Engineering and Materials Science  
Duke University

Date: \_\_\_\_\_

Approved:

\_\_\_\_\_  
Robert E. Kielb, Supervisor

\_\_\_\_\_  
Earl H. Dowell

\_\_\_\_\_  
Donald B. Bliss

\_\_\_\_\_  
Wilkins Aquino

An abstract of a thesis submitted in partial  
fulfillment of the requirements for the degree of  
Master of Science in the Department of  
Mechanical Engineering and Materials Science  
in the Graduate School of  
Duke University

2013

Copyright by  
Jiadong Yin  
2013

## **Abstract**

Modern aircraft gas engines and power turbines are frequently subject to the high cycle fatigue (HCF) which can lead to structural failure of turbomachinery blades. HCF in turbomachinery can be caused by many flow induced problems, among which flutter, a self-excited and self-sustained dynamic instability, is one of the most important and cumbersome phenomena. Therefore, a thorough understanding of the mechanism of flutter in turbomachinery is necessary to avoid the HCF issues.

In this work, firstly a numerical approach is applied to analyze the flutter stability of a quasi 3D single-row standard configuration 4 (STCF4) blade cascade in supersonic flow. Then, the calculated results will be compared to the results from other unsteady Computational Fluid Dynamics (CFD) solver and the experimental data based on the published paper. In the last part of this thesis, different initial conditions or boundary conditions will be applied to investigate the sensitivity of the structure in terms of flutter stability to the variation of the vibration frequency and the pressure ratio.

# Contents

Abstract .....	iv
List of Tables.....	vii
List of Figures .....	viii
Nomenclature .....	xiii
Acknowledgements .....	xvi
1 Introduction and Motivation .....	1
2 Problems Outline.....	3
3 Theoretical Background.....	6
3.1 Wing flutter .....	6
3.2 Flutter in Turbomachinery .....	10
3.2.1 Key Parameters affecting Turbomachinery Flutter .....	10
3.2.2 Types of Flutter in Turbomachinery.....	14
3.2.3 Flutter Stability .....	17
4 Numerical Approach in turbomachinery research.....	21
4.1 Governing Equation.....	21
4.2 Flow Field Kinematics in Frequency Domain .....	23
4.3 The Harmonic Balance Equations .....	25
4.4 The Unsteady Turbomachinery Code MUSTANG_HB.....	26
4.4.1 Periodic Boundary Conditions.....	28
5 Test Case & Blade Cascade Setting .....	29

6	Results and Analysis .....	33
6.1	General Remarks .....	33
6.2	Test Case Results .....	33
6.2.1	Steady Results .....	33
6.2.2	Unsteady Results .....	35
6.3	Variation Cases .....	44
6.3.1	Results with 110% and 90% Oscillating Frequency .....	44
6.3.2	Results with 110% Pressure Ratio .....	45
7	Conclusion and Future Work .....	47
7.1	Conclusion .....	47
7.2	Future Work .....	48
	Appendix .....	49
A	Additional Graphs .....	49
B	Matlab Codes .....	67
	generalized_force.m (Calculate the generalized force) .....	67
	AR.m (Calculate the element area) .....	74
	References .....	79

## List of Tables

Table 5.1: Flow parameters for STCF4 Case 628, from Witteck et al. (2012).....	30
Table 5.2: Geometric parameters of STCF4 blade slice cascade .....	32

## List of Figures

Figure 1.1: High-bypass turbofan engine of the first generation of wide-body aircraft (Pratt & Whitney PW4000).....	2
Figure 2.1: Campbell Diagram showing different aeroelasticity problems. Shown are force response (FR), flutter, non-synchronous vibration (NSV), and separated flow vibration (SFV), from Bendiksen et al. (2010) .....	4
Figure 3.1: The Collar diagram A: aerodynamic forces; B: buffeting; D: Static divergence; E: elastic forces; F: flutter; G: gust; I: inertia forces; L: loading problems; R: reversal of control; S: stability and control; V: mechanical vibration; Z: impacts, from Collar (1946) .	6
Figure 3.2: Typical section pitching and plunging airfoil .....	7
Figure 3.3: Dimensionless damping $\frac{P_R}{\omega_\alpha}$ , and frequency $\frac{P_I}{\omega_\alpha}$ vs. reduced airspeed $\frac{U}{b\omega_\alpha}$ , from Dowell et al. (2004).....	9
Figure 3.4: Interpretation of the reduced frequency, from Oates (1989).....	11
Figure 3.5: Schematic interpretation of the mass ratio, from Meinzer (2011).....	12
Figure 3.6: Traveling wave pitching mode for a cascade of 12 flat plates, with nodal diameter $n$ and interblade phase angle $\sigma$ , from Meinzer (2011) .....	13
Figure 3.7: Compressor performance map showing flutter boundaries for different types of flutter, from Oates (1989).....	15
Figure 3.8: Differences in flow conditions between stalled flow and choked flow, from Oates (1989).....	16
Figure 3.9: Blade row under supersonic relative flow with propagated Mach wave, from Oates (1989).....	17
Figure 3.10: Schematic representation of a two dimensional typical session cascade with both pitching and bending motions .....	18
Figure 4.1: Computational grid for the STCF4 slice (view 1).....	27

Figure 4.2: Computational grid for the STCF4 slice (view 2).....	28
Figure 5.1: Photo of the STCF4 test cascade rig .....	29
Figure 5.2: Pressure gradient distribution at blade midspan from MUSTANG .....	30
Figure 5.3: Schematic illustration of STCF4 blade cascade .....	31
Figure 6.1: Steady surface pressure coefficient at midspan ( $k=3$ ) vs. $x/c$ from MUSTANG, ANSYS CFX 13.0, and experiment data .....	35
Figure 6.2: 1 <sup>st</sup> harmonic amplitude of the surface unsteady pressure at midspan ( $k=3$ ), $IBPA = 180^\circ$ from MUSTANG, ANSYS CFX 13.0, and experimental data .....	37
Figure 6.3: 1 <sup>st</sup> harmonic phase shift of the surface unsteady pressure at midspan ( $k=3$ ), $IBPA = 180^\circ$ from MUSTANG, ANSYS CFX 13.0, and experimental data .....	38
Figure 6.4: 1 <sup>st</sup> harmonic amplitude of the surface unsteady pressure at midspan ( $k=3$ ), $IBPA = 270^\circ$ from MUSTANG, ANSYS CFX 13.0, and experimental data .....	39
Figure 6.5: 1 <sup>st</sup> harmonic phase shift of the surface unsteady pressure at midspan ( $k=3$ ), $IBPA = 270^\circ$ from MUSTANG, ANSYS CFX 13.0, and experimental data .....	40
Figure 6.6: Real part and Imaginary part of the unsteady generalized force amplitude at different $IBPA$ 's. ....	41
Figure 6.7: Stability curves of MUSTANG results and experimental data .....	42
Figure 6.8: Stability curves of MUSTANG results by using 161 integration points and 11 integration points, compared with experimental results .....	44
Figure 6.9: Stability curve with 100%, 90%, and 110% oscillating frequency .....	45
Figure 6.10: Stability curve with 100% and 110% pressure ratio.....	46
Figure 8.1: Unsteady surface pressure 1 <sup>st</sup> harmonic amplitude at midspan ( $k=3$ ) for $IBPA = 0^\circ$ .....	49
Figure 8.2: Unsteady surface pressure 1 <sup>st</sup> harmonic phase at midspan ( $k=3$ ) for $IBPA = 0^\circ$ .....	49

Figure 8.3: Unsteady surface pressure 1 <sup>st</sup> harmonic amplitude at midspan (k=3) for $IBPA = 18^\circ$ .....	50
Figure 8.4: Unsteady surface pressure 1 <sup>st</sup> harmonic phase at midspan (k=3) for $IBPA = 18^\circ$ .....	50
Figure 8.5: Unsteady surface pressure 1 <sup>st</sup> harmonic amplitude at midspan (k=3) for $IBPA = 36^\circ$ .....	51
Figure 8.6: Unsteady surface pressure 1 <sup>st</sup> harmonic phase at midspan (k=3) for $IBPA = 36^\circ$ .....	51
Figure 8.7: Unsteady surface pressure 1 <sup>st</sup> harmonic amplitude at midspan (k=3) for $IBPA = 54^\circ$ .....	52
Figure 8.8: Unsteady surface pressure 1 <sup>st</sup> harmonic phase at midspan (k=3) for $IBPA = 54^\circ$ .....	52
Figure 8.9: Unsteady surface pressure 1 <sup>st</sup> harmonic amplitude at midspan (k=3) for $IBPA = 72^\circ$ .....	53
Figure 8.10: Unsteady surface pressure 1 <sup>st</sup> harmonic phase at midspan (k=3) for $IBPA = 72^\circ$ .....	53
Figure 8.11: Unsteady surface pressure 1 <sup>st</sup> harmonic amplitude at midspan (k=3) for $IBPA = 90^\circ$ .....	54
Figure 8.12: Unsteady surface pressure 1 <sup>st</sup> harmonic phase at midspan (k=3) for $IBPA = 90^\circ$ .....	54
Figure 8.13: Unsteady surface pressure 1 <sup>st</sup> harmonic amplitude at midspan (k=3) for $IBPA = 108^\circ$ .....	55
Figure 8.14: Unsteady surface pressure 1 <sup>st</sup> harmonic phase at midspan (k=3) for $IBPA = 108^\circ$ .....	55
Figure 8.15: Unsteady surface pressure 1 <sup>st</sup> harmonic amplitude at midspan (k=3) for $IBPA = 126^\circ$ .....	56

Figure 8.16: Unsteady surface pressure 1 <sup>st</sup> harmonic phase at midspan (k=3) for $IBPA = 126^\circ$ .....	56
Figure 8.17: Unsteady surface pressure 1 <sup>st</sup> harmonic amplitude at midspan (k=3) for $IBPA = 144^\circ$ .....	57
Figure 8.18: Unsteady surface pressure 1 <sup>st</sup> harmonic phase at midspan (k=3) for $IBPA = 144^\circ$ .....	57
Figure 8.19: Unsteady surface pressure 1 <sup>st</sup> harmonic amplitude at midspan (k=3) for $IBPA = 162^\circ$ .....	58
Figure 8.20: Unsteady surface pressure 1 <sup>st</sup> harmonic phase at midspan (k=3) for $IBPA = 162^\circ$ .....	58
Figure 8.21: Unsteady surface pressure 1 <sup>st</sup> harmonic amplitude at midspan (k=3) for $IBPA = 198^\circ$ .....	59
Figure 8.22: Unsteady surface pressure 1 <sup>st</sup> harmonic phase at midspan (k=3) for $IBPA = 198^\circ$ .....	59
Figure 8.23: Unsteady surface pressure 1 <sup>st</sup> harmonic amplitude at midspan (k=3) for $IBPA = 216^\circ$ .....	60
Figure 8.24: Unsteady surface pressure 1 <sup>st</sup> harmonic phase at midspan (k=3) for $IBPA = 216^\circ$ .....	60
Figure 8.25: Unsteady surface pressure 1 <sup>st</sup> harmonic amplitude at midspan (k=3) for $IBPA = 234^\circ$ .....	61
Figure 8.26: Unsteady surface pressure 1 <sup>st</sup> harmonic phase at midspan (k=3) for $IBPA = 234^\circ$ .....	61
Figure 8.27: Unsteady surface pressure 1 <sup>st</sup> harmonic amplitude at midspan (k=3) for $IBPA = 252^\circ$ .....	62
Figure 8.28: Unsteady surface pressure 1 <sup>st</sup> harmonic phase at midspan (k=3) for $IBPA = 252^\circ$ .....	62

Figure 8.29: Unsteady surface pressure 1 <sup>st</sup> harmonic amplitude at midspan (k=3) for $IBPA = 288^\circ$ .....	63
Figure 8.30: Unsteady surface pressure 1 <sup>st</sup> harmonic phase at midspan (k=3) for $IBPA = 288^\circ$ .....	63
Figure 8.31: Unsteady surface pressure 1 <sup>st</sup> harmonic amplitude at midspan (k=3) for $IBPA = 306^\circ$ .....	64
Figure 8.32: Unsteady surface pressure 1 <sup>st</sup> harmonic phase at midspan (k=3) for $IBPA = 306^\circ$ .....	64
Figure 8.33: Unsteady surface pressure 1 <sup>st</sup> harmonic amplitude at midspan (k=3) for $IBPA = 324^\circ$ .....	65
Figure 8.34: Unsteady surface pressure 1 <sup>st</sup> harmonic phase at midspan (k=3) for $IBPA = 324^\circ$ .....	65
Figure 8.35: Unsteady surface pressure 1 <sup>st</sup> harmonic amplitude at midspan (k=3) for $IBPA = 342^\circ$ .....	66
Figure 8.36: Unsteady surface pressure 1 <sup>st</sup> harmonic phase at midspan (k=3) for $IBPA = 342^\circ$ .....	66

# Nomenclature

## Latin Letters

A	m <sup>2</sup>	Area
$A_i$	-	Fourier coefficient
B	-	Fourier coefficient
b	m	Half chord
c	m	Chord length
$C_L$	-	Lift Coefficient
D	-	Pseudo-spectral operator
E	-	Discrete Fourier transform operator
E	J	Enthalpy
F	-	Flux in x
F	N	Force
f	Hz	Frequency
G	-	Flux in y
H	-	Flux in z
I	Nms <sup>2</sup> /rad	Inertia
I	J	Renthalpy
i	-	Imaginary unit, $i = \sqrt{-1}$
K	Nm/rad	Stiffness
k	kg/s <sup>2</sup>	Stiffness
k	-	Integer
k	-	Nodal diameter/wave number
k	-	Reduced frequency
l	-	Integer
m	-	Integer
m	kg	Mass
Ma	-	Mach number
N	-	Nodal diameter
N	-	Number of blades
n	-	Integer
P	Pa	Pressure
q	Pa	Dynamic pressure

r	m	Radius
S	-	Source term
S	-	Southwell coefficient
s	m	Blade pitch
t	s	Time
U	-	Conservation variable
U	m/s	x-direction freestream velocity
u	m/s	Velocity component x
V	m <sup>3</sup>	Volume
V	m/s	Velocity
v	m/s	Velocity component y
W	Nm	Work
w	m/s	Velocity component z
x	m	x-direction coordinate
y	m	y-direction coordinate
z	m	z-direction coordinate

#### Greek Letters

$\alpha$	deg	Inlet angle
$\kappa$	-	Specific heat ratio
$\mu$	-	Mass ratio
$\Phi$	deg	phase angle
$\pi$	-	Pi constant
$\rho$	kg/m <sup>3</sup>	Density
$\sigma$	deg, rad	Interblade phase angle
$\Theta$	deg, rad	Circumferential coordinate
$\theta$	deg	Stagger angle
$\Xi$	-	Stability parameter/Aerodynamic damping coefficient
$\Omega$	1/min	Rotational speed
$\omega$	rad/s	Angular frequency

## Subscript

0	Initial state, point of reference
EO	Engine order
I	Imaginary
R	Real

## Abbreviations

CFD	Computational Fluid Dynamics
EO	Engine Order
DFT	Discrete Fourier Transformation
FEM	Finite Element Method
FR	Forced Response
HBM	Harmonic Balance Method
HCF	High Cycle Fatigue
IBPA	Interblade Phase Angle
LPC	Low Pressure Compressor
LPT	Low Pressure Turbine
MDOF	Multiple Degree of Freedom
NSV	Non Synchronous Vibration
RANS	Reynolds Averaged Navier Stokes
SDOF	Single Degree of Freedom
SFV	Separated Flow Vibration

## **Acknowledgements**

I would like to express sincere gratitude to my advisor, Dr. Robert Kielb for his guidance, suggestions, and patience. I also would like to thank my final exam committee members, Dr. Earl H. Dowell, Dr. Donald B. Bliss, and Dr. Wilkins Aquino for their valuable comments and suggestions. Finally, I greatly appreciate my family for their understanding and support to my education.

# 1 Introduction and Motivation

As an empirical field of study, aeroelasticity dates back to the flutter occurrence on the early “iron” bridge in England, ca 1818 (Platzer and Carta, 1987). In turbomachinery, aeroelasticity has become a major field of enquiry since 1940’s when gas turbines were firstly applied in aircraft propulsion. Nowadays, due to the strict requirement of performance, efficiency, and environment capability in aircraft industry field, jet-engine companies have made significant endeavor on improving efficiency of the engine.

To meet these requirements, high aspect ratio compressor and turbine blades are widely used, as this blade configuration can achieve high bypass ratio and higher isentropic efficiency. However, this type of blade can experience flutter, a major source to cause high cycle fatigue (HCF).

In general, large high-bypass aircraft engines, see e.g. Figure 1.1, include several stages of compressors and turbines. The engine blades with high aspect ratio in the first stage of the low pressure compressor (LPC) and in the last stage of low pressure turbine (LPT) are more likely subjected to intense vibration due to flutter, an effect that arises from interaction between unsteady flow and oscillating structure.

This thesis focuses on the flutter analysis of a single blade row under supersonic tip Mach number flow, which is the typical condition in power turbines. Due to the lack of data for the flutter analysis in this condition, valid unsteady numerical methods are

strongly required to predict the flutter occurrence. Currently, there are some existing approaches to investigate the flutter under supersonic flow. In this work, an unsteady CFD approach, which is developed by Dr. Hall and his coworkers in Duke University, is applied to compute the aerodynamic damping with different interblade phase angles (IBPA). Then, the calculated results are compared with experimental results and the results from other CFD codes. In addition, different initial conditions or boundary conditions will be applied to investigate the sensitivity of the structure in terms of flutter stability to the variation of the vibration frequency and the pressure ratio.

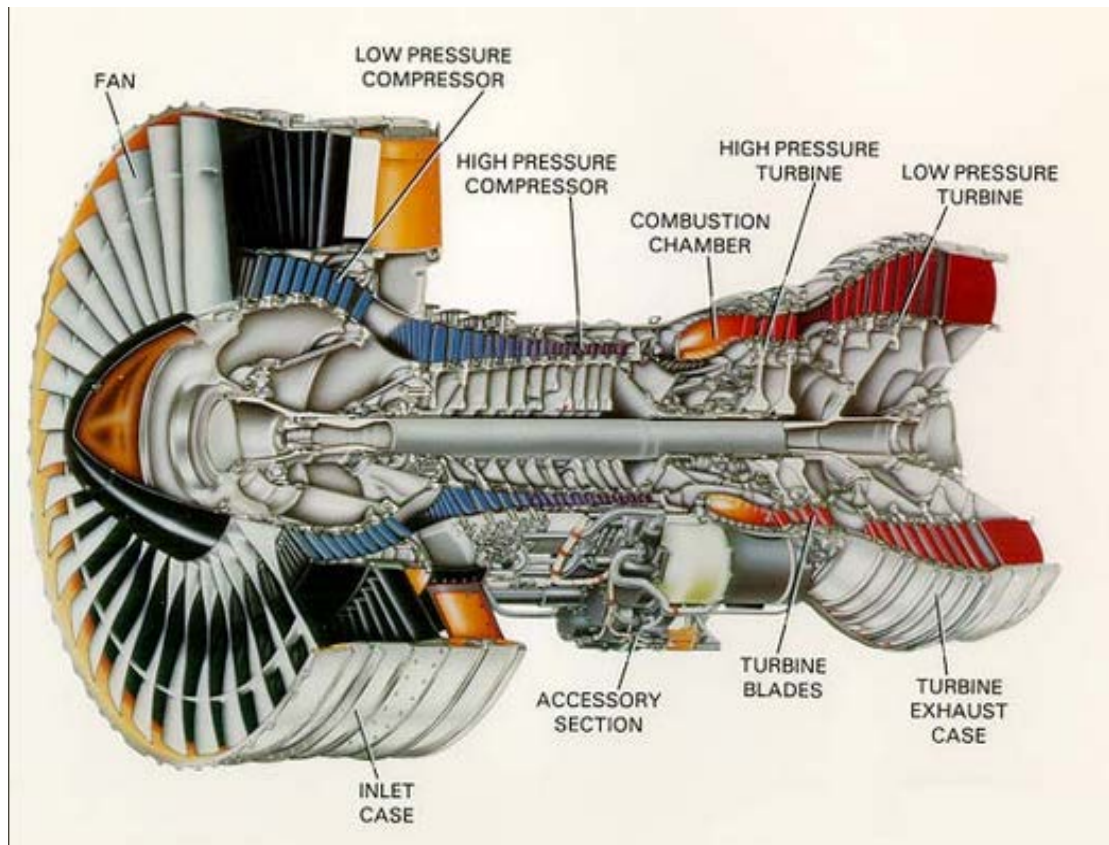


Figure 1.1: High-bypass turbofan engine of the first generation of wide-body aircraft (Pratt & Whitney PW4000)

## 2 Problems Outline

In turbomachinery, there are two major aeroelasticity problems. One is forced response (FR), in which the vibration induced by external forces from adjacent structures or from inlet distortion. This vibration can occur when the excited frequency coincides with the eigenfrequencies of the blade row assembly. The other type of vibration is flutter, a self-excited and self-sustained aeroelastic instability, in which the aerodynamic response of the flow through a blade row due to blade vibration produces negative aerodynamic damping, causing the response to grow exponentially.

In addition to forced response and flutter, non-synchronous vibration (NSV) becomes another typical aeromechanical problem. This type of vibration is caused by flow instabilities, e.g., vortex shedding, flow separation, and unsteady tip clearance flows. These flow instabilities, in certain senses, assemble rotating excitation in a way that they emerge at some distinctive frequency, and rotate at a fixed rotation rate that is not an integer multiple of the rotor frequency (as in forced response) (Bendiksen et al. 2010).

A prevalent tool to show the occurrence of different vibrational circumstances in rotational machinery is the Campbell Diagram, as shown in Figure 2.1. The natural frequencies of the blades (e.g., the first flexure, the first torsion, and the second flexure, etc.) are plotted as a function of rotor speed. Due to centrifugal stiffening, the natural

frequencies increase somewhat as the rotational frequency increases according to

Equation 2.1:

$$\omega = \omega_0 \sqrt{1 + S \Omega^2 / \omega_0^2} \quad (2.1)$$

Above,  $\omega_0$  is the blade frequency without rotation,  $\Omega$  is the rotation rate, S is the Southwell coefficient.

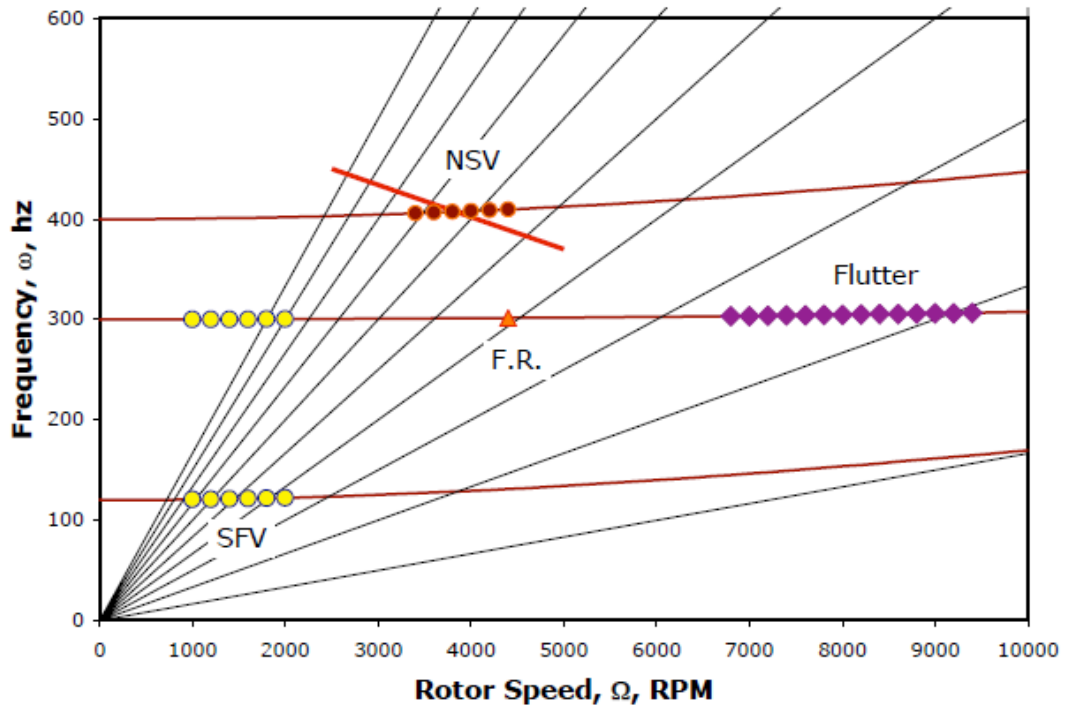


Figure 2.1: Campbell Diagram showing different aeroelasticity problems. Shown are force response (FR), flutter, non-synchronous vibration (NSV), and separated flow vibration (SFV), from Bendiksen et al. (2010)

On the same figure engine order (EO) lines, which show the integer multiples of engine rotation frequency, are plotted as well. Forced response can occur at each intersection point of natural frequency lines and engine order lines.

According to Figure 2.1, flutter occurs at frequencies close to some of the blade natural frequencies. Flutter typically occurs on the 1<sup>st</sup> or 2<sup>nd</sup> mode of the blade structure. Non-synchronous vibration occurs at low-speed off-design conditions, and the frequency is usually locked onto a blade natural frequency.

As flutter is one of the most hazardous phenomena in turbomachinery, the objective of this thesis is to predict the flutter occurrence for a turbo blade cascade with unsteady CFD codes.

### 3 Theoretical Background

#### 3.1 Wing flutter

Aeroelasticity is a discipline which concerns with physical phenomena involving mutual interaction among inertia forces, elastic forces, and aerodynamic forces. A triangle of discipline, the so-called Collar diagram introduced by Collar (1946), can be used to illustrate the scope of aeroelasticity, as is shown in Fig. 3.1. By connecting each two of the three vertices, different subfields of aeroelasticity can be obtained.

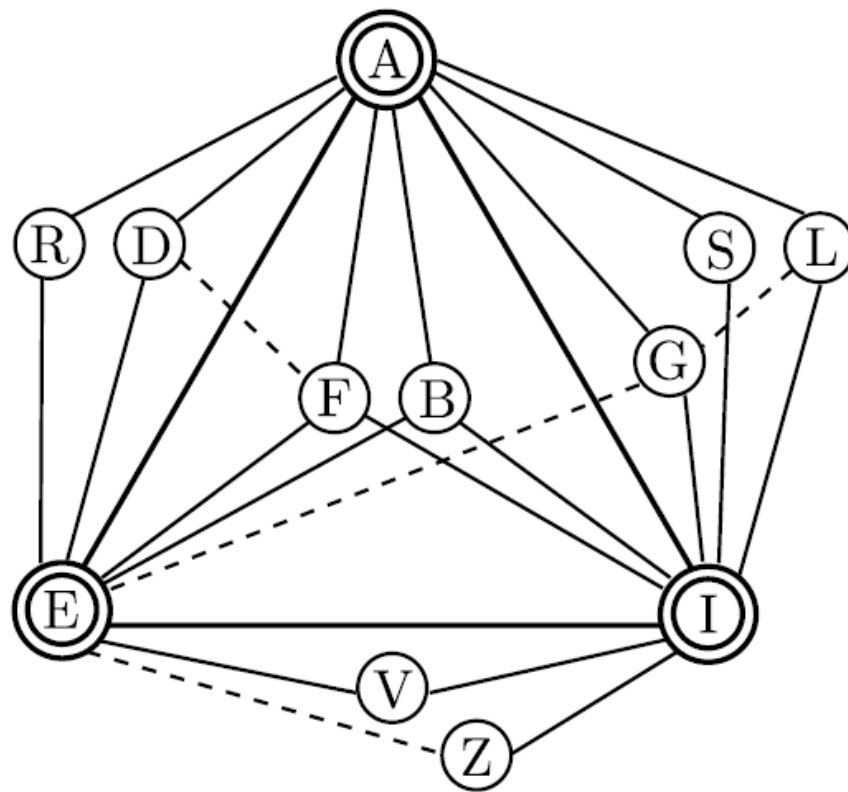


Figure 3.1: The Collar diagram A: aerodynamic forces; B: buffeting; D: Static divergence; E: elastic forces; F: flutter; G: gust; I: inertia forces; L: loading problems; R: reversal of control; S: stability and control; V: mechanical vibration; Z: impacts, from Collar (1946)

Among all the subfields of aeroelasticity, flutter is the most dramatic phenomenon. According to Fig. 3.1, flutter lies in the category of dynamic aeroelasticity which includes all three forces. In aircraft or helicopter structures, coalescence flutter, which occurs when eigenfrequencies of different modes move close together, typically occurs.

Although CFD and FEM are the most common tools to investigate the coalescence flutter in engineering field, a simplified method in the predesign phase is to use a typical section two degree-of-freedom airfoil model, which is shown in Fig. 3.2. This airfoil model allows both pitching and plunging motions.

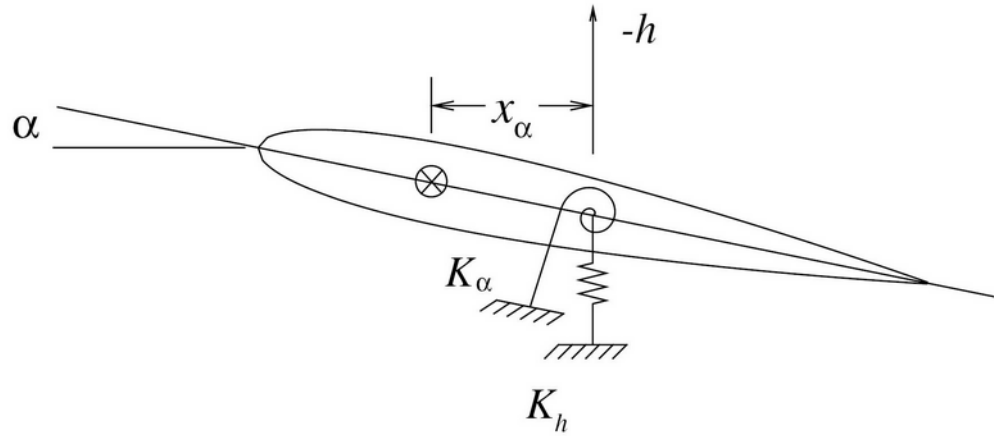


Figure 3.2: Typical section pitching and plunging airfoil

To greatly simplify the problem, a steady flow aerodynamic model is assumed.

Then, derived by Lagrange's equation, the equations of motion for this airfoil model are:

$$m\ddot{h} + S_\alpha \ddot{\alpha} + K_h h = -L = -qc \frac{\partial C_L}{\partial \alpha} \left( \alpha + \frac{\dot{h}}{U} \right) \quad (3.1)$$

$$I_\alpha \ddot{\alpha} + S_\alpha \ddot{h} + K_\alpha \alpha = M_y = Le = qc \frac{\partial C_L}{\partial \alpha} \left( \alpha + \frac{\dot{h}}{U} \right) e \quad (3.2)$$

Assuming the solution has the following form:

$$h = \bar{h}e^{pt} \quad (3.3)$$

$$\alpha = \bar{\alpha}e^{pt} \quad (3.4)$$

Then, substitute Eq. 3.3 and Eq. 3.4 into Eq. 3.1 and Eq. 3.2, there are:

$$\begin{pmatrix} mp^2 + K_h + qc \frac{\partial C_L}{\partial \alpha} \frac{p}{U} & S_\alpha p^2 + qc \frac{\partial C_L}{\partial \alpha} \\ S_\alpha p^2 - qc \frac{\partial C_L}{\partial \alpha} e & I_\alpha p^2 + K_\alpha - qc \frac{\partial C_L}{\partial \alpha} e \end{pmatrix} \begin{Bmatrix} \bar{h} \\ \bar{\alpha} \end{Bmatrix} = \begin{Bmatrix} 0 \\ 0 \end{Bmatrix} \quad (3.5)$$

For nontrivial solutions the determinant of coefficient is set to zero, which determines  $p$  correspondingly. Solve for  $p$  from the algebraic equation:

$$Ap^4 + Bp^3 + Cp^2 + Dp + E = 0 \quad (3.6)$$

The solution can be expressed as:

$$p = p_R + ip_I \quad (3.7)$$

Therefore,

$$\frac{U}{b\omega_\alpha} \quad (3.8)$$

$$\alpha = \bar{\alpha}e^{p_R t} e^{ip_I t} \quad (3.9)$$

When  $p_R$  is positive, the pitching and plunging oscillation amplitude grow exponentially to infinity theoretically. In reality, due to the nonlinear effects the motion amplitude grows to a finite value, which can be sufficiently large to lead to catastrophic structure failure. Hence, the flutter boundary lies in the point where the sign

of  $p_R$  changes from negative to positive. Fig. 3.3 plots dimensionless parameter  $\frac{p_R}{\omega_\alpha}$ ,

$\frac{p_I}{\omega_\alpha}$  vs. reduced airspeed  $\frac{U}{b\omega_\alpha}$ , which clearly shows the flutter boundary.

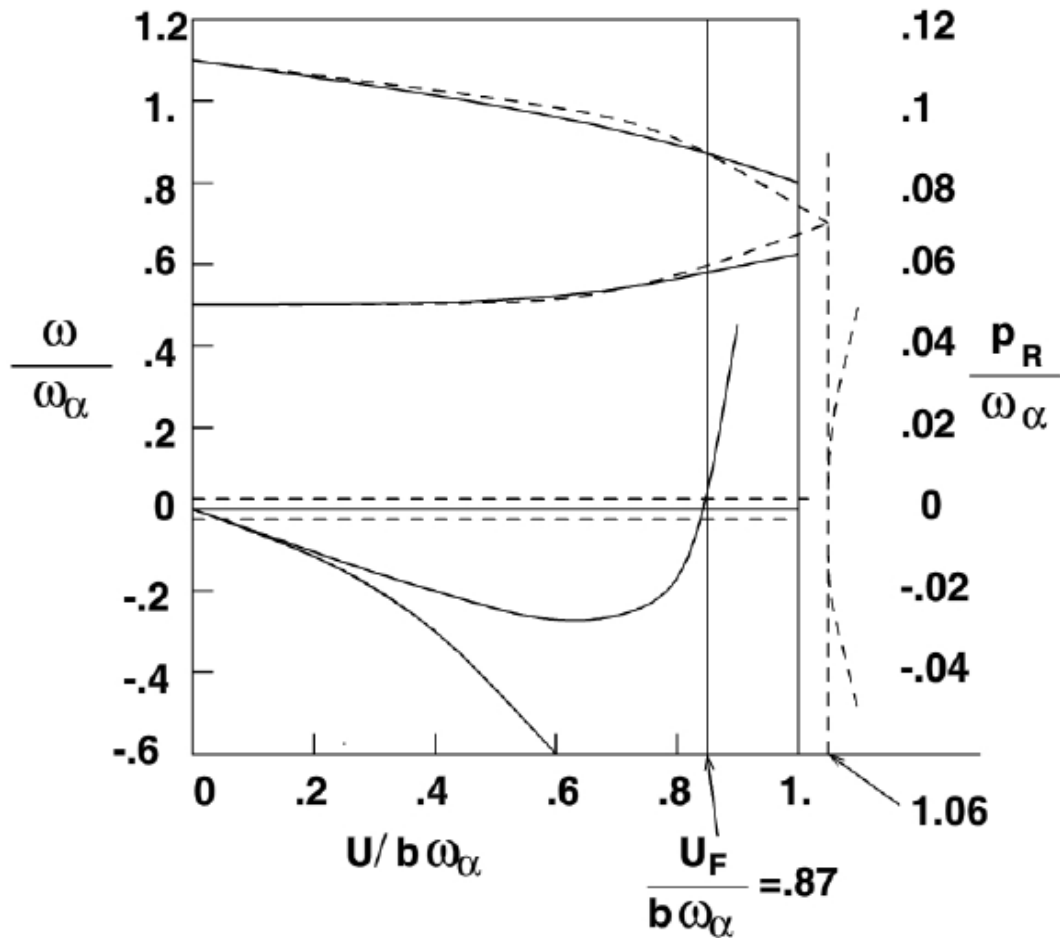


Figure 3.3: Dimensionless damping  $\frac{p_R}{\omega_\alpha}$ , and frequency  $\frac{p_I}{\omega_\alpha}$  vs. reduced airspeed  $\frac{U}{b\omega_\alpha}$ , from Dowell et al. (2004)

## 3.2 Flutter in Turbomachinery

The types of flutter in turbomachinery are fundamentally different from the coalescence wing flutter. The wing flutter involves the coupling of two or more modes of the wing structure, and flutter occurs when the natural frequencies of these modes coalesce. In contrast, flutter in turbomachinery tends to be a single degree-of-freedom phenomenon in which only a single blade vibratory mode and a single interblade phase angle traveling wave (for tuned systems) are considered. The mode shape and frequency of vibration of the blades are nearly unchanged by the unsteady aerodynamic forces acting on the blades. However, the aerodynamic forces arising from the blade vibration provide certain amount of positive or negative damping (Bendiksen et al., 2010). If the aerodynamic damping is negative and greater in magnitude than the combined damping provided by the structural material and the mechanical dampers (viscous and friction damper), then the systems will flutter.

### 3.2.1 Key Parameters affecting Turbomachinery Flutter

Flutter in turbomachinery is closely dependent on several parameters, among which the most important ones are reduced frequency, mass ratio, interblade phase angle, and loading (such as incidence angle).

The reduced frequency ( $k$ ), which is a dimensionless parameter shared by all flutter phenomena, is:

$$k = \frac{\omega b}{V} \quad (3.10)$$

Above,  $\omega$  refers to the frequency of the oscillation,  $b$  the semichord, and  $V$  the freestream velocity. The reduced frequency characterizes the unsteadiness of the airfoil vibration. It can be interpreted as the ratio of the time a particle needs to travel over the distance of the semichord to the oscillation period of the airfoil (Srinivasan, 1997).

Another interpretation of the reduced frequency is the ratio of chord length ( $c$ ) to the wave length ( $\lambda$ ) of the sinusoidal wake formed in the freestream flow field by the vibrating airfoil, as is shown by Oates (1989) in Fig. 3.4. For a low reduced frequency ( $0 \leq k \leq 0.05$ ) the wave length is much larger compared to the chord length and therefore the flow can be assumed as quasi-steady, while for higher reduced frequency ( $k \geq 0.05$ ) the wave length can be the same magnitude of the chord length, which signifies that both steady and unsteady effects need to be taken into account (Srinivasan, 1997).

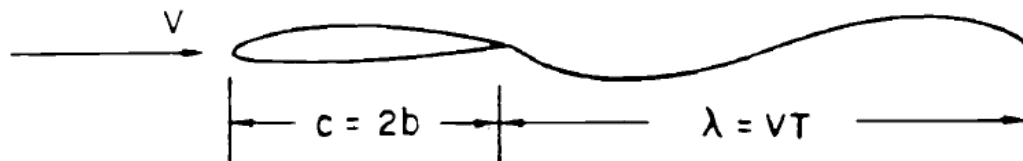


Figure 3.4: Interpretation of the reduced frequency, from Oates (1989)

From Shannon (1945), torsional stall flutter could occur for values of reduced frequency  $k \leq 0.75$ . Hence, the reduced frequency is a crucial parameter which accounts for the occurrence of flutter.

The second dimensionless parameter, one of the major differences between aeroelastic phenomena on airfoil and on a turbomachine blade, is the mass ratio  $\mu$  which refers to the ratio between the mass of the airfoil and the mass of the air  $m$  with density  $\rho$  confined in a circular region with diameter of chord length ( $c$ ) surrounding the airfoil. Eq. 3.11 gives the definition of the mass ratio, which is illustrated in Fig. 3.5:

$$\mu = \frac{4m}{\pi c^2 \rho} \quad (3.11)$$

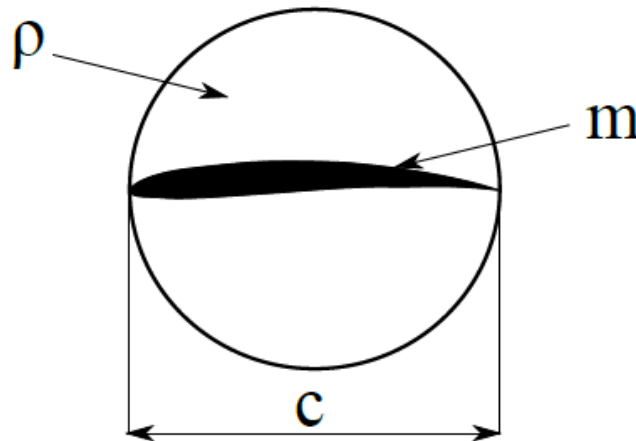


Figure 3.5: Schematic interpretation of the mass ratio, from Meinzer (2011)

The relatively high mass ratio in turbomachinery prevents the coalescence of different modes. This fact explains why mode coupling is not the predominant mechanism of flutter in turbomachinery (Marshall and Imregun, 1996).

In addition to the reduced frequency  $k$  and the mass ratio  $\mu$ , another parameter, the other major difference between wing aeroelasticity and turbomachinery

aeroelasticity, is the interblade phase angle (IBPA)  $\sigma$ . Unlike an aircraft wing, a vibrating blade is surrounded by adjacent blades which influence its vibration by coupling through the fluid and the structure. Therefore, a large number of degrees of freedom are required to analyze the whole structure, which brings about significant difficulties to the analysis. Lane (1956) showed that, assuming that all blades are identical and equally spaced around a rotor, each blade vibrates in the same mode but with a phase shift-known as the interblade phase angle  $\sigma$ . Therefore, it is sufficient to analyze a single blade. Fig. 3.6 shows the motion pattern for a pitching blade cascade.

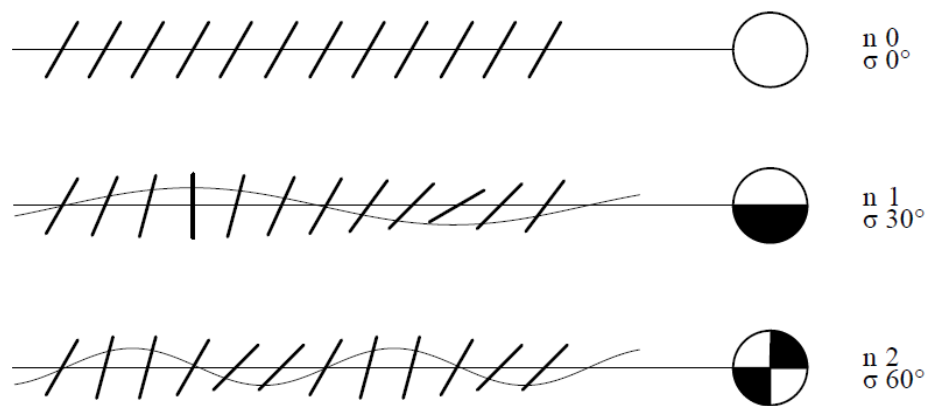


Figure 3.6: Traveling wave pitching mode for a cascade of 12 flat plates, with nodal diameter  $n$  and interblade phase angle  $\sigma$ , from Meinzer (2011)

To calculate the interblade phase angle, Eq. 3.12 is applied:

$$\sigma = \frac{2\pi \cdot N}{N_{bl}} \quad (3.12)$$

Here,  $N$  is the nodal diameter (wave number),  $N_{bl}$  is the number of blade in the cascade. The interblade phase angle has a large influence on the coupling of adjacent blades motions, and therefore significantly affects the stability of the blade.

Additionally, loading is another parameter which significantly influences the flutter occurrence. Even small variations in the loading condition, such as incidence angle and pressure ratio, can lead to considerable changes in term of the flutter stability of the structure.

### **3.2.2 Types of Flutter in Turbomachinery**

In turbomachinery, flutter is a phenomenon which can occur under different operation conditions. Fig. 3.7 shows the flutter boundaries for different types of flutter in the compressor performance map.

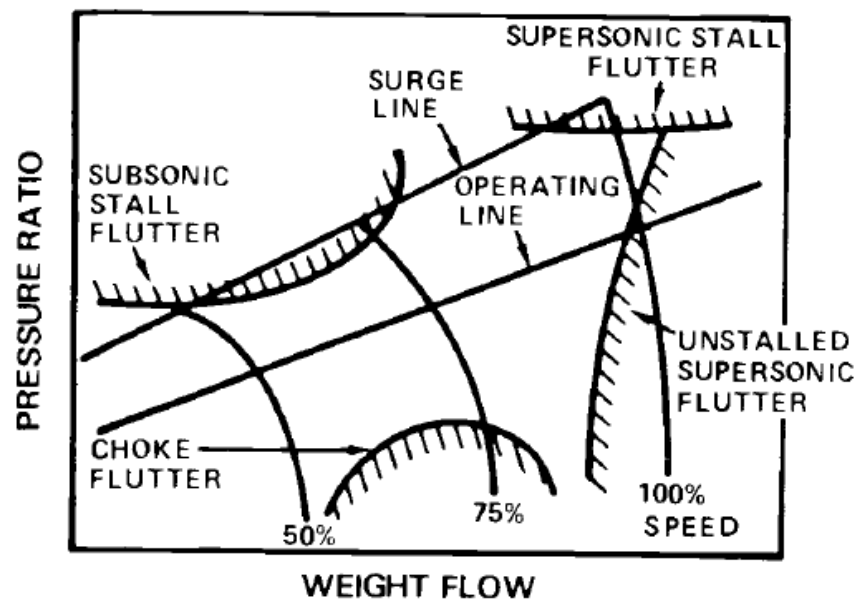


Figure 3.7: Compressor performance map showing flutter boundaries for different types of flutter, from Oates (1989)

The first type of flutter is stall flutter, which occurs near the stall or surge line.

Typically, stall flutter occurs at partial-speed operation with higher than average incidence, causing flow separation. This flow separation further reduces the axial flow velocity, resulting in a temporary reversed flow until stabilized again (Dowell et al., 2004). According to the freestream flow speed region in the compressor performance map, stall flutter can be divided into subsonic stall flutter and supersonic stall flutter.

The second type of flutter is choke flutter, which occurs near the choke line as shown in Fig. 3.6. Choke flutter occurs at partial-speed operation at low-sometimes even negative-incidence. The differences in the flow conditions for stall flutter and chock flutter are shown in Fig. 3.8. When choke occurs, the inlet flow is constrained to pass

through a smaller in-passage stream area, producing higher in-passage Mach number. If the in-passage Mach number exceeds the local critical values, in-passage shock can form, causing flow separation, or couple the adjacent blades directly. In either case, severe vibration can occur, triggering flutter (Oates, 1989).

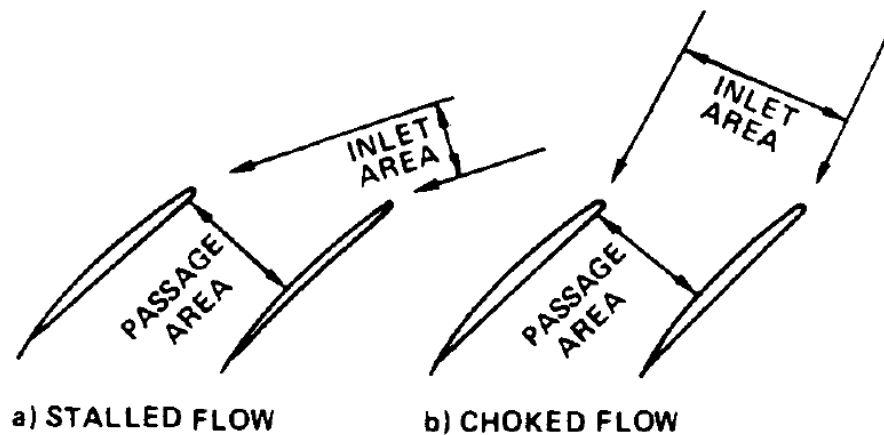


Figure 3.8: Differences in flow conditions between stalled flow and choked flow, from Oates (1989)

Another type of flutter, which is discussed and analyzed in this thesis, is the unstalled supersonic flutter. The unstalled supersonic flutter normally occurs at full speed with supersonic relative flow velocity but subsonic axial flow velocity. Because the axial flow is subsonic, Mach waves can propagate forward of the plane of rotation. When flutter occurs, the Mach waves will propagate with varied amplitude and phase, and therefore exerting unsteady influence ahead of the adjacent blades. Fig. 3.9 shows a portion of a blade row under supersonic relative flow with propagated Mach wave.

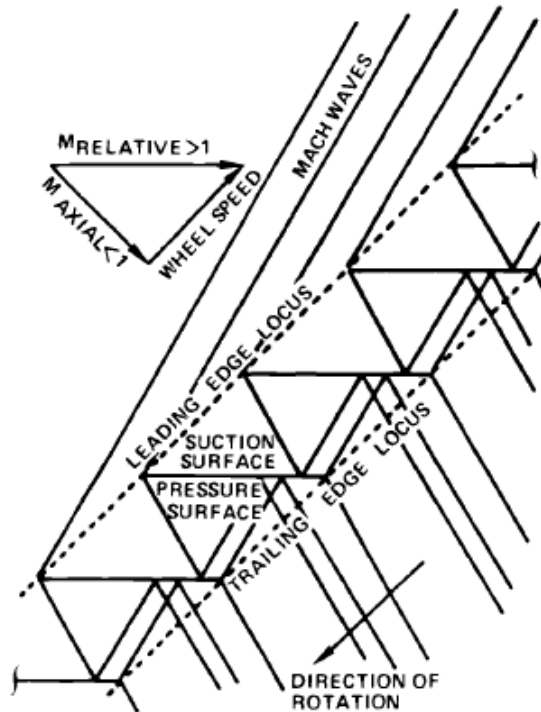


Figure 3.9: Blade row under supersonic relative flow with propagated Mach wave, from Oates (1989)

### 3.2.3 Flutter Stability

The onset of flutter is characterized by the point where the oscillating structure extracts energy from the flow, which represents that the aerodynamic work done by the fluid is positive. Hence, a criterion to judge whether the vibrating structure will flutter is to evaluate the sign of the aerodynamic work.

Fig. 3.10 shows a two dimensional typical section blade cascade with both pitching and bending motions. For simplicity, here each blade is considered to have only one degree of freedom, which is the bending motion. To further simplify the problem, the bending motion are assumed to be harmonic in time domain.

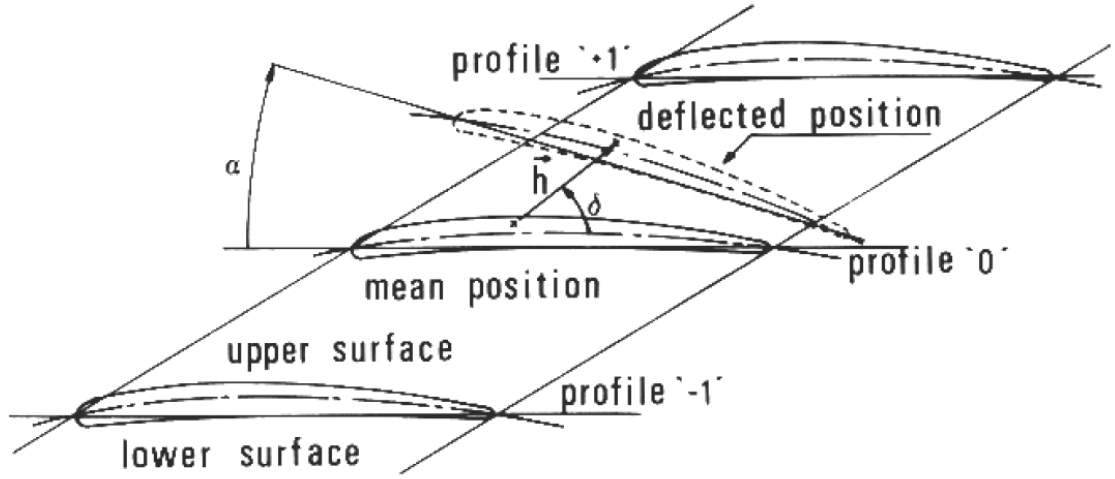


Figure 3.10: Schematic representation of a two dimensional typical session cascade with both pitching and bending motions

Therefore, the bending oscillation for blade  $s$  can be expressed by Eq. 3.13:

$$\vec{h}_s(t) = h_s \cdot e^{i\omega_s t} \cdot \vec{e}_{h,s} \quad (3.13)$$

Above,  $h_s$  is the bending amplitude of the vibrating blade  $s$ , and  $\omega_s$  is the oscillating frequency of the vibrating blade  $s$ .

Hence, the generalized force induced by the blade vibration also can be considered as harmonic in time domain expressed in Eq. 3.14:

$$\vec{F}_s(t) = (\bar{F}_s + F_s \cdot e^{i\omega_s t}) \cdot \vec{e}_{h,s} \quad (3.14)$$

Here,  $\bar{F}_s$  is the steady generalized force, and  $F_s$  is the amplitude of the unsteady generalized force. As the generalized force is caused by the blade vibration, it can have a

phase shift away from the bending vibration. Therefore,  $F_s$  in general is a complex number expressed as Eq. 3.15:

$$F_s = F_{R,s} + iF_{I,s} \quad (3.15)$$

Then, it is not difficult to show that Eq. 3.16 is true:

$$\vec{F}_s(t) = (\bar{F}_s + \frac{1}{2}(F_s \cdot e^{i\omega_s t} + F_s^* \cdot e^{-i\omega_s t})) \cdot \vec{e}_{h,s} \quad (3.16)$$

Above,  $F_s^*$  is the complex conjugate of  $F_s$ . The aerodynamic work per cycle then can be calculated from Eq. 3.17:

$$W_{cyc,s} = \int_0^{\frac{2\pi}{\omega}} \vec{F}_s(t) \cdot d\vec{h}_s(t) \quad (3.17)$$

Substituting Eq. 3.15, Eq. 3.16 and Eq. 3.13 into Eq. 3.17, the following Eq. 3.18 can be obtained after some manipulation:

$$W_{cyc,s} = \pi \cdot h_s \cdot F_{I,s} \quad (3.18)$$

As  $h_s$  is always positive, the sign of the aerodynamic work is the same as the sign for the imaginary part of the amplitude of the unsteady generalized force. Therefore, flutter occurs when  $F_{I,s}$  is positive, meaning that the fluid exerts positive aerodynamic work onto the vibrating blade structure.

Another parameter to evaluate the flutter stability is the aerodynamic damping coefficient, sometimes called the stability parameter  $\Xi$ , which is defined from Eq. 3.19.

$$\Xi = -\frac{1}{(p_{t,1} - p_1)c^3} \frac{W_{cyc,s}}{\pi h_s^2} = -\frac{C_{W_{cyc,s}}}{\pi h_s^2} \quad (3.19)$$

Here,  $V$  is the freestream velocity,  $c$  is the chord length,  $C_{W_{exc.s}}$  is the work coefficient. As is shown in Eq. 3.19, the sign of the stability parameter  $\Xi$  is opposite to the sign of the aerodynamic work. Therefore, flutter occurs when the stability parameter  $\Xi$  is negative.

## 4 Numerical Approach in turbomachinery research

In this Chapter, the computational method to simulate the unsteady flow phenomenon in this research is briefly discussed. To solve the Navier-Stokes equation or inviscid Euler equation, a novel “Harmonic Balance “ method has been developed by Hall et al. (2002). Most content of this chapter is based on the work from Ekici et al. (2007).

### 4.1 Governing Equation

The Navier-Stokes equation and the Reynold Average Navier-Stokes (RANS) equation, which govern the flow phenomena in turbomachinery, are derived by applying laws of mass conservation, momentum conservation, and energy conservation to a control volume. The derivation of the Navier-Stokes equation can be found in Anderson et al. (1984).

Prandtl shows that the viscous effect is constrained in a thin boundary layer. Therefore, the inviscid case is assumed here to explain the theory in a simple manner. In the numerical calculation, viscosity is actually taken into consideration. This inviscid Navier-Stokes equation is the so-called Euler equation. The Euler equation in turbomachinery is given by Ekici et al. (2007) as:

$$\frac{d}{dt} \iiint_V U dV + \iint_A [F - U\dot{f}, G - U\dot{g}, H - U\dot{h}] \cdot \vec{n} dA = \iiint_V S dV \quad (4.1)$$

Here,  $\dot{f}, \dot{g}, \dot{h}$  are the  $x, y, z$  velocity components of the control surface. The conservative variable vector  $U$ , the flux vector in respective direction  $F, G, H$  and the source vector  $S$  are given by Eq. 4.2:

$$U = \begin{bmatrix} \rho \\ \rho u \\ \rho v \\ \rho w \\ \rho E \end{bmatrix} \quad F = \begin{bmatrix} \rho u \\ \rho u^2 + p \\ \rho uv \\ \rho uw \\ \rho uI \end{bmatrix} \quad G = \begin{bmatrix} \rho v \\ \rho vu \\ \rho v^2 + p \\ \rho vw \\ \rho vI \end{bmatrix} \quad H = \begin{bmatrix} \rho w \\ \rho wu \\ \rho wv \\ \rho w^2 + p \\ \rho wI \end{bmatrix} \quad S = \begin{bmatrix} 0 \\ 0 \\ \rho(\Omega^2 y + 2\Omega w) \\ \rho(\Omega^2 z - 2\Omega v) \\ 0 \end{bmatrix} \quad (4.2)$$

Now consider an ideal gas with constant specific heat ratio  $\gamma$ , the pressure  $p$  can be calculated as:

$$p = (\gamma - 1)\rho \left[ E - \frac{1}{2}(u^2 + v^2 + w^2) + \frac{1}{2}(\Omega r)^2 \right] \quad (4.3)$$

Here,  $r$  is the distance from the  $x$  axis ( $r = \sqrt{y^2 + z^2}$ ). In Eq. 4.2, the rothalpy  $I$  is defined as:

$$I = \frac{\rho E + p}{\rho} = \frac{\gamma}{\gamma - 1} \frac{p}{\rho} + \frac{1}{2}(u^2 + v^2 + w^2) - \frac{1}{2}(\Omega r)^2 \quad (4.4)$$

As can be seen, both the Navier-Stokes equation and the Euler equation are nonlinear and hence admit nonlinear solutions.

Then, from the calculated pressure, the generalized force can be obtained by:

$$\vec{F}_s(t) = \int_A p(x, y, z) \cdot dA \cdot \langle \vec{e}_n, \vec{e}_h \rangle \vec{e}_h \quad (4.5)$$

## 4.2 Flow Field Kinematics in Frequency Domain

Most content of this section is based on the work from Ekici et al. (2007).

If the non-rotational blades vibrate with frequency  $\omega_0$  and nodal diameter  $k_0$ , then the flow will have  $N$  nodal diameter:

$$N = nk_0 \quad (4.6)$$

Here,  $n$  can take on all integer values. Accordingly, the frequency of the unsteady flow of a specific nodal diameter will be:

$$\omega = n\omega_0 \quad (4.7)$$

Then, the flow can be represented by the time series:

$$U(x, r, \theta, t) = \sum_{k=1}^K [\hat{A}_k(x, r) \cos(\omega_k t + N_k \theta) + \hat{B}_k(x, r) \sin(\omega_k t + N_k \theta)] \quad (4.8)$$

or more generally,

$$U(x, r, \theta, t) = A_0(x, r, \theta) + \sum_{k=1}^K [A_k(x, r, \theta) \cos(\omega_k t) + B_k(x, r, \theta) \sin(\omega_k t)] \quad (4.9)$$

Above,  $\omega_k$  is the  $k$  th non-repeat non-zero absolute frequency.  $N_k$  is the nodal diameter of mode  $k$ .  $\hat{A}_k$  and  $\hat{B}_k$  are the spatial Fourier coefficients of mode  $k$ .  $A_k$  and  $B_k$  are the temporal Fourier coefficients of mode  $k$ .  $\theta$  is the circumferential coordinate. The vector  $U^*$  is constructed by assembling the conservative variables in each blade at a number of sub-time levels. The vector  $\tilde{U}$  is constructed by assembling the Fourier coefficients:

$$U^* = \begin{Bmatrix} U_1 \\ U_2 \\ U_3 \\ U_4 \\ \vdots \end{Bmatrix} \quad \tilde{U} = \begin{Bmatrix} A_0 \\ A_1 \\ A_2 \\ \vdots \\ B_1 \\ B_2 \\ \vdots \end{Bmatrix} \quad (4.10)$$

From Eq. 4.10, if  $K$  harmonics are kept in the Fourier series, then  $\tilde{U}$  has  $2K + 1$  entries. For temporary periodic flow, the Fourier coefficients can be determined from the conservative variables at sub-time levels by left-multiplying a discrete Fourier transform matrix. Conversely, the conservative variables at sub-time levels can be obtained from the Fourier coefficient by left-multiply an inverse discrete Fourier transform matrix.

$$\tilde{U} = EU^* \quad (4.11)$$

$$U^* = E^{-1}\tilde{U} \quad (4.12)$$

Here,  $E$  is the discrete Fourier transform matrix.  $E^{-1}$  is the inverse discrete Fourier transform matrix.

For aperiodic flow normally 50 percent more sub-time levels, that is  $3K + 1$ , are kept. In this circumstance, Eq. 4.12 needs to be modified to:

$$U^* = E^+\tilde{U} \quad (4.13)$$

Above,  $E^+$  is the pseudo inverse of the discrete Fourier transform matrix. An example for an aperiodic flow with 8 harmonics ( $K = 8$ ) is shown in Eq. 4.14.

$$\begin{Bmatrix} U_1 \\ U_2 \\ U_3 \\ \vdots \\ U_{25} \end{Bmatrix} = \begin{bmatrix} 1 & \cos(\omega_1 t_1) & \cdots & \cos(\omega_8 t_1) & \sin(\omega_1 t_1) & \cdots & \cos(\omega_8 t_1) \\ 1 & \cos(\omega_1 t_2) & \cdots & \cos(\omega_8 t_2) & \sin(\omega_1 t_2) & \cdots & \cos(\omega_8 t_2) \\ 1 & \cos(\omega_1 t_3) & \cdots & \cos(\omega_8 t_3) & \sin(\omega_1 t_3) & \cdots & \cos(\omega_8 t_3) \\ \vdots & \vdots & \vdots & \vdots & \vdots & \vdots & \vdots \\ 1 & \cos(\omega_1 t_{25}) & \cdots & \cos(\omega_8 t_{25}) & \sin(\omega_1 t_{25}) & \cdots & \cos(\omega_8 t_{25}) \end{bmatrix} \begin{Bmatrix} A_0 \\ A_1 \\ \vdots \\ A_8 \\ B_1 \\ \vdots \\ B_8 \end{Bmatrix} \quad (4.14)$$

### 4.3 The Harmonic Balance Equations

Most content of this section is based on the work from Ekici et al. (2007).

Ignoring for the moment deformation, Eq. 4.1, in conservative form, can be expressed in differential equations as:

$$\frac{\partial U}{\partial t} + \frac{\partial F}{\partial x} + \frac{\partial G}{\partial y} + \frac{\partial H}{\partial z} = S \quad (4.15)$$

Substituted with conservative variables at all sub-time levels, Eq. 4.15 turns into:

$$\frac{\partial U^*}{\partial t} + \frac{\partial F^*}{\partial x} + \frac{\partial G^*}{\partial y} + \frac{\partial H^*}{\partial z} = S^* \quad (4.16)$$

Based on Eq. 4.9, the time derivative of  $U$  is:

$$\frac{\partial}{\partial t} U = \sum_{k=1}^K [-\omega_k \cdot A_k \sin(\omega_k t) + \omega_k \cdot B_k \cos(\omega_k t)] \quad (4.17)$$

or in matrix form

$$\frac{\partial U^*}{\partial t} = \frac{\partial E^+}{\partial t} \tilde{U} \quad (4.18)$$

Substituted with Eq. 4.13,

$$\frac{\partial U^*}{\partial t} = \frac{\partial E^+}{\partial t} E U^* = D U^* \quad (4.19)$$

Finally, substituting Eq. 4.19 into Eq. 4.16, the harmonic balance equations Eq. 4.20 can be obtained:

$$D U^* + \frac{\partial F^*}{\partial x} + \frac{\partial G^*}{\partial y} + \frac{\partial H^*}{\partial z} = S^* \quad (4.20)$$

As can be seen, Eq. 4.20 is time independent, therefore a steady equation mathematically. To solve this equation, conventional time-marching techniques commonly applied in CFD, are used. A pseudo-time term is introduced, which will eventually vanish when convergence is reached, leaving the steady part of Eq. 4.21. Then, Eq. 4.20 is recovered.

$$\frac{\partial U^*}{\partial \tau} + D U^* + \frac{\partial F^*}{\partial x} + \frac{\partial G^*}{\partial y} + \frac{\partial H^*}{\partial z} = S^* \quad (4.21)$$

#### 4.4 The Unsteady Turbomachinery Code MUSTANG\_HB

In this research, the unsteady multistage turbomachinery code MUSTANG\_HB is used. Based on Fortran 90, MUSTANG\_HB, which was developed at Duke University by Hall and his coworkers, implements the harmonic balance method introduced by Hall et al. (2002). This solver is used to compute steady and unsteady turbomachinery flow in 2D and 3D under both viscous and inviscid case by using the Navier-Stokes equation or the Euler equation.

To solve Eq. 4.21, Lax-Wendroff scheme, a finite volume approach, is applied to discretize the harmonic balance equations into series of algebraic equations. Techniques like local time stepping and multi-grid acceleration are used to reach high convergence speed.

Typically, the computational grid used in MUSTANG\_HB is three block H-O-H style meshes. The O-type grid is used around the blade, and H-type grids are used at the inlet and exit boundaries. If tip clearance gap is considered, an additional H-block is needed to discretize the tip gap region. Fig. 4.1 and Fig. 4.2 show the H-O-H computational grid without tip clearance which is used in this work.

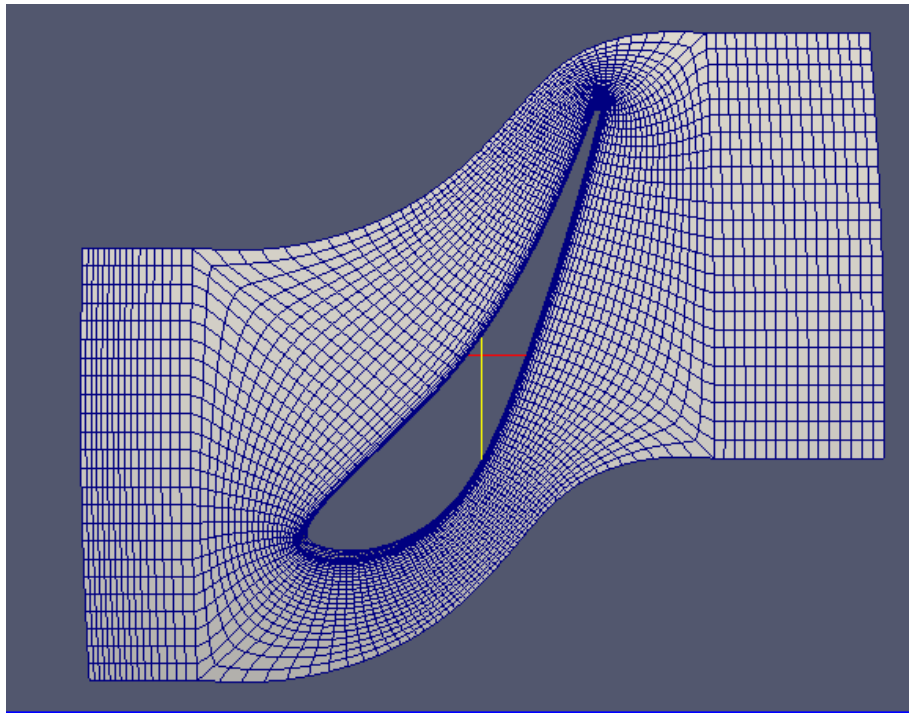


Figure 4.1: Computational grid for the STCF4 slice (view 1)

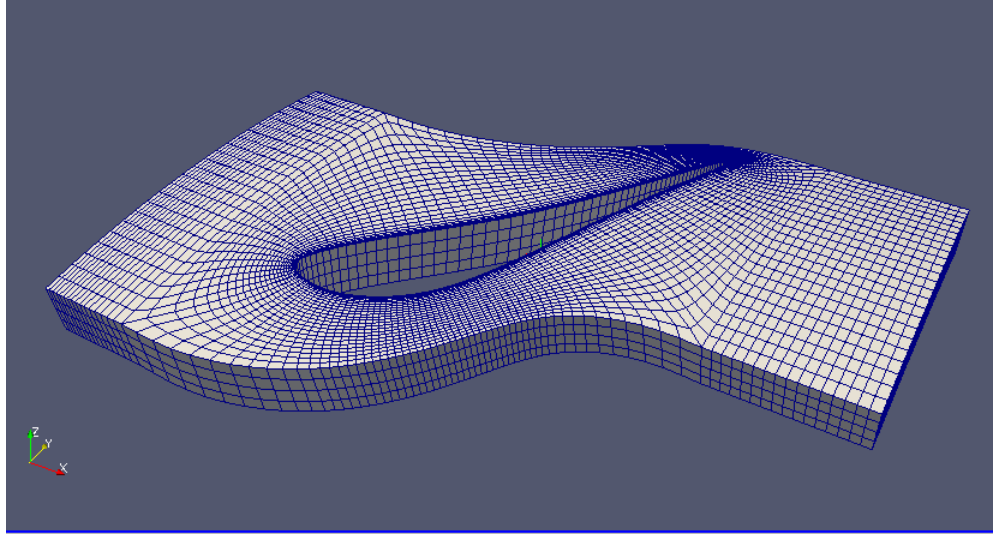


Figure 4.2: Computational grid for the STCF4 slice (view 2)

#### 4.4.1 Periodic Boundary Conditions

Most content of this section is based on the work from Ekici et al. (2007).

By using the complex periodicity conditions along the periodic boundaries, the computational domain can be reduced to a single blade passage. By applying Fourier transform to the solution vector  $U^*$ , the vector of Fourier coefficient  $\tilde{U}$  is obtained. Then, according to Eq. 4.9 and Eq. 4.10, the periodicity boundary conditions, which are applied at every iteration of the Lax-Wendroff solver, are given by:

$$A_k(x, r, \theta + \theta_G) = A_k(x, r, \theta) \cdot \cos(N_k \theta_G) - B_k(x, r, \theta) \cdot \sin(N_k \theta_G) \quad (4.24)$$

$$B_k(x, r, \theta + \theta_G) = A_k(x, r, \theta) \cdot \sin(N_k \theta_G) + B_k(x, r, \theta) \cdot \cos(N_k \theta_G) \quad (4.25)$$

Here,  $\theta_G$  is the circumferential gap between two blades.

## 5 Test Case & Blade Cascade Setting

The blade row considered in this study is the 4<sup>th</sup> Standard Configuration (STCF4), which is an annular turbine cascade containing 20 blades which oscillate sinusoidally as rigid bodies in traveling wave mode, which means that all blades in the cascade vibrate at identical mode shape with a constant interblade phase angle to the adjacent blades (Witteck, 2012). Fig. 5.1 shows a photo of the STCF4 test cascade rig.

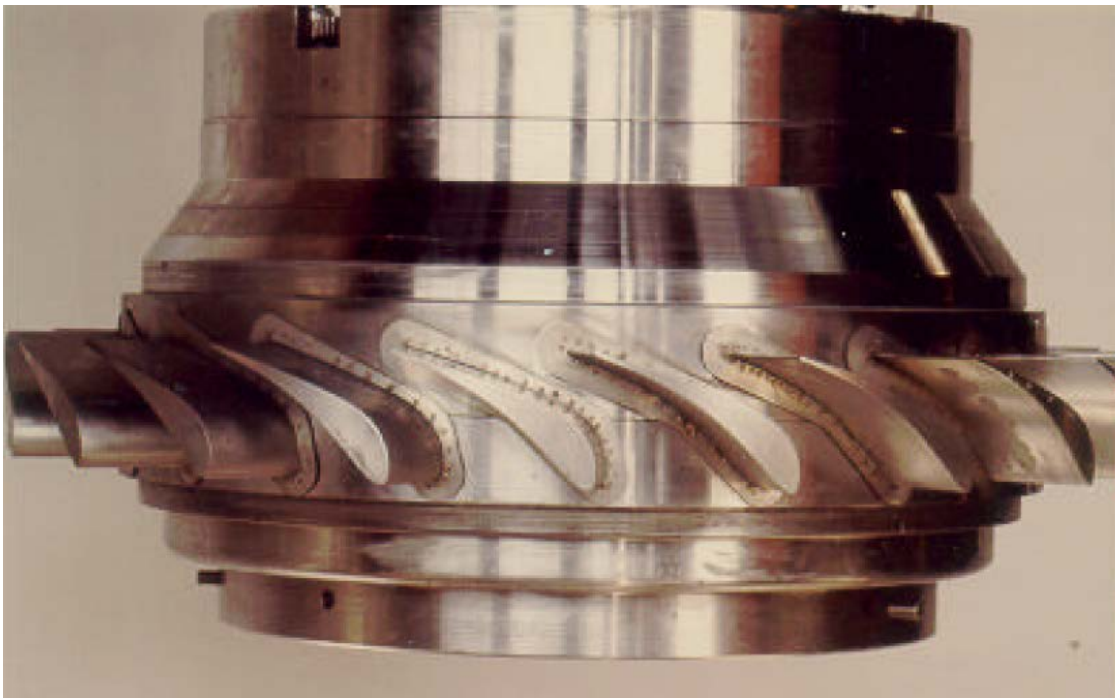


Figure 5.1: Photo of the STCF4 test cascade rig

According to the database from KTH, there are 11 standard configurations with different two-dimensional cascade geometries and flow conditions. The present work deals with STCF4 Case 628, in which the inlet flow is subsonic and the exit flow is supersonic. Case 628 is of great interests as the trailing edge shock on its suction side

propagates downstream from the trailing edge and impinges on the adjacent blade can be easily observed, as is shown in Fig. 5.2. Table 5.1 shows a summary of the main flow conditions in Case 628. This cascade is non-rotational.

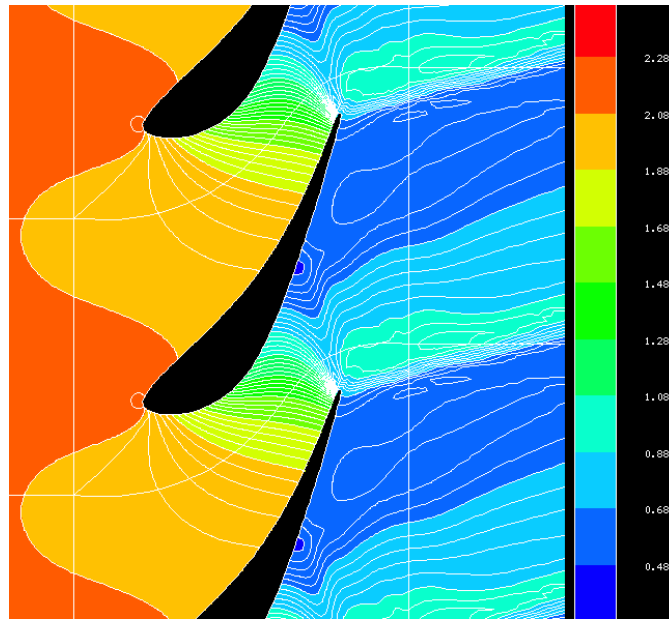


Figure 5.2: Pressure gradient distribution at blade midspan from MUSTANG

Table 5.1: Flow parameters for STCF4 Case 628, from Witteck et al. (2012)

		<b>Case 628 (supersonic)</b>
inlet total pressure	$P_{t,1}$	217,100 Pa
inlet total temperature	$T_{t,1}$	330 K
inlet Mach number	$M_{is,1}$	0.20
outlet Mach number	$M_{is,2}$	1.43
inlet flow angle (vs. axial direction)	$\beta_1$	-28.0 deg
reduced frequency	$k$	0.0779
bending amplitude at hub	$h_h$	0.00315
bending amplitude at midspan	$h_m$	0.00403
bending amplitude at casing	$h_c$	0.00491
bending mode direction	$\delta$	63.0 deg

In Table 5.1, the inlet flow angle  $\beta_1$  applied in the computation is -28 deg, different from the measured angle in the experiment, which is -12 deg. This inconsistency is most likely due to the location of the probe in the experiment. Fig 5.3 shows a schematic illustration of the test blade cascade.

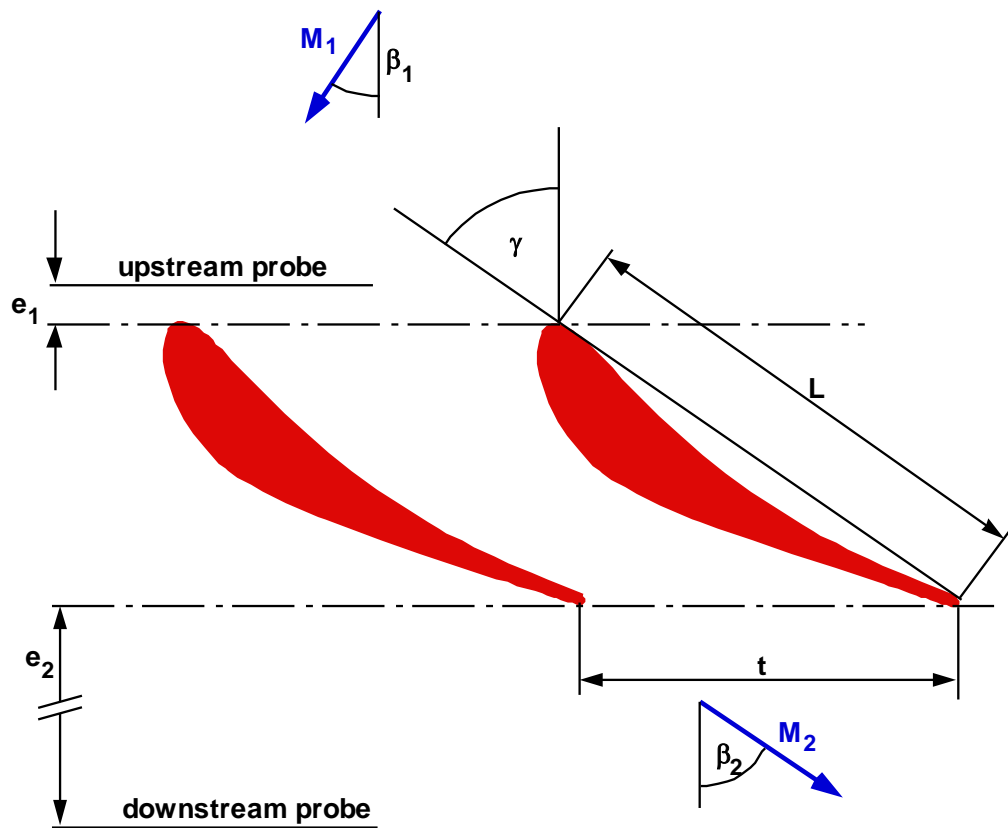


Figure 5.3: Schematic illustration of STCF4 blade cascade

According to Fig 5.3, the probe which measures the inlet flow angle is so close (only 5mm upstream) to the leading edge of the blade that it is significantly affected by the flow. In numerical simulation, the inlet Mach number and the blade loading conditions with inlet flow angle of -28 deg are in a good agreement with those in the

experimental data with  $\beta_1 = -12^\circ$ . According to Witteck et al. (2012) and Mcbean et al. (2005), the inlet flow angle of -28 deg is applied. The geometric parameters of STCF4 in the present work are shown in Table 5.2.

Table 5.2: Geometric parameters of STCF4 blade slice cascade

chord length ( $L$ )	0.0744 m
stagger angle ( $\gamma$ )	$56.6^\circ$
pitch/chord at midspan ( $t/L$ )	0.76
Span (Real/Slice)	0.04 / 0.008 m

## 6 Results and Analysis

In this Chapter, the results of the test case defined in Chapter 5 are presented and discussed. First the test case results are analyzed, in which the steady and unsteady results calculated from the solutions of the MUSTANG\_HB solver are compared with the existing experimental data and the results by a 3D model in ANSYS CFX 13.0 solver from Witteck et al. (2012). Actually, there are still some other results from TBLOCK and Pinelli et al. (2009). However, the reason of picking ANSYS CFX as comparison is that it best matches the experimental data among those CFD solvers shown in Witteck et al. (2012). Then, the results from different initial conditions and boundary conditions are presented to investigate the influence in terms of flutter stability of varying the vibrating frequency and the pressure ratio.

### 6.1 General Remarks

In the present work, a solution is considered converged when the residual reaches the precision class of  $10^{-15}$ , which is close to the machine precision. In addition, nonlinear code is applied to solve the equations.

### 6.2 Test Case Results

#### 6.2.1 Steady Results

The conservative variable solution  $U^*$  can be obtained by solving Eq. 4.21 with Lax-Wendroff algorithm. Then, the pressure  $p$  can be calculated by Eq. 4.3. After

applying the temporal Fourier transform matrix  $E$  to  $p$ , the Fourier coefficient vector  $\hat{p}$  can be calculated. The first entry of  $\hat{p}$  is the steady pressure or mean pressure  $\bar{p}$ . Here, the mean pressure  $\bar{p}$  can be converted into dimensionless steady pressure coefficient  $C_{\bar{p}}$  using Eq. 6.1.

$$C_{\bar{p}} = \frac{\bar{p} - p_1}{p_{t,1} - p_1} \quad (6.1)$$

Above,  $p_1$  is the inlet static pressure.  $p_{t,1}$  is the inlet total pressure. For unsteady pressure, Eq. 6.2 is applied to calculate the unsteady pressure coefficient.

$$C_p = \frac{p}{p_{t,1} - p_1} \cdot \frac{1}{h_s / c} \quad (6.2)$$

Fig. 6.1 shows the steady surface pressure coefficient at midspan calculated from MUSTANG and ANSYS CFX, which are compared with the experimental data in the same plot. According to Fig 6.1, the results from MUSTANG are in a good agreement to the experimental data and the results from CFX at the pressure side. However, in 55%-60% chord region at the suction side, the steady pressure coefficients calculated from MUSTANG show some deviation from the experimental data and CFX, while CFX coincides well with the measured data. This deviation might be due to the simplification by using Quasi 3D grid, in which only a blade slice along the span is extracted. In contrast, the CFX solver uses the full 3D grid, greatly improving the accuracy of the simulation. Therefore, the results from CFX are able to accurately capture the shock behavior at the suction side possibly due to its sophisticated turbulence models.

Additionally, one thing needed to be mention is that the results from other 2D approaches (TBLOCK, Mcbean, and Pinelli) also fail to predict the shock on the suction side.

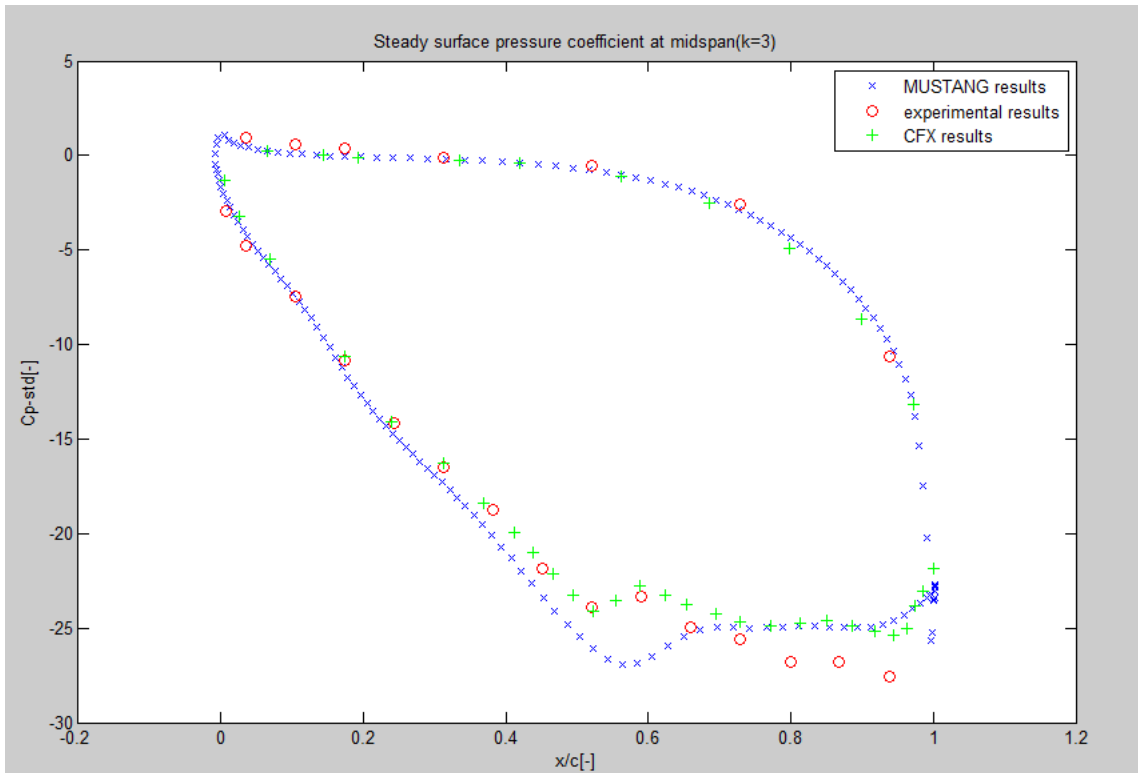


Figure 6.1: Steady surface pressure coefficient at midspan ( $k=3$ ) vs.  $x/c$  from MUSTANG, ANSYS CFX 13.0, and experiment data

## 6.2.2 Unsteady Results

Since the pressure can be decomposed into a series of harmonics, among which the 1<sup>st</sup> harmonic plays a much more important role than other higher frequency harmonics. Therefore, the unsteady pressure can be approximately calculated by including only the 1<sup>st</sup> harmonic. After applying the temporal Fourier transform to get the Fourier coefficient vector  $\hat{p}$ , the coefficients of the real part and the imaginary part of  $\hat{p}$  can be obtained. It

has been shown that the unsteady pressure is dependent on the interblade phase angle (IBPA). The amplitude of the 1<sup>st</sup> harmonic unsteady pressure and phase under different IBPA's are plotted in the Appendix A.

Fig. 6.2 and Fig. 6.3 show the amplitude and the phase shift, respectively, of the 1<sup>st</sup> harmonic of the surface unsteady pressure from MUSTANG, ANSYS CFX, and the experimental data for  $IBPA = 180^\circ$ . According to Fig. 6.2 and Fig. 6.3, the results of 1<sup>st</sup> harmonic amplitude and phase shift from CFX are in a good agreement with the experimental data at the pressure side and to 55% chord on the suction side because downstream of the 55% chord the nonlinear effects like shocks, shock reflections, and the interaction between shocks and the boundary layers add much complexity to the simulation. In contrast, the results of the amplitude and phase shift from MUSTANG are in general close to the results from CFX and the experimental data but with some deviations, which might be partly cause by the 3D finer mesh in CFX instead of quasi 3D coarse mesh in MUSTANG. In addition, there also will be some deviation due to the neglect of the tip clearance in the present work. As is shown in Fig. 6.2 and Fig 6.3, the results from MUSTANG predict the shock occurrence at 50% chord of the suction side. Furthermore, as with the CFX results, the pressure and phase downstream of the shock point calculated from MUSTANG are difficult to evaluate because of the sparseness of the experimental data.

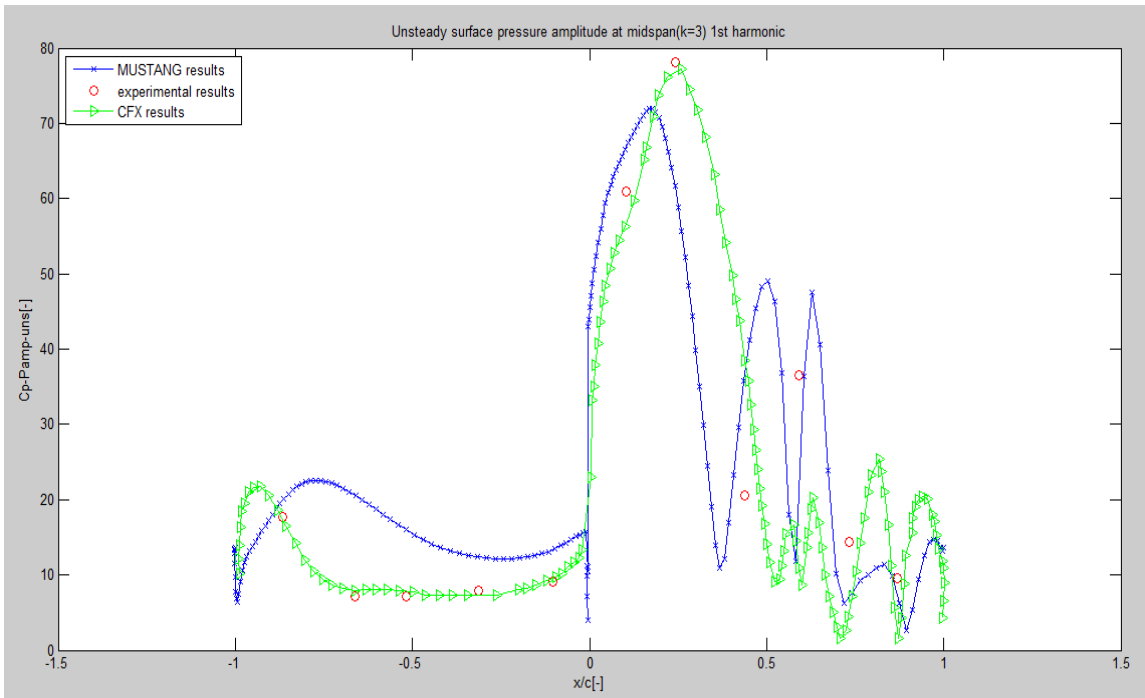


Figure 6.2: 1<sup>st</sup> harmonic amplitude of the surface unsteady pressure at midspan (k=3),  $IBPA = 180^\circ$  from MUSTANG, ANSYS CFX 13.0, and experimental data

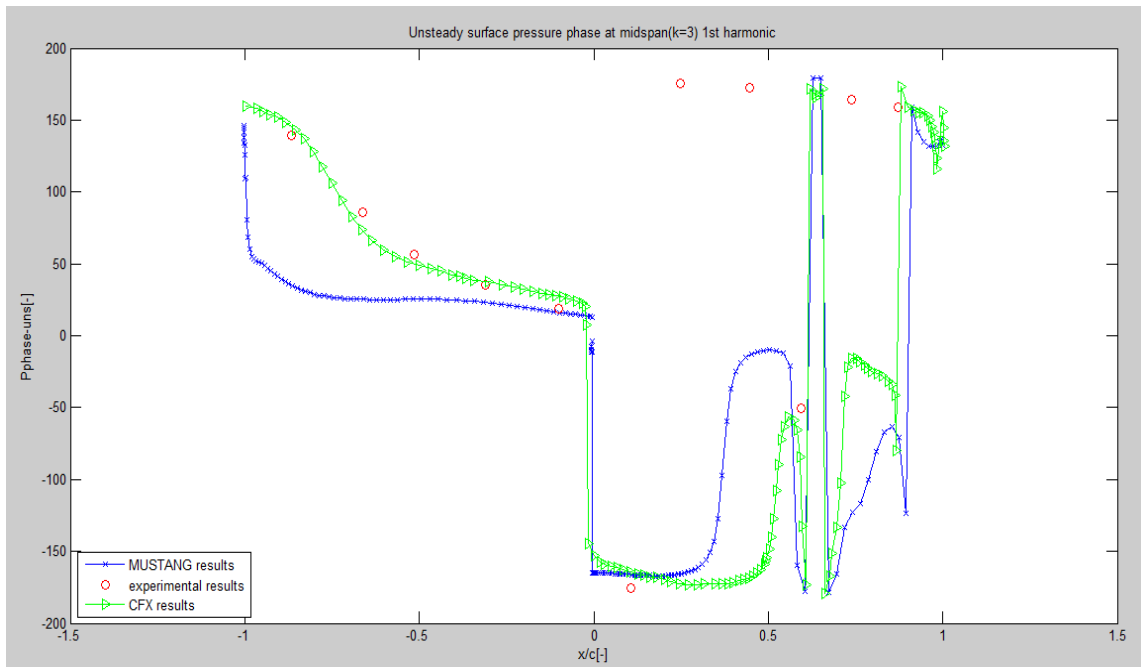


Figure 6.3: 1<sup>st</sup> harmonic phase shift of the surface unsteady pressure at midspan ( $k=3$ ),  $IBPA = 180^\circ$  from MUSTANG, ANSYS CFX 13.0, and experimental data

Then, Fig. 6.4 and Fig. 6.5 show the amplitude and the phase shift, respectively, of the 1<sup>st</sup> harmonic of the surface unsteady pressure from MUSTANG, ANSYS CFX, and the experimental data for  $IBPA = 270^\circ$ , where flutter most probably occurs based on experimental data. As can be seen from Fig. 6.4 and Fig. 6.5, the amplitude and phase from MUSTANG in general captures the trend of the experimental data at both the pressure side and up to 50% chord at suction side where the shock occurs but with some deviation. In addition, compared with the experimental data, the CFX simulation is better in Fig. 6.4 and no better in Fig. 6.5 than MUSTANG. Again, this difference can be partly attributed to the fineness of the mesh and the difference between quasi 3D coarse mesh and 3D finer mesh and to the neglect of the tip clearance in MUSTANG.

Downstream of the shock position, it is difficult to evaluate the accuracy of the MUSTANG and ANSYS CFX due to the sparseness of the experimental data.

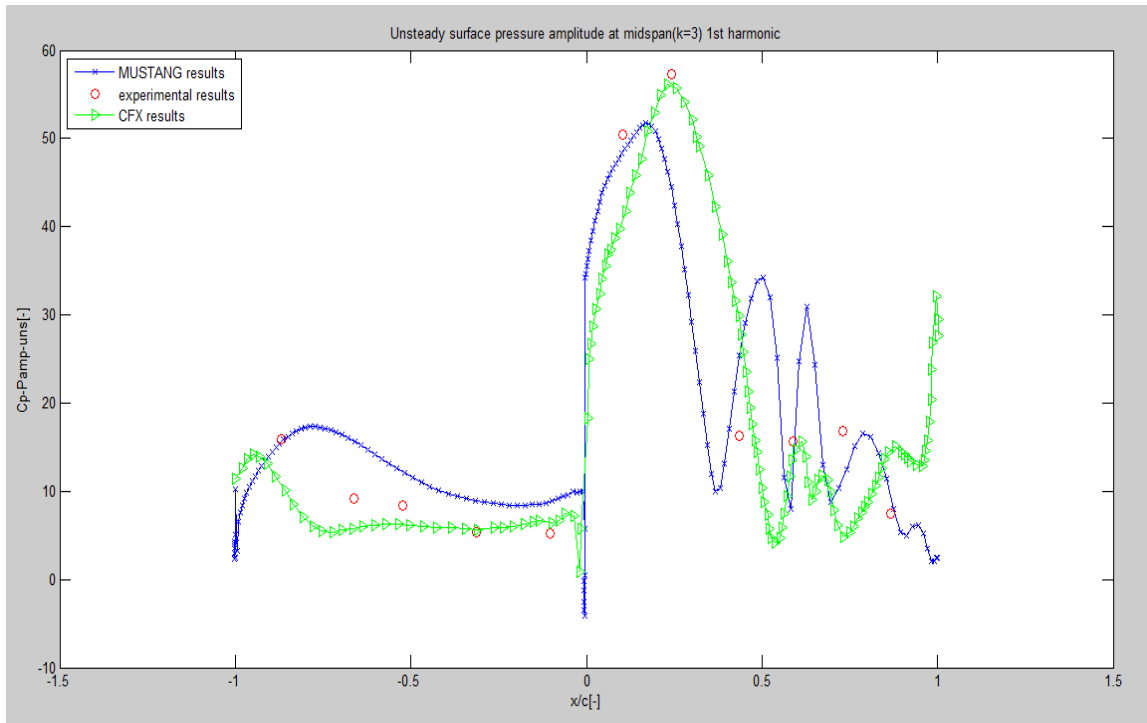


Figure 6.4: 1<sup>st</sup> harmonic amplitude of the surface unsteady pressure at midspan (k=3),  $IBPA = 270^\circ$  from MUSTANG, ANSYS CFX 13.0, and experimental data

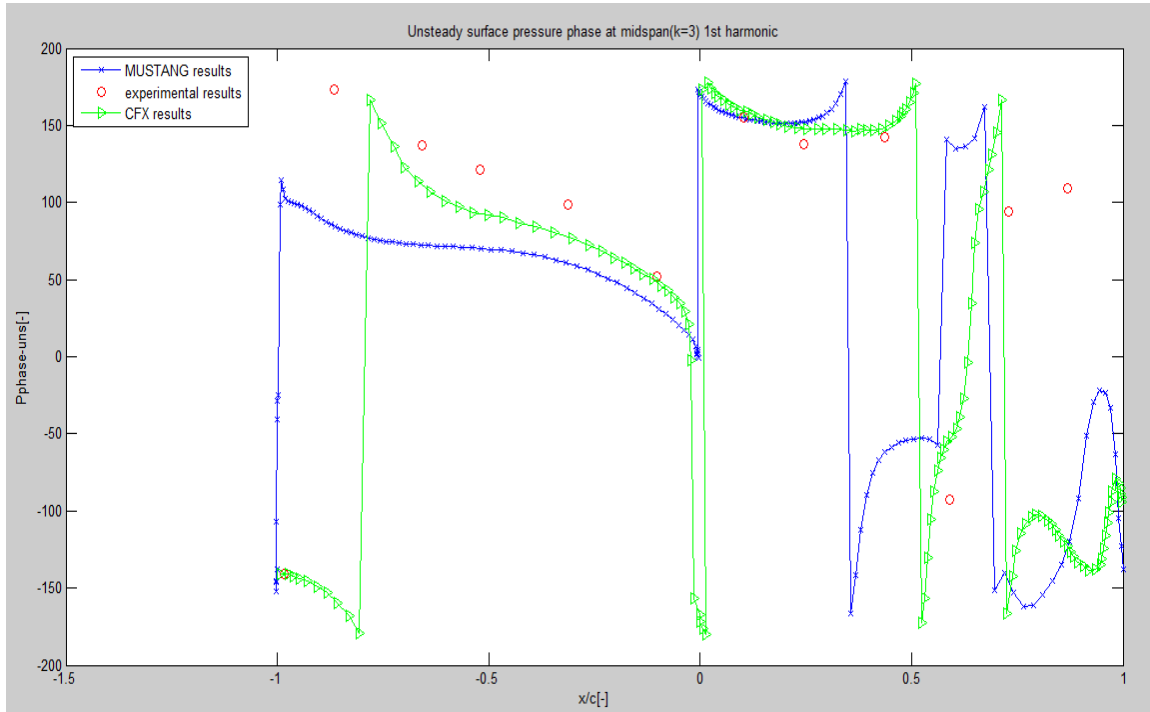


Figure 6.5: 1<sup>st</sup> harmonic phase shift of the surface unsteady pressure at midspan ( $k=3$ ),  $IBPA = 270^\circ$  from MUSTANG, ANSYS CFX 13.0, and experimental data

Finally, as discussed in Chapter 3, the flutter stability is directly related to the sign of the aerodynamic work, which further depends on the imaginary part of the unsteady generalized force according to Eq. 3.18. In Fig. 6.6, the real parts and the imaginary parts of the unsteady generalized force amplitude calculated at different IBPA's are plotted.

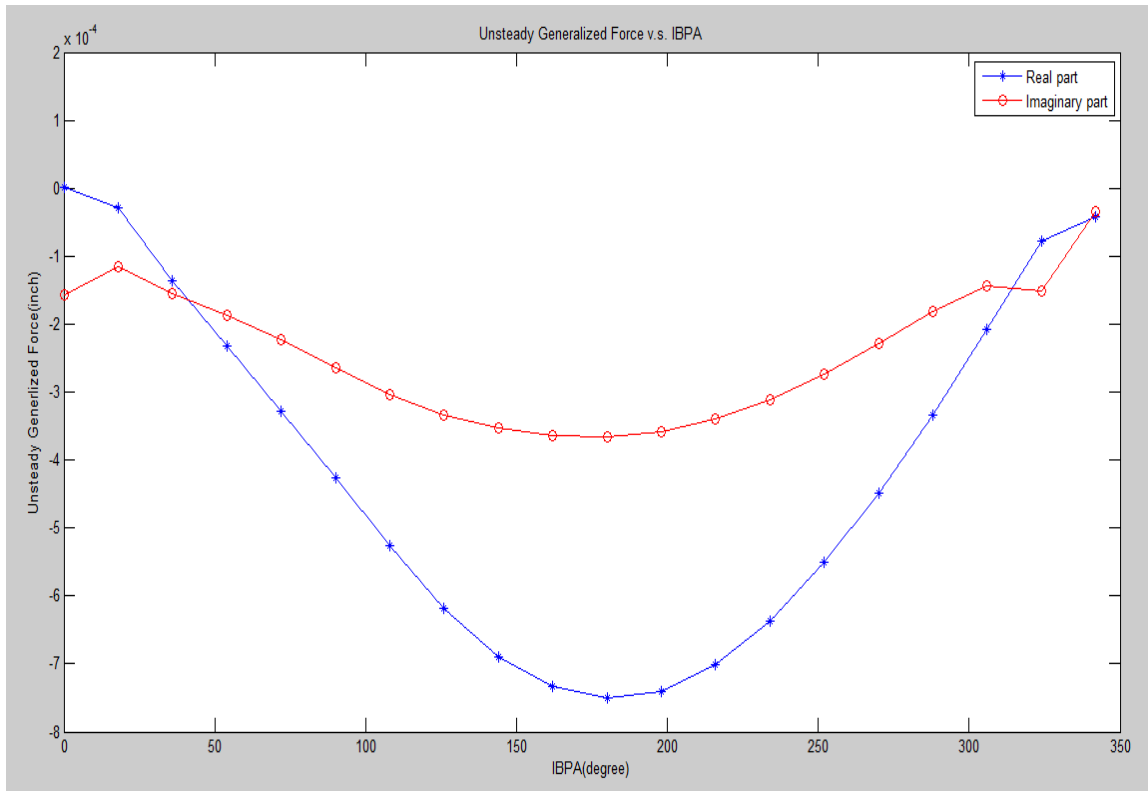


Figure 6.6: Real part and Imaginary part of the unsteady generalized force amplitude at different IBPA's.

In Fig. 6.6, the imaginary parts of the unsteady generalized force amplitude (1<sup>st</sup> harmonic) are negative at all IBPA's, which, based on Eq. 3.18, signifies that the aerodynamic work per cycle exerted by the fluid to the structure is negative. Hence, flutter will not occur for all IBPA's according to this analysis. Then, according to Eq. 3.18 and Eq. 3.19, the aerodynamic damping coefficient can be calculated from the imaginary parts of the unsteady generalized force amplitude (1<sup>st</sup> harmonic). Fig. 6.7 shows the stability curve of the MUSTANG results and the experimental data. As can be seen from Fig. 6.7, in the experimental data there is some region (from  $IBPA = 216^\circ$  to

$IBPA = 342^\circ$ ) where the flutter can occur. While in MUSTANG, the structure is stable for all IBPA's. According to Fig. 6.7, the general trend of the results from MUSTANG shows that the flutter stability is dependent on the IBPA. As is shown in Fig. 6.7, the mean value of the aerodynamics damping coefficients calculated from MUSTANG is larger than in the experiment. In principle, the mean value of the aerodynamic damping coefficients is the blade-self damping coefficient, in which only the blade in analysis is considered vibrating while the adjacent blades are assumed to be non-vibrating. The influences from the adjacent vibrating blades serve as higher order harmonics which "enrich" or "adjust" the aerodynamic damping coefficient curve. Hence, Fig. 6.7 illustrates that the biggest deviation comes from the blade-self damping coefficient.

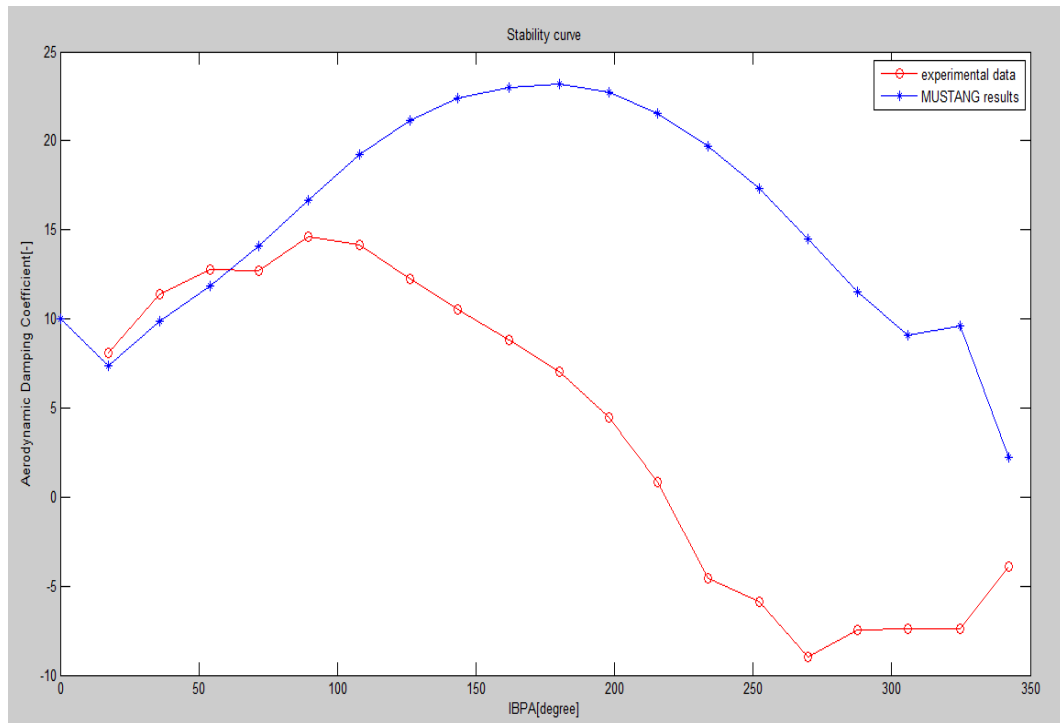


Figure 6.7: Stability curves of MUSTANG results and experimental data

This deviation might be partly attributed to the sparseness of the pressure transducers in the experimental case. In the experimental data, there are only 11 pressure transducers at the blade surface, and the aerodynamic damping coefficient in the experimental data is calculated based on the measurement from those 11 sample points. In contrast, 161 points, which is much denser than in the experiment, are sampled at the blade surface in MUSTANG. To visualize the influence of the number of sample points, Fig. 6.8 plots the stability curves based on the MUSTANG results by using 161 points and by using 11 points. Both results are compared with the experimental results. As is clearly shown in Fig. 6.8, the mean value of the aerodynamic damping coefficients calculated by using fewer sample points is in general smaller than those calculated by using more sample points.

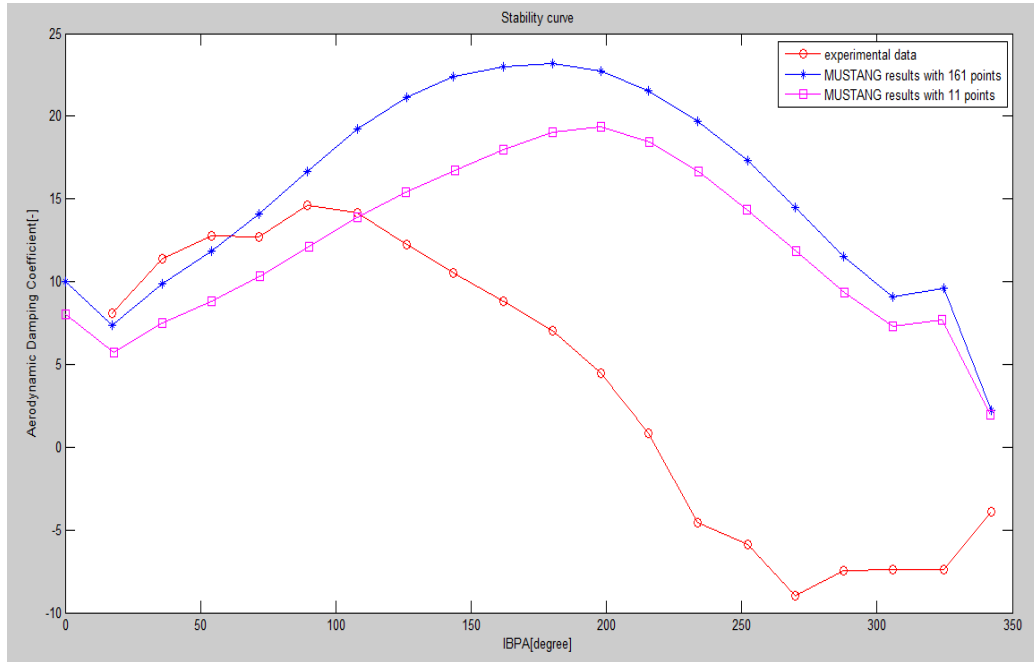


Figure 6.8: Stability curves of MUSTANG results by using 161 integration points and 11 integration points, compared with experimental results

### 6.3 Variation Cases

#### 6.3.1 Results with 110% and 90% Oscillating Frequency

When the blade oscillating frequency is 110% or 90% of the test case, the stability curves obtained from MUSTANG are plotted in Fig. 6.9.

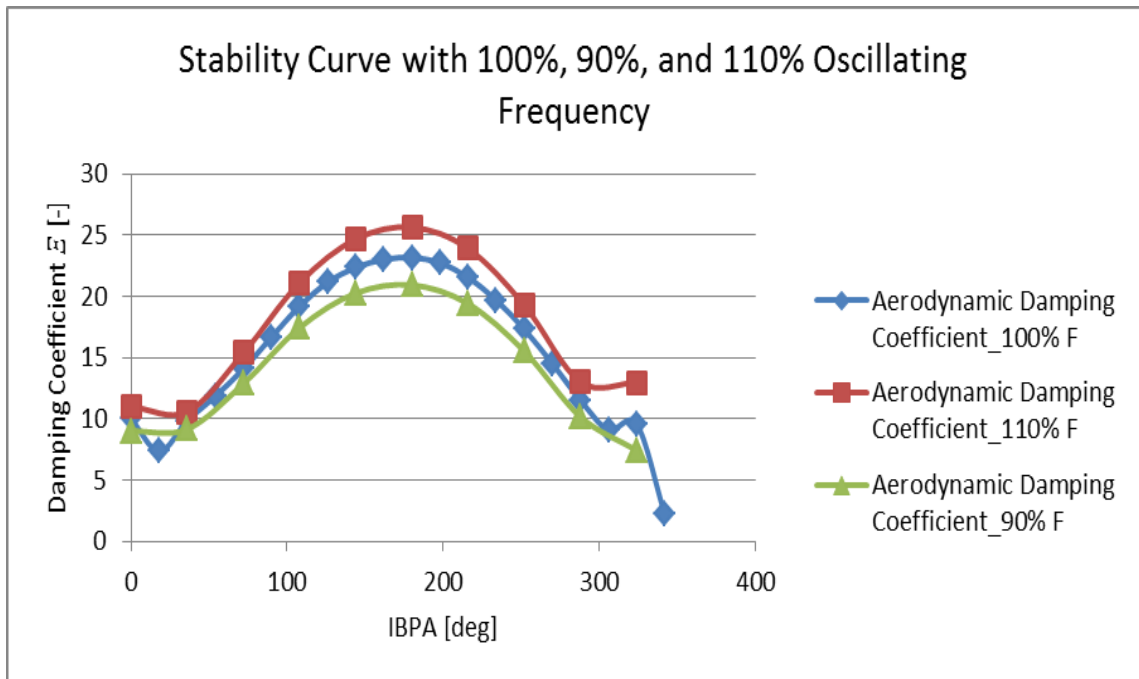


Figure 6.9: Stability curve with 100%, 90%, and 110% oscillating frequency

According to Fig. 6.9, When 110% vibrating frequency is applied to the blade, the structure will be more stable in terms of flutter stability than in the test case. In 90% vibrating frequency case, the structure will be less stable in terms of flutter stability. However, this factor alone doesn't explain the deviation of the stability curves from MUSTANG and the experimental data.

### 6.3.2 Results with 110% Pressure Ratio

As is mentioned in previous chapter, loading is another parameter which influences the flutter stability. When the pressure ratio across the blade row increases by 10% (by lowering the exit pressure), the stability curve is shown in Fig. 6.10.

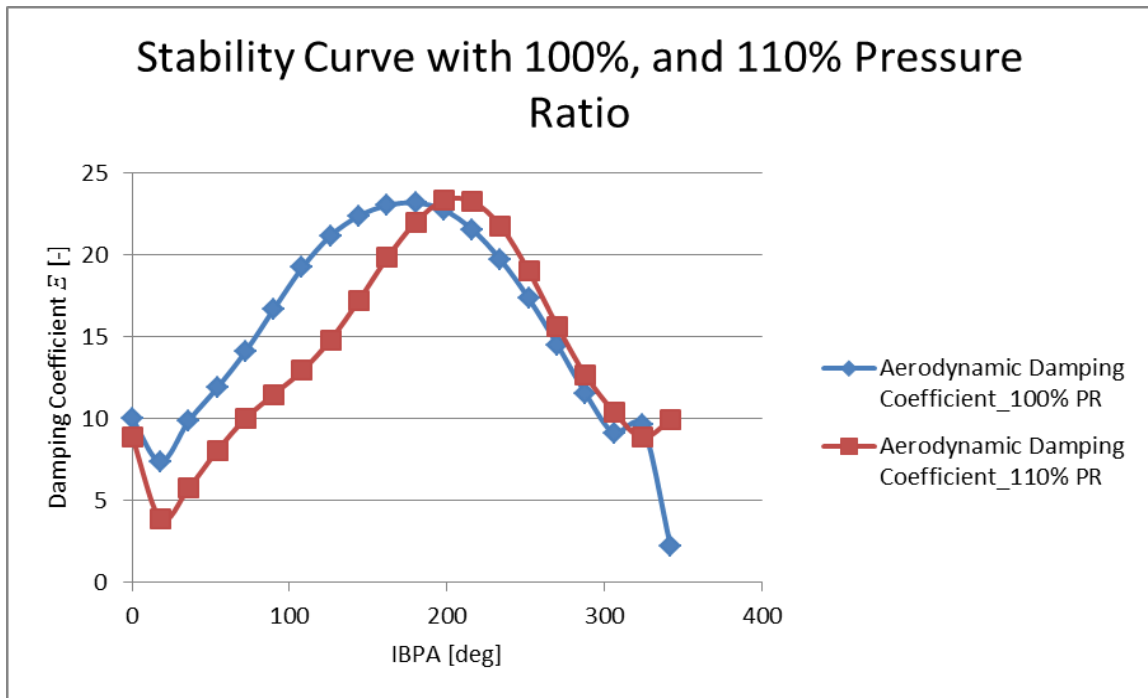


Figure 6.10: Stability curve with 100% and 110% pressure ratio

According to Fig. 6.10, the stability curve moves rightward and a little downward, meaning that the blade structure will be more stable in some region of IBPA's but less stable in other region of IBPA's. However, this factor alone doesn't explain the deviation of the stability curves from MUSTANG and the experimental data.

## 7 Conclusion and Future Work

### 7.1 Conclusion

According to the results in Chapter 6, the nonlinear MUSTANG code applied on a quasi 3D standard configuration 4 (C4) blade row can well predict the shock occurrence around mid-chord at suction side. Meanwhile, MUSTANG in general follows the trend of the unsteady flow behaviors at the pressure side and up to the 50% chord where shock occurs but with some deviation which might be attributed to the quasi-3D simplification and the neglect of tip clearance. However, just like other CFD solvers, MUSTANG fails to simulate the flow phenomena downstream the 55% chord where shock occurs due to the uncertainties in CFD prediction of the shock wave/boundary layer interaction. Furthermore, the stability curve from MUSTANG is inconsistent with that from the experimental data-might partially due to the sparseness of the pressure transducer in the experiment.

According to the results of the variation cases, small changes on the oscillating frequency and the pressure ratio have significant impact on the flutter stability of the blade structure. This fact indicates that some of the deviation in the stability curve between MUSTANG and the experiment might come from the small variation of the blade oscillating frequency and the pressure ratio.

Although part of the deviation can be attributed to the factors mentioned above, none of these reasons can perfectly explain the large differences of the aerodynamic damping coefficients between the MUSTANG results and the experimental data.

## **7.2 Future Work**

In future work, further investigation on the deviation in the stability curve can be studied. Instead of using quasi 3D mesh, a full 3D grid with tip clearance will be applied, which is expected to increase the simulation accuracy.

In addition, flutter stability under different bending directions can be analyzed to evaluate how variations of bending direction affect the flutter stability of the structure.

Furthermore, more research is needed to study the complexity of the suction side region where shock occurs, reflects, and interacts with the boundary layer.

Correspondingly, sophisticated turbulence models are required to capture the spurious phenomena downstream of the shock position on suction side.

Finally, both flutter and forced response will be studied simultaneously.

# Appendix

## A Additional Graphs

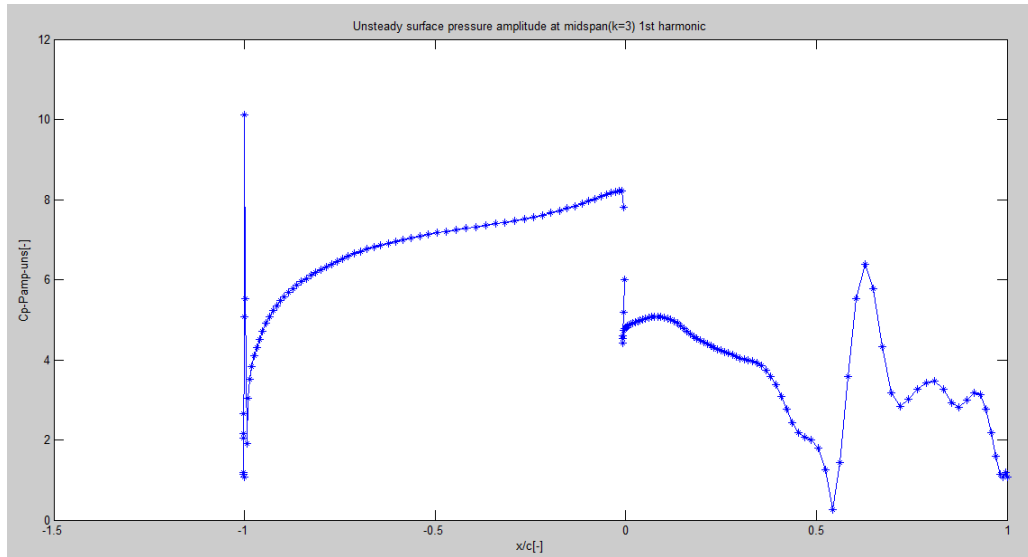


Figure 8.1: Unsteady surface pressure 1<sup>st</sup> harmonic amplitude at midspan (k=3) for  $IBPA = 0^\circ$

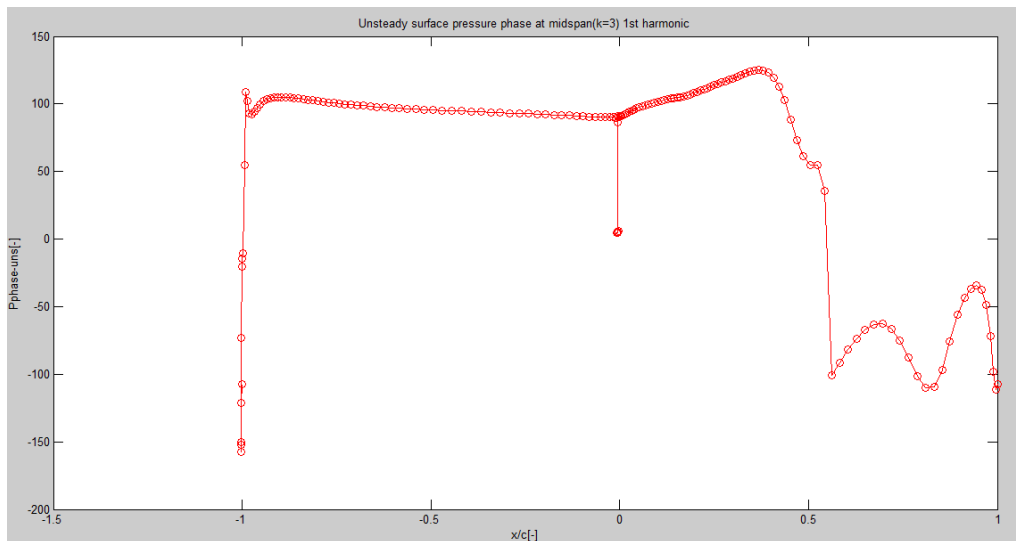


Figure 8.2: Unsteady surface pressure 1<sup>st</sup> harmonic phase at midspan (k=3) for  $IBPA = 0^\circ$

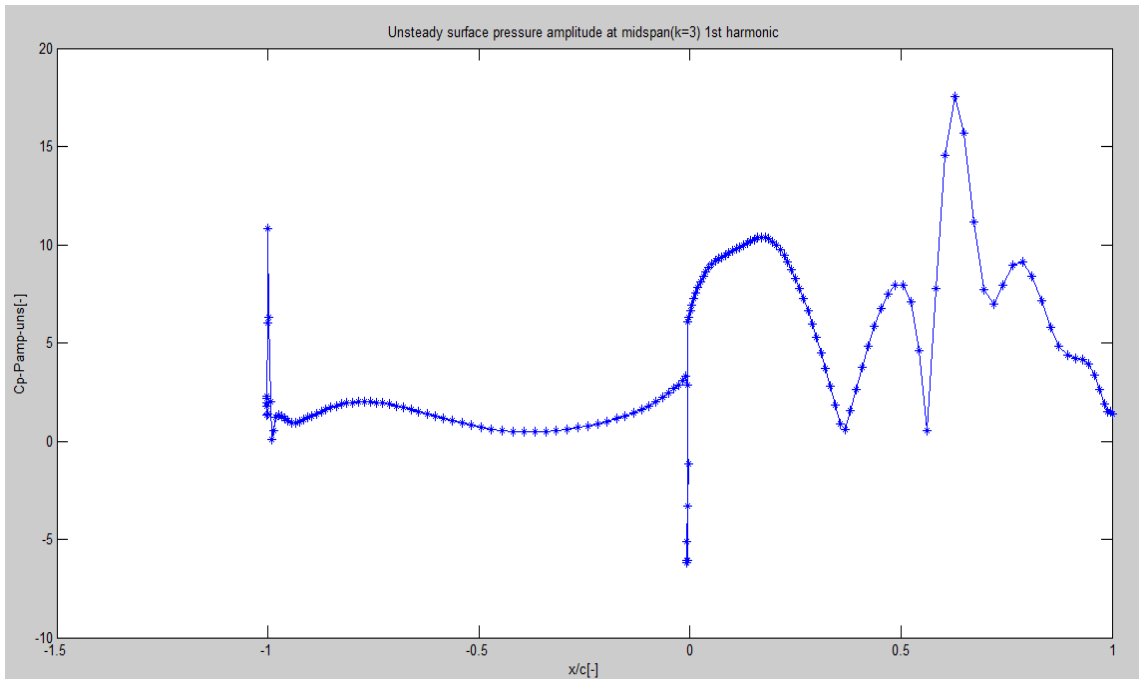


Figure 8.3: Unsteady surface pressure 1<sup>st</sup> harmonic amplitude at midspan (k=3) for  $IBPA = 18^\circ$

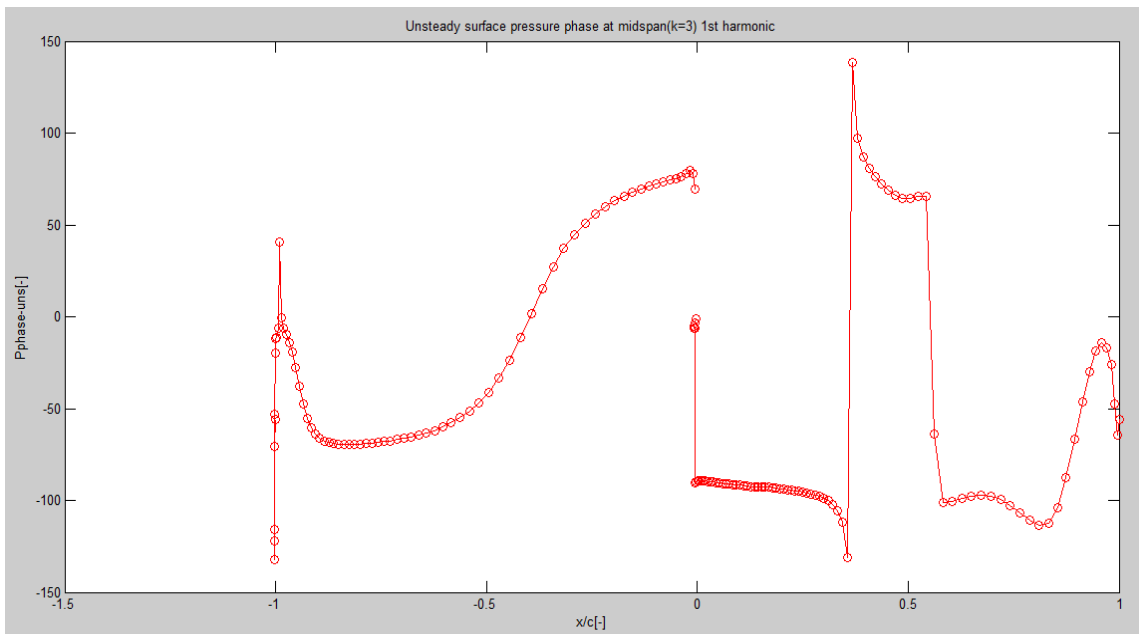


Figure 8.4: Unsteady surface pressure 1<sup>st</sup> harmonic phase at midspan (k=3) for  $IBPA = 18^\circ$

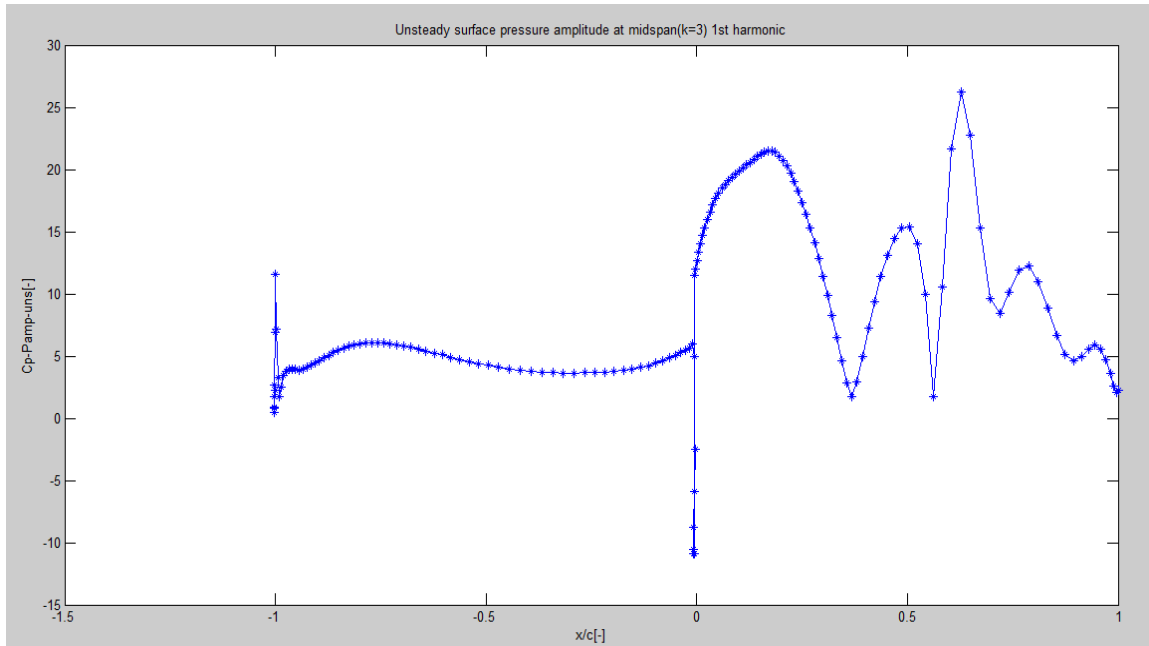


Figure 8.5: Unsteady surface pressure 1<sup>st</sup> harmonic amplitude at midspan (k=3) for  $IBPA = 36^\circ$

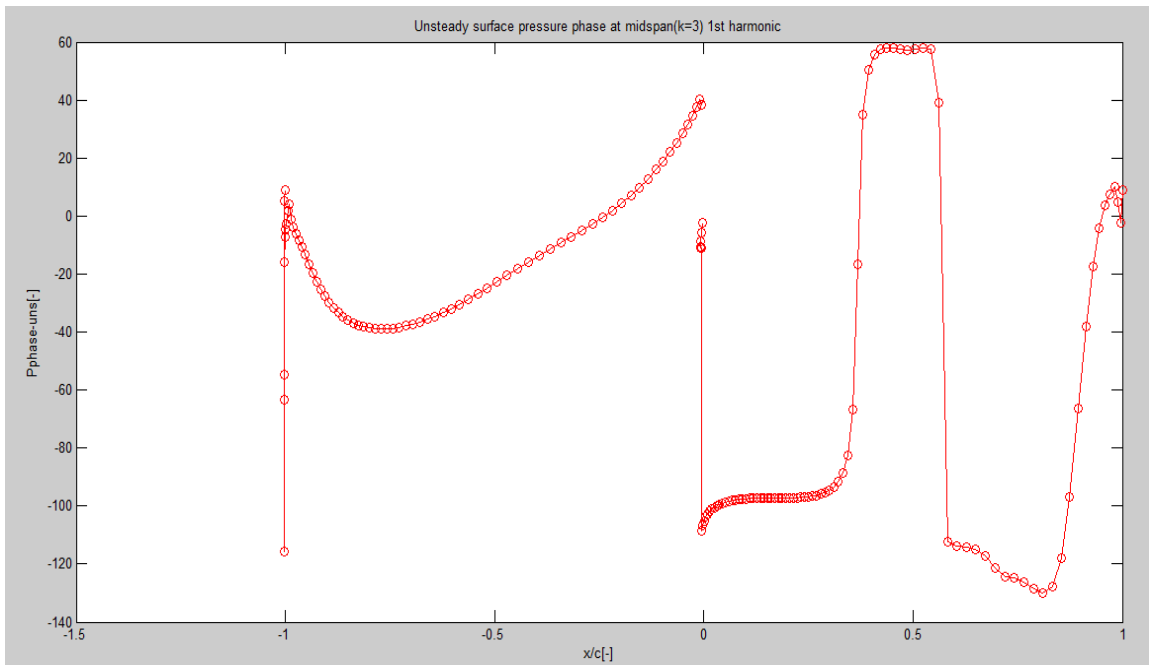


Figure 8.6: Unsteady surface pressure 1<sup>st</sup> harmonic phase at midspan (k=3) for  $IBPA = 36^\circ$

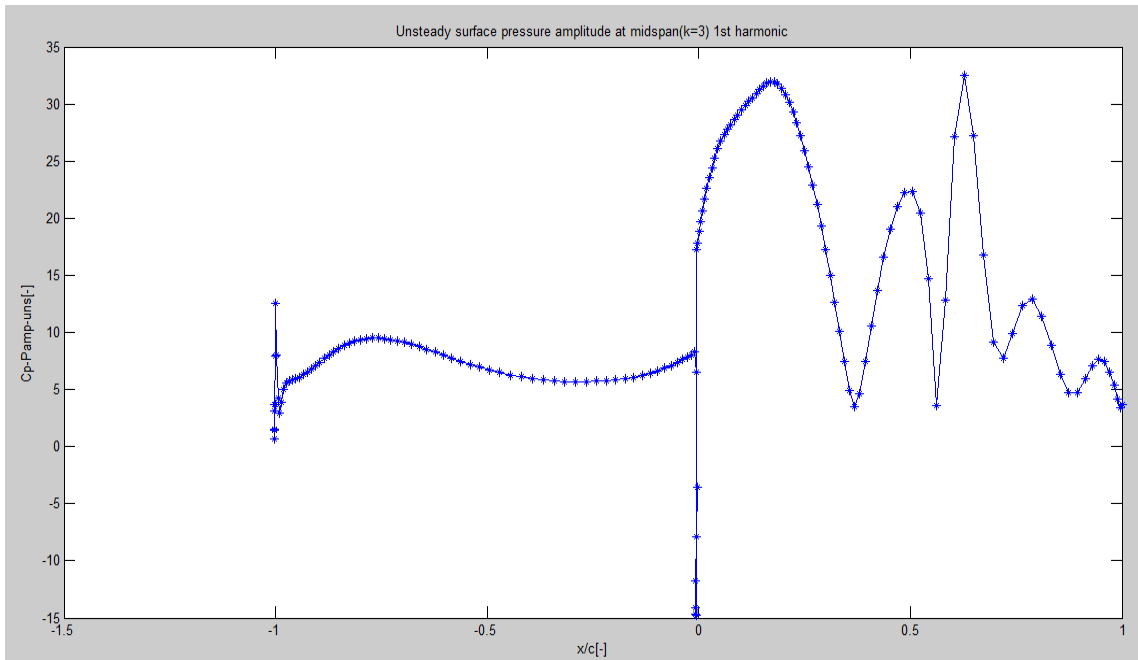


Figure 8.7: Unsteady surface pressure 1<sup>st</sup> harmonic amplitude at midspan (k=3) for  $IBPA = 54^\circ$

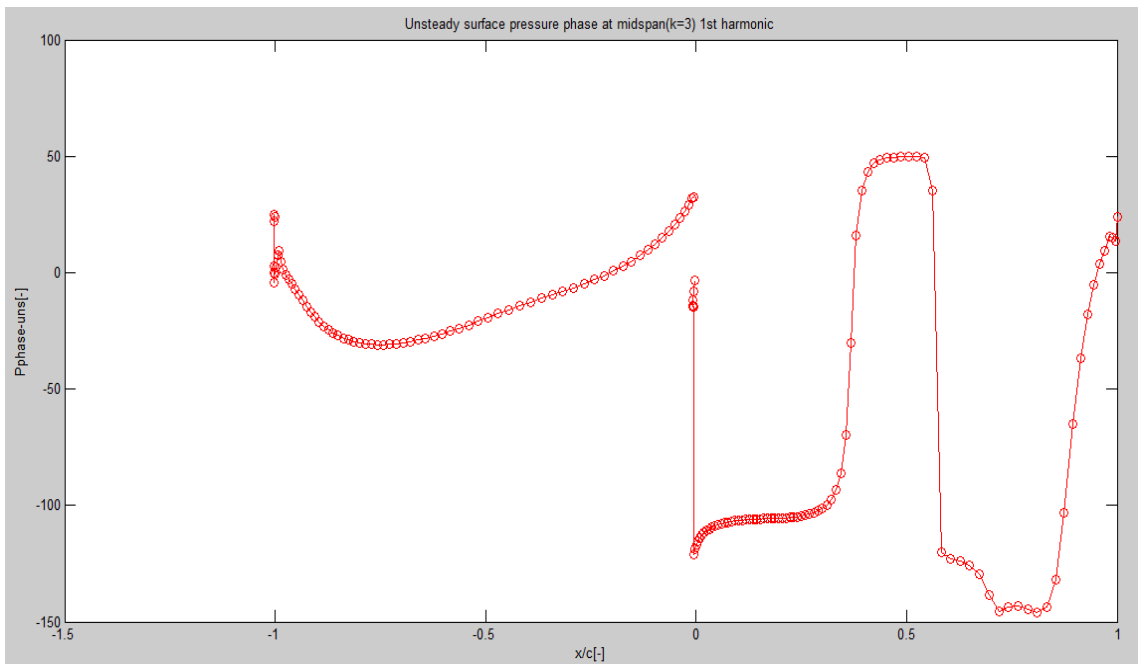


Figure 8.8: Unsteady surface pressure 1<sup>st</sup> harmonic phase at midspan (k=3) for  $IBPA = 54^\circ$

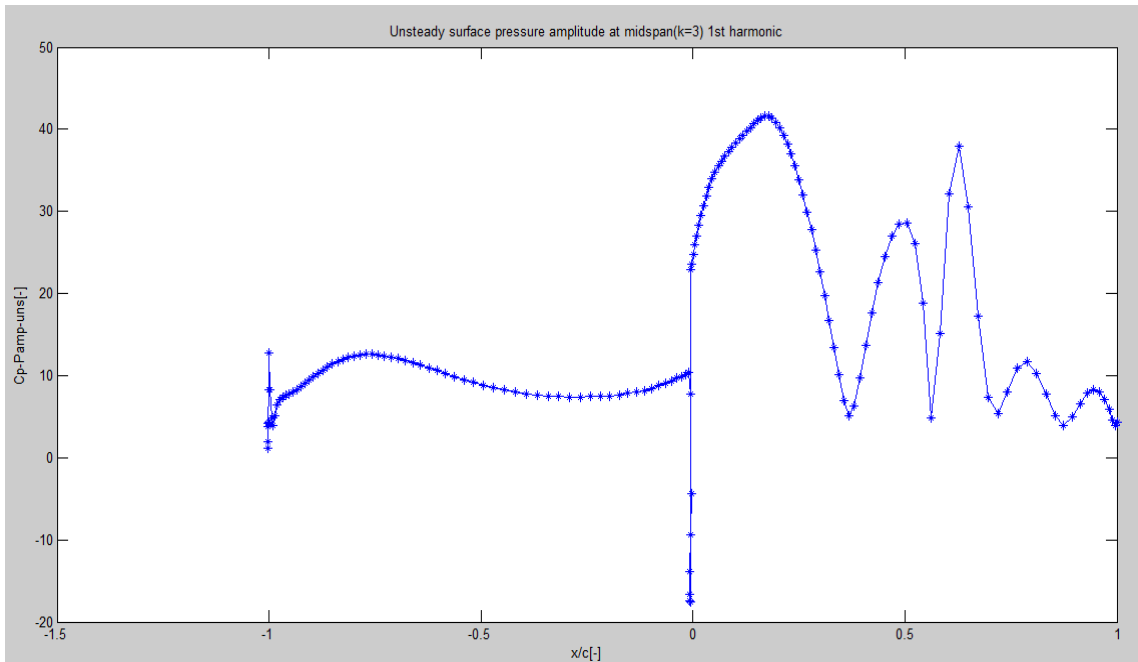


Figure 8.9: Unsteady surface pressure 1<sup>st</sup> harmonic amplitude at midspan ( $k=3$ ) for  $IBPA = 72^\circ$

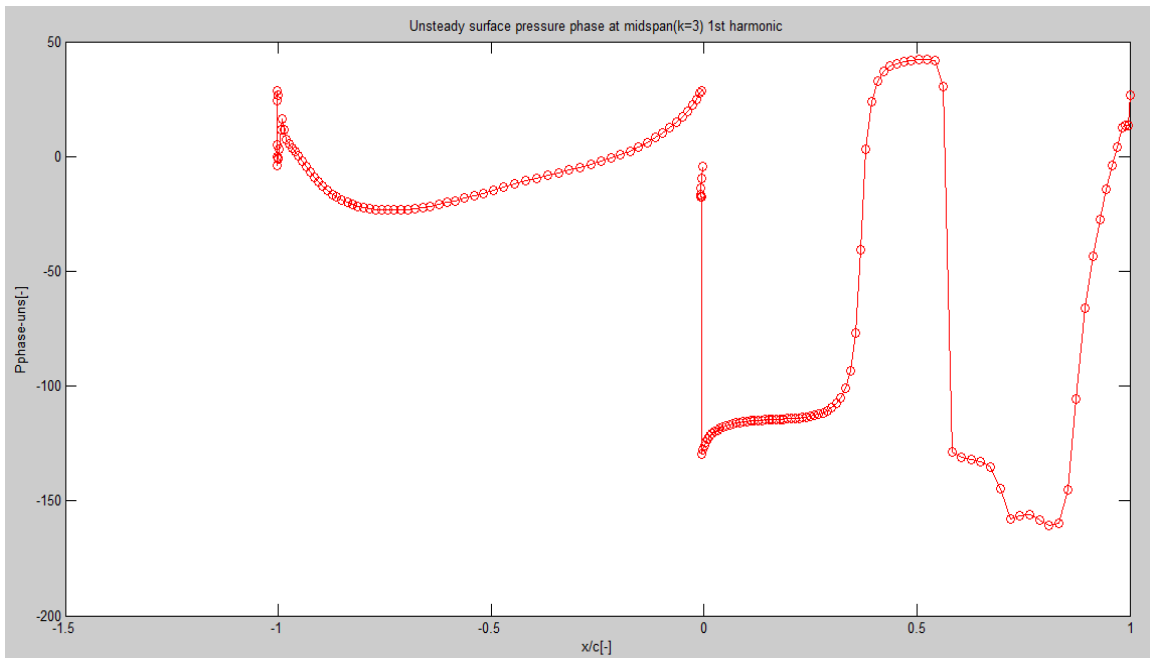


Figure 8.10: Unsteady surface pressure 1<sup>st</sup> harmonic phase at midspan ( $k=3$ ) for  $IBPA = 72^\circ$

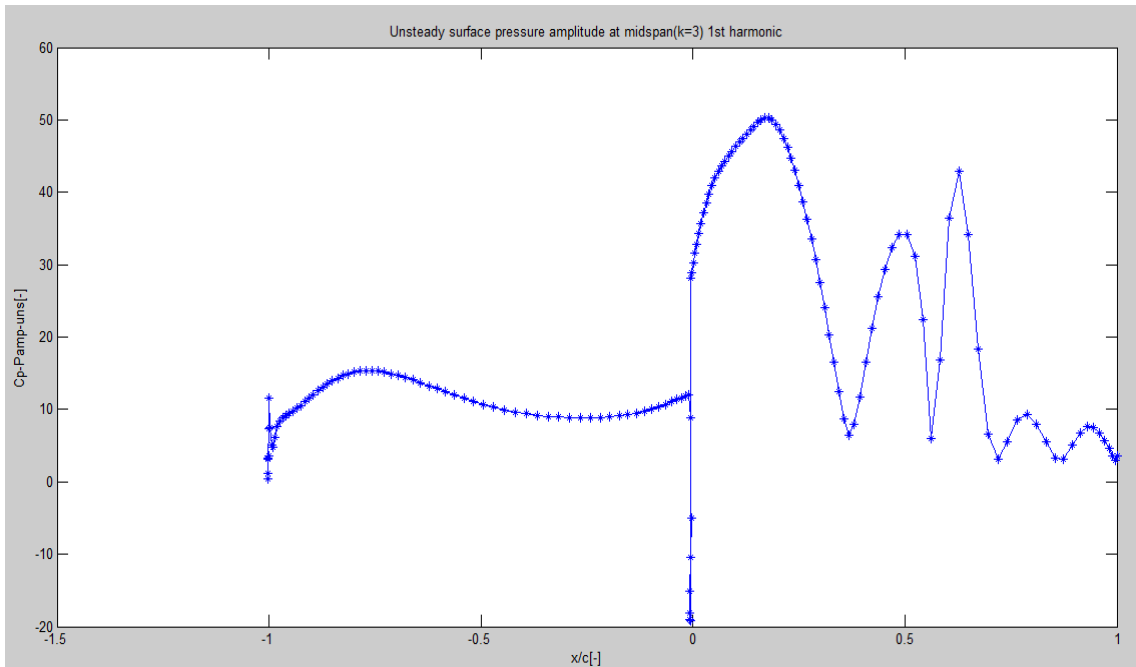


Figure 8.11: Unsteady surface pressure 1<sup>st</sup> harmonic amplitude at midspan ( $k=3$ ) for  $IBPA = 90^\circ$

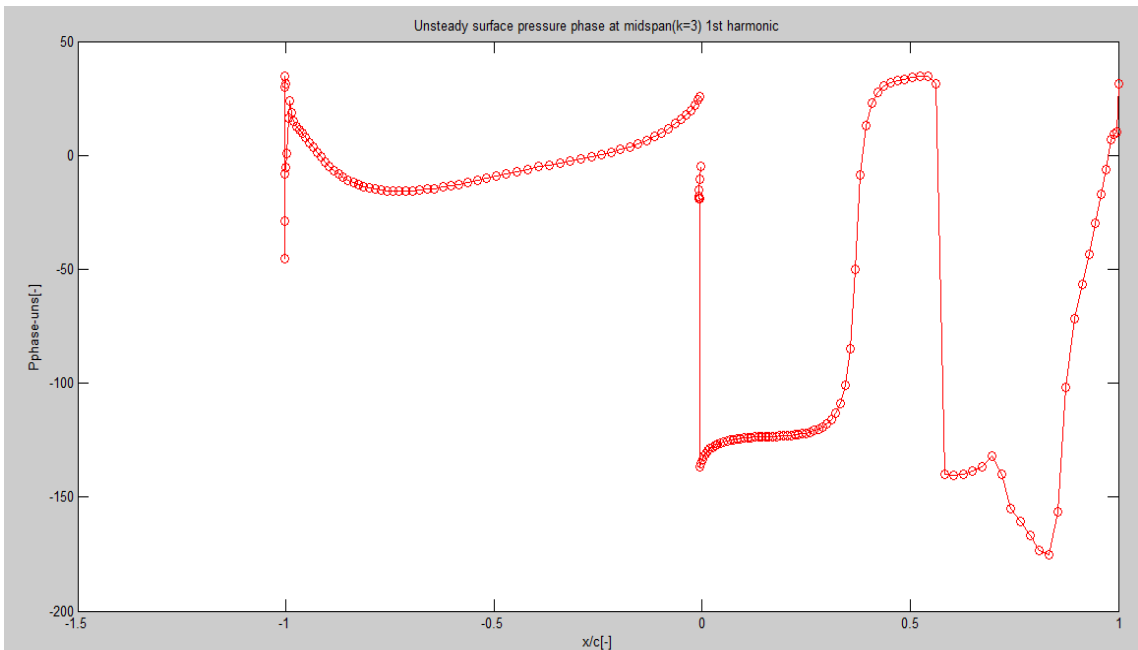


Figure 8.12: Unsteady surface pressure 1<sup>st</sup> harmonic phase at midspan ( $k=3$ ) for  $IBPA = 90^\circ$

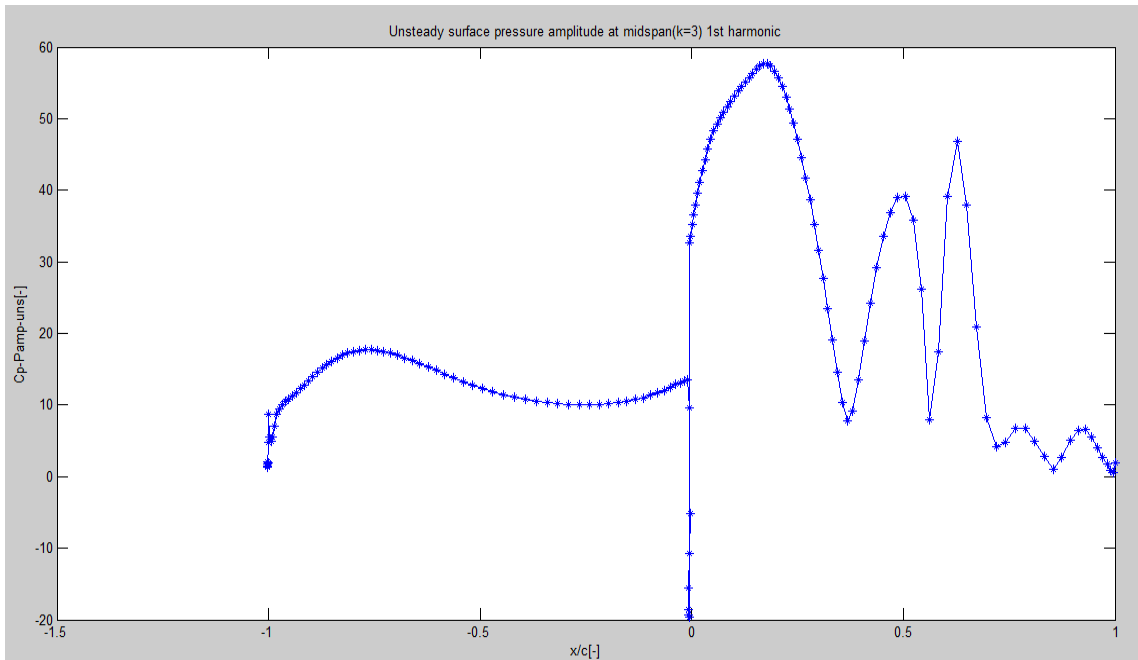


Figure 8.13: Unsteady surface pressure 1<sup>st</sup> harmonic amplitude at midspan ( $k=3$ ) for  $IBPA = 108^\circ$

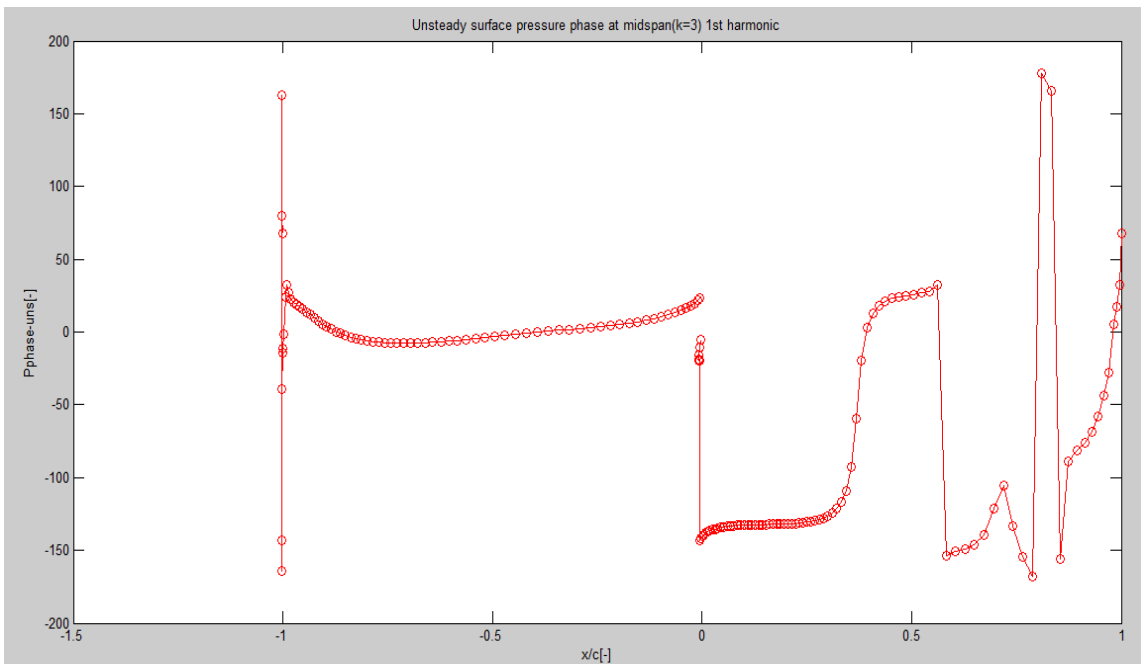


Figure 8.14: Unsteady surface pressure 1<sup>st</sup> harmonic phase at midspan ( $k=3$ ) for  $IBPA = 108^\circ$

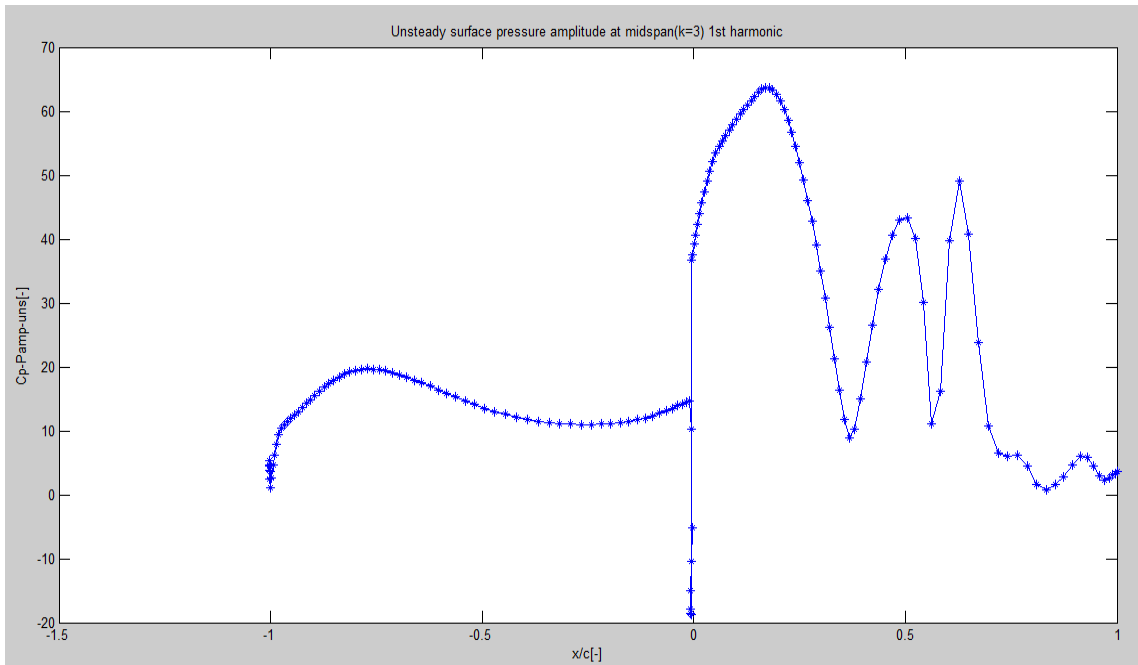


Figure 8.15: Unsteady surface pressure 1<sup>st</sup> harmonic amplitude at midspan (k=3) for  $IBPA = 126^\circ$

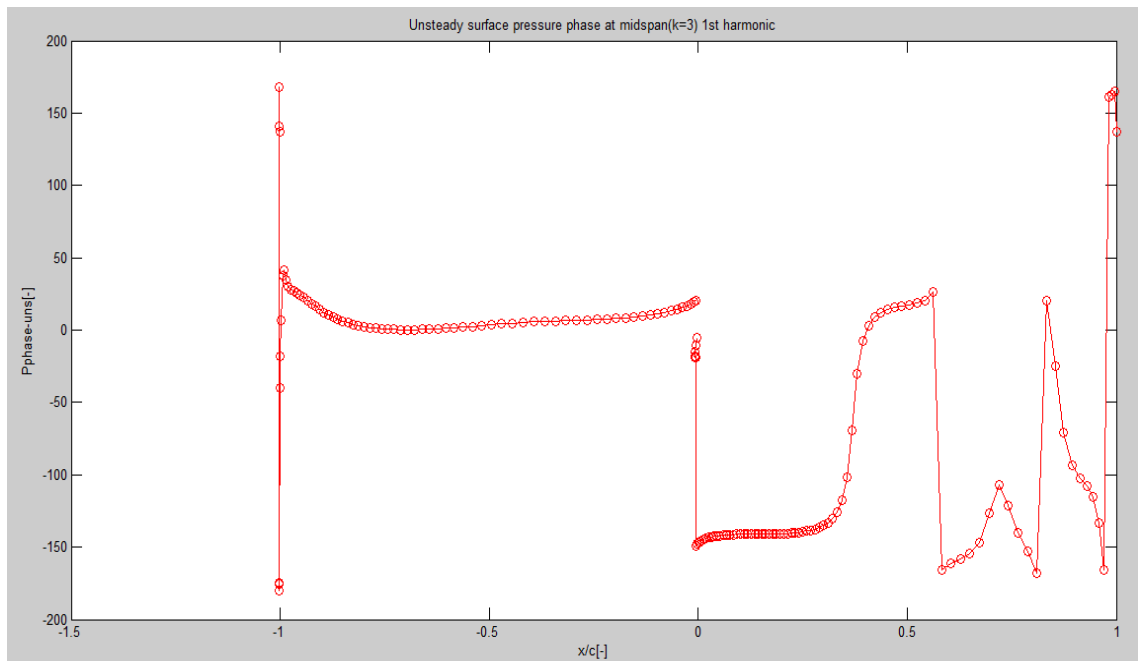


Figure 8.16: Unsteady surface pressure 1<sup>st</sup> harmonic phase at midspan (k=3) for  $IBPA = 126^\circ$

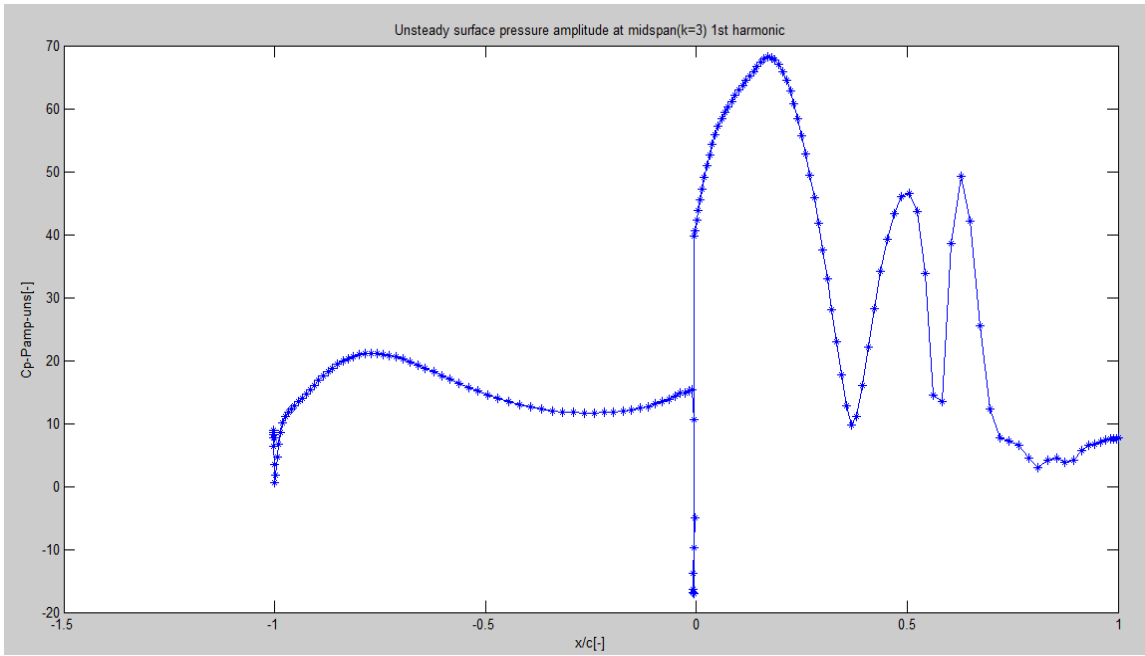


Figure 8.17: Unsteady surface pressure 1<sup>st</sup> harmonic amplitude at midspan ( $k=3$ ) for  $IBPA = 144^\circ$

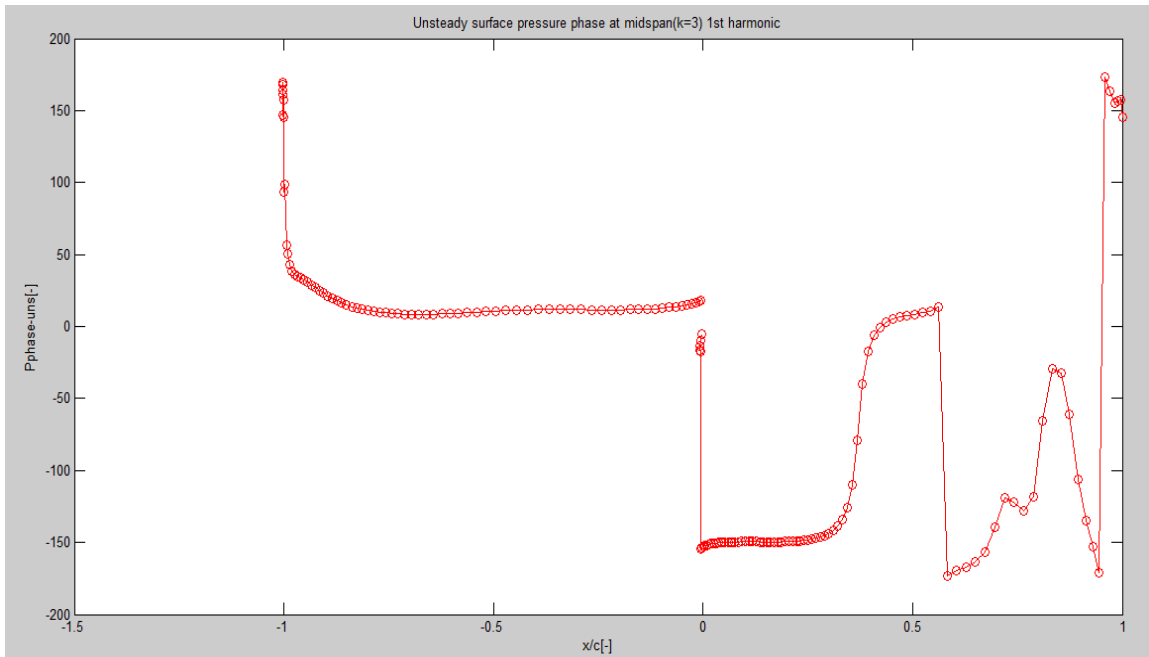


Figure 8.18: Unsteady surface pressure 1<sup>st</sup> harmonic phase at midspan ( $k=3$ ) for  $IBPA = 144^\circ$

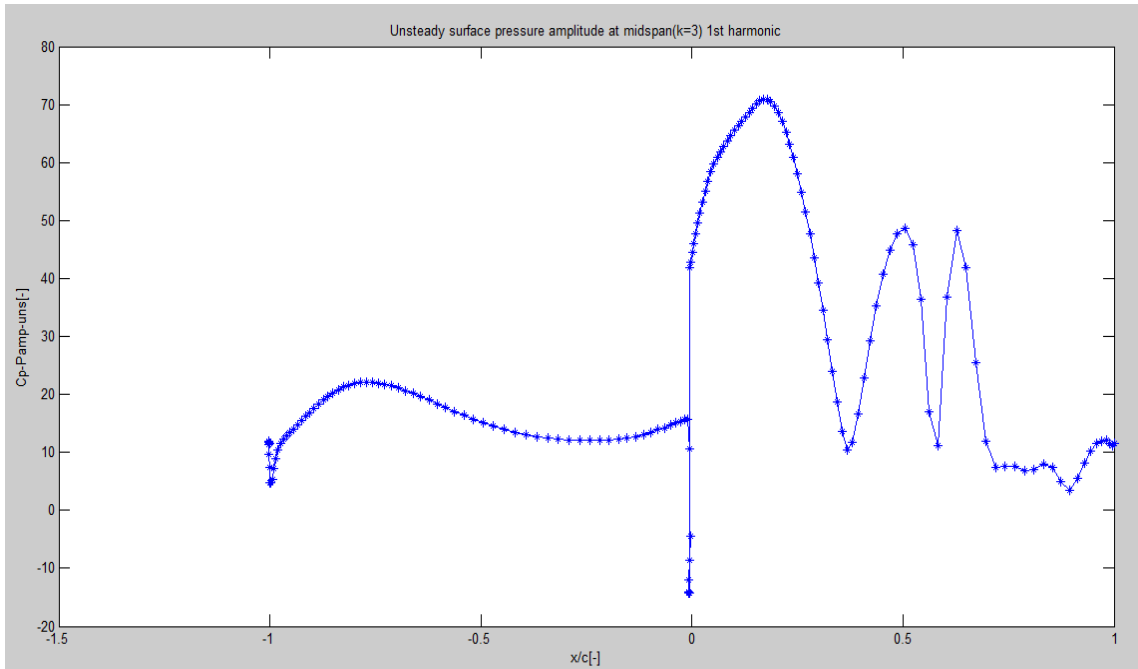


Figure 8.19: Unsteady surface pressure 1<sup>st</sup> harmonic amplitude at midspan ( $k=3$ ) for  $IBPA = 162^\circ$

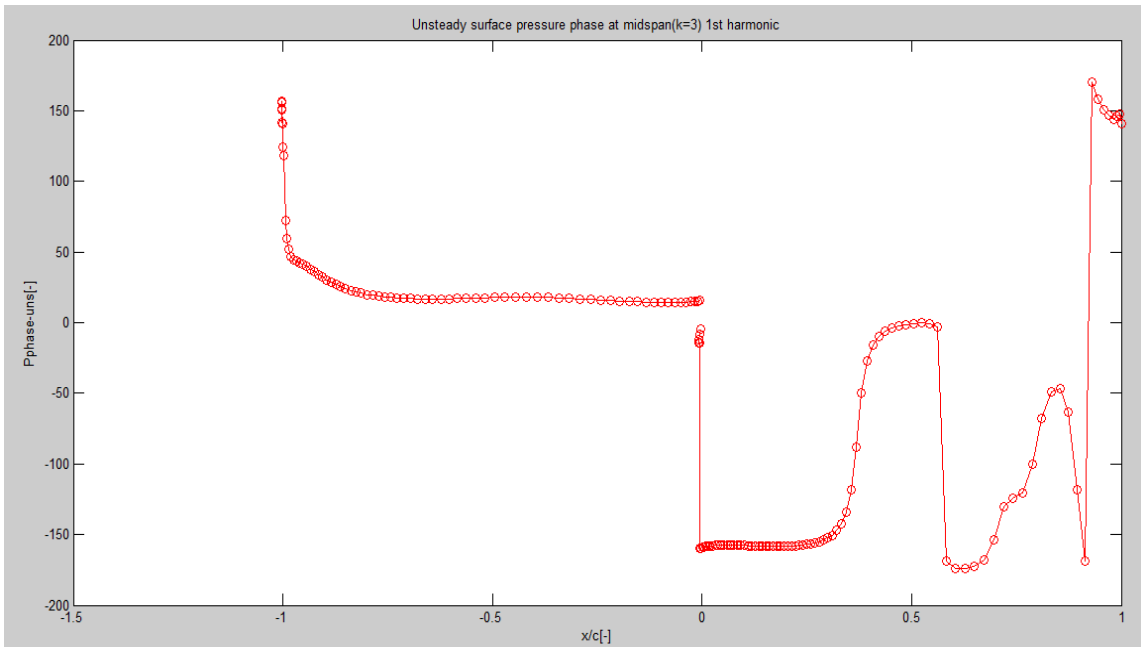


Figure 8.20: Unsteady surface pressure 1<sup>st</sup> harmonic phase at midspan ( $k=3$ ) for  $IBPA = 162^\circ$

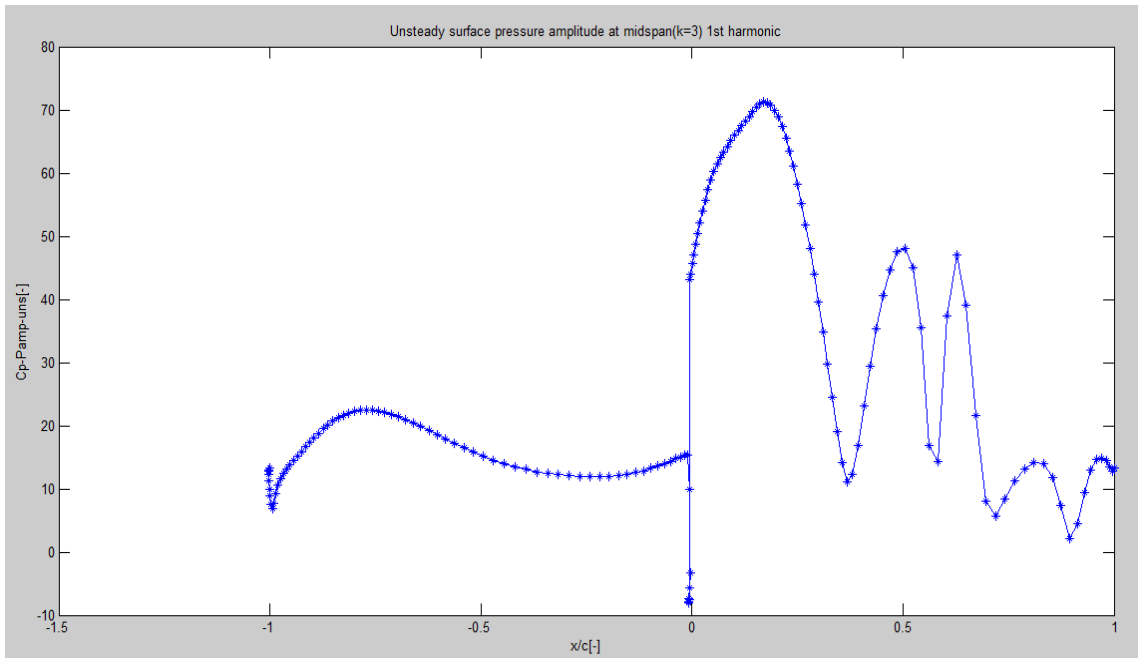


Figure 8.21: Unsteady surface pressure 1<sup>st</sup> harmonic amplitude at midspan ( $k=3$ ) for  $IBPA = 198^\circ$

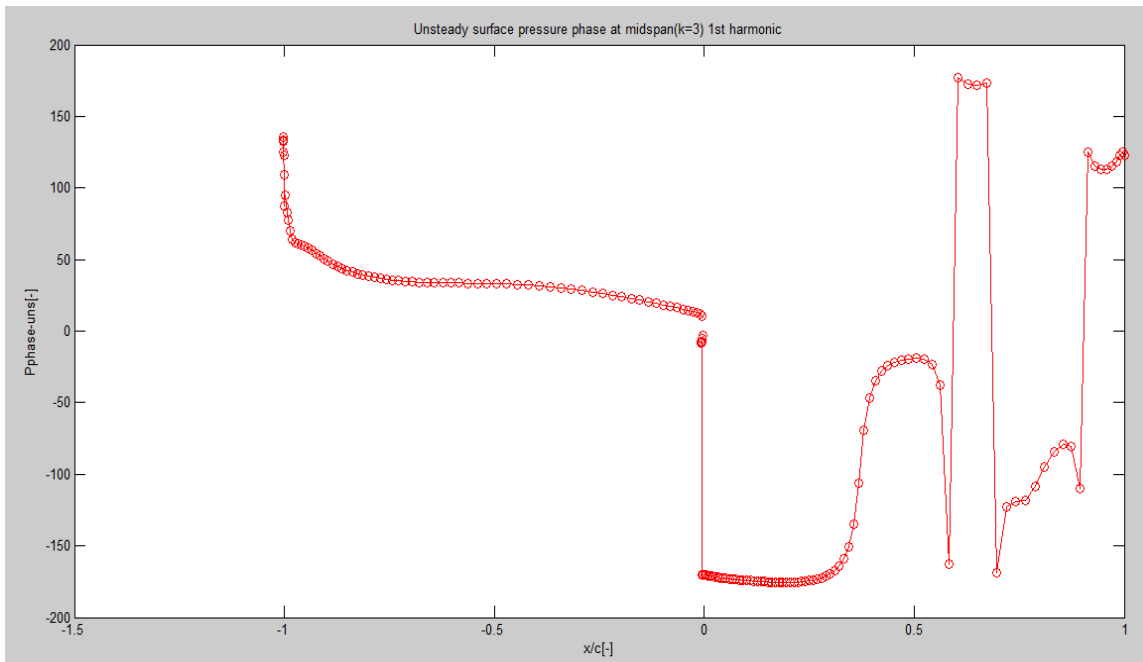


Figure 8.22: Unsteady surface pressure 1<sup>st</sup> harmonic phase at midspan ( $k=3$ ) for  $IBPA = 198^\circ$

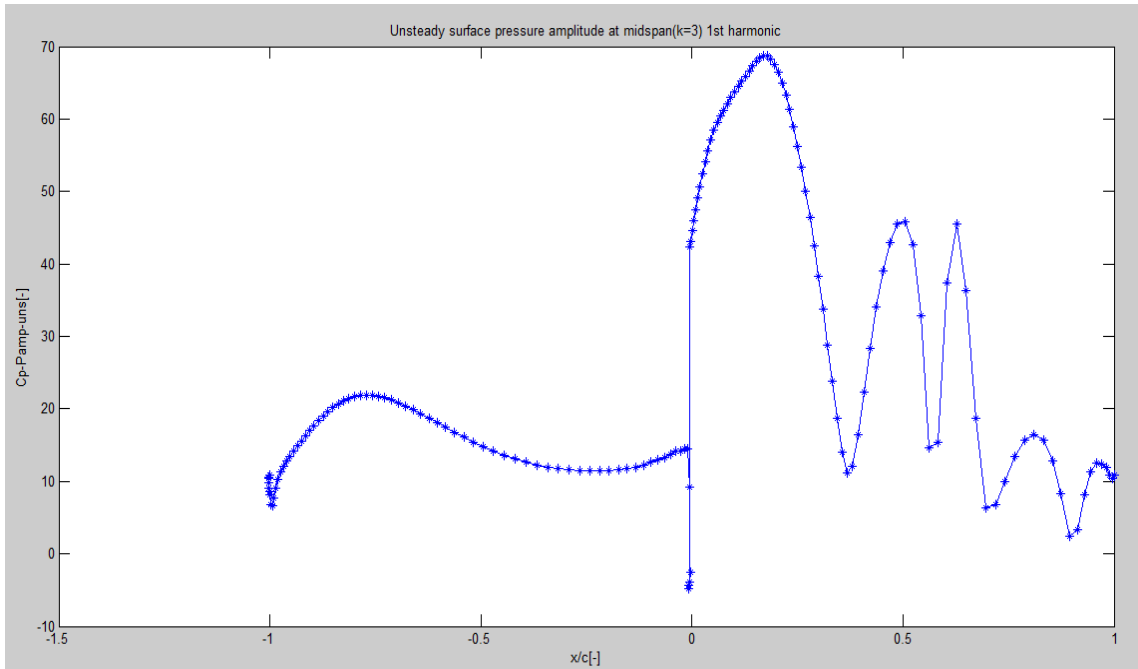


Figure 8.23: Unsteady surface pressure 1<sup>st</sup> harmonic amplitude at midspan (k=3) for  $IBPA = 216^\circ$

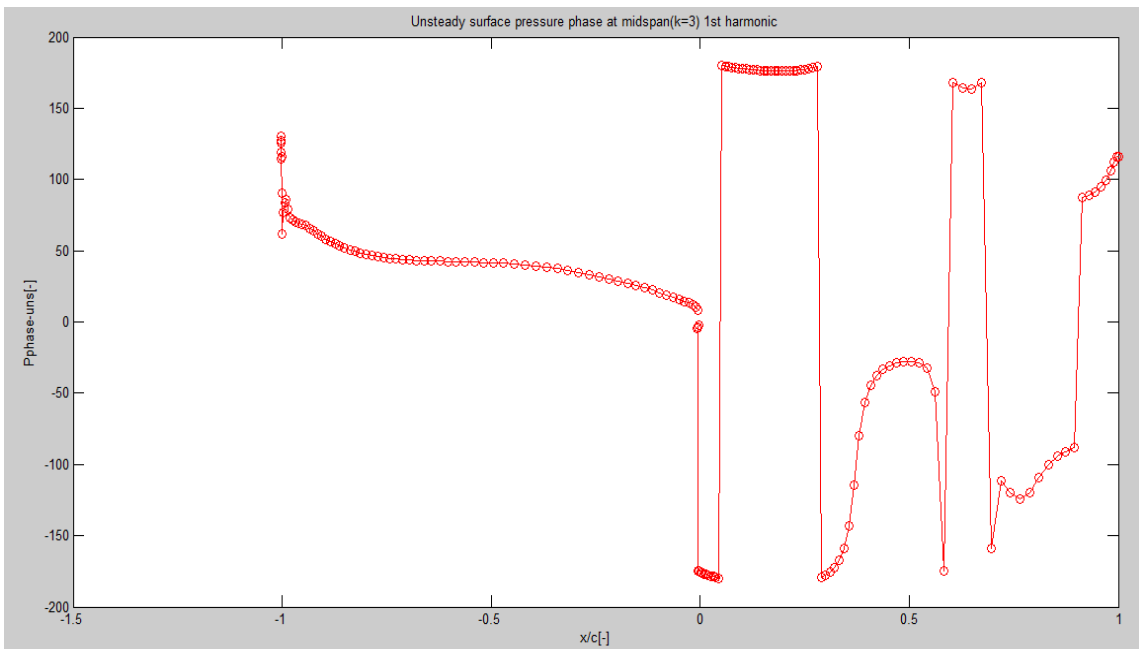


Figure 8.24: Unsteady surface pressure 1<sup>st</sup> harmonic phase at midspan (k=3) for  $IBPA = 216^\circ$

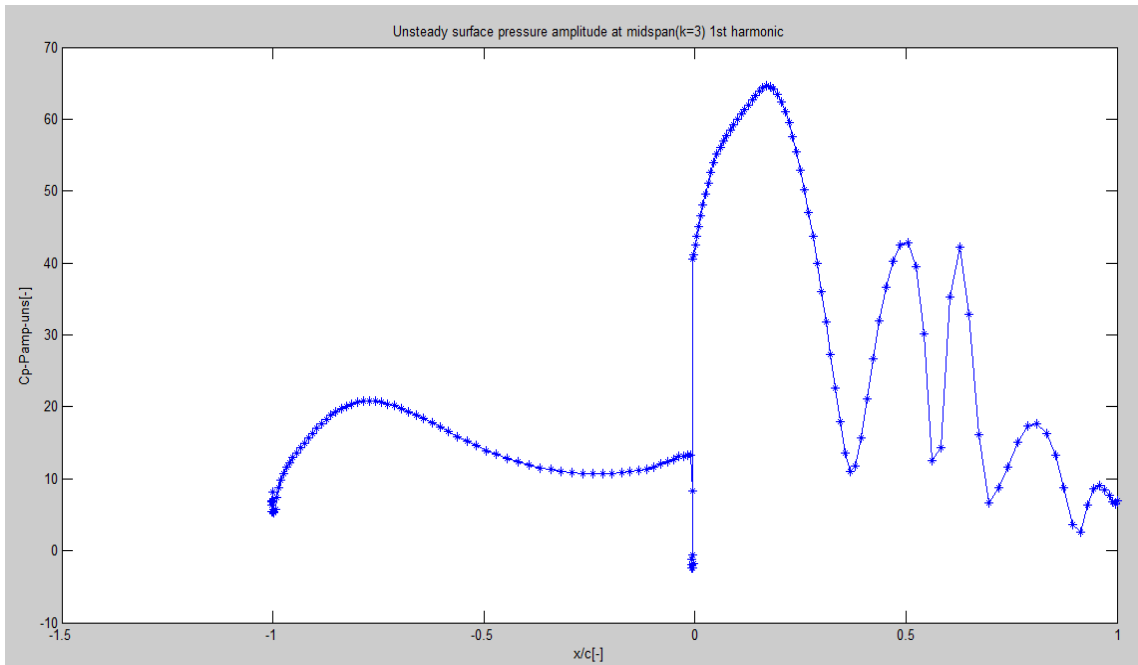


Figure 8.25: Unsteady surface pressure 1<sup>st</sup> harmonic amplitude at midspan (k=3) for  $IBPA = 234^\circ$

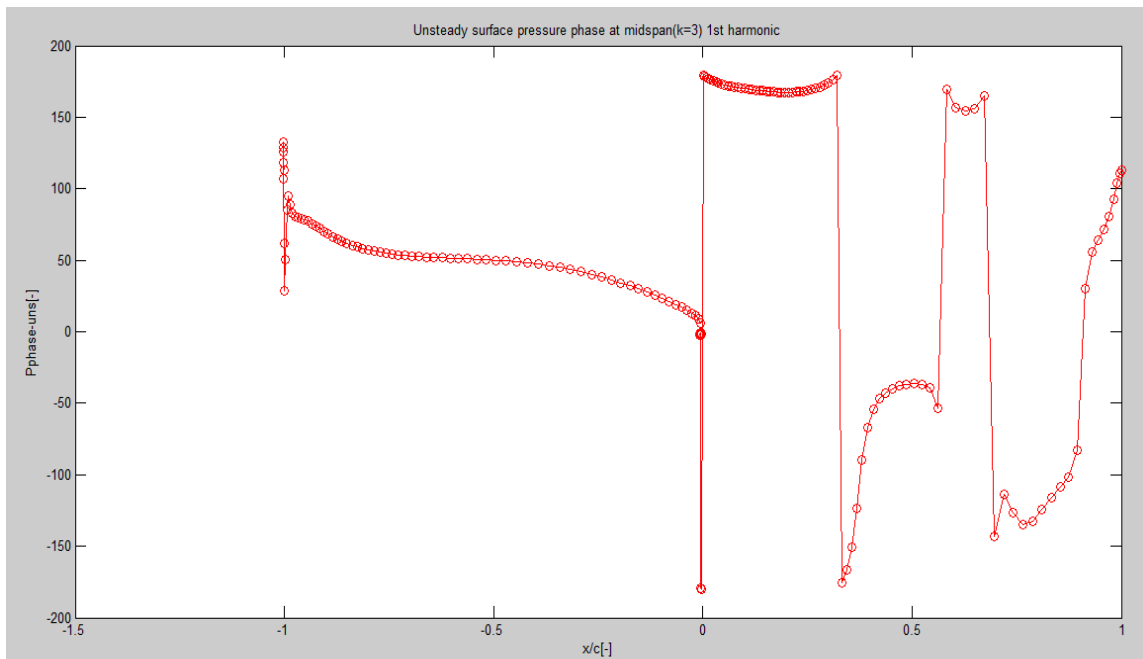


Figure 8.26: Unsteady surface pressure 1<sup>st</sup> harmonic phase at midspan (k=3) for  $IBPA = 234^\circ$

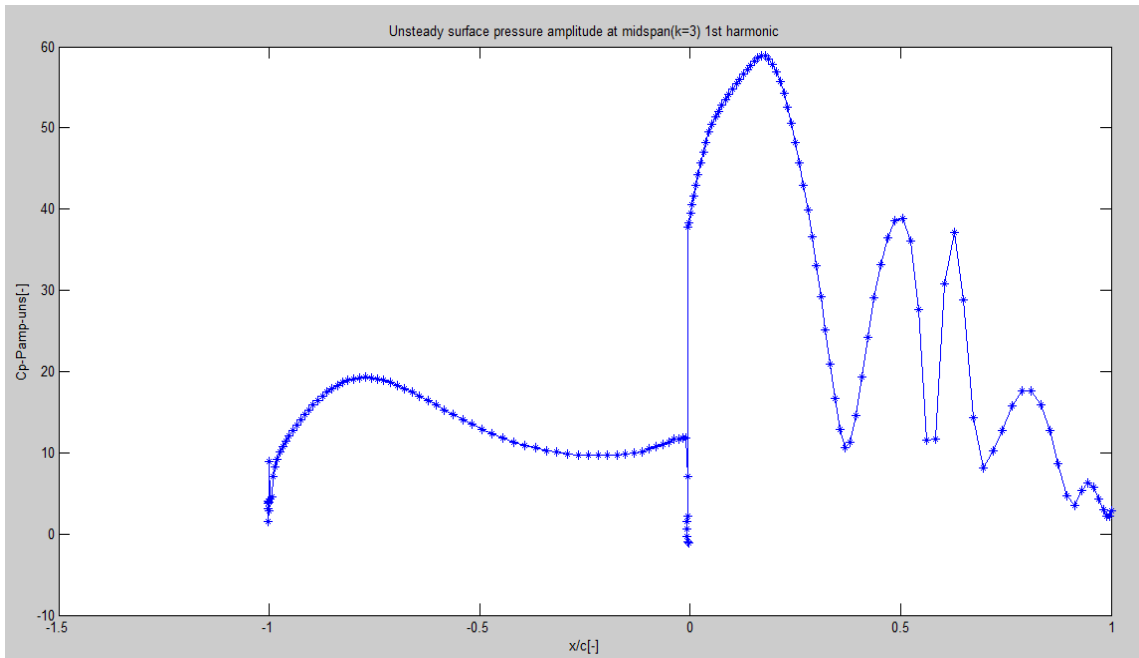


Figure 8.27: Unsteady surface pressure 1<sup>st</sup> harmonic amplitude at midspan (k=3) for  $IBPA = 252^\circ$

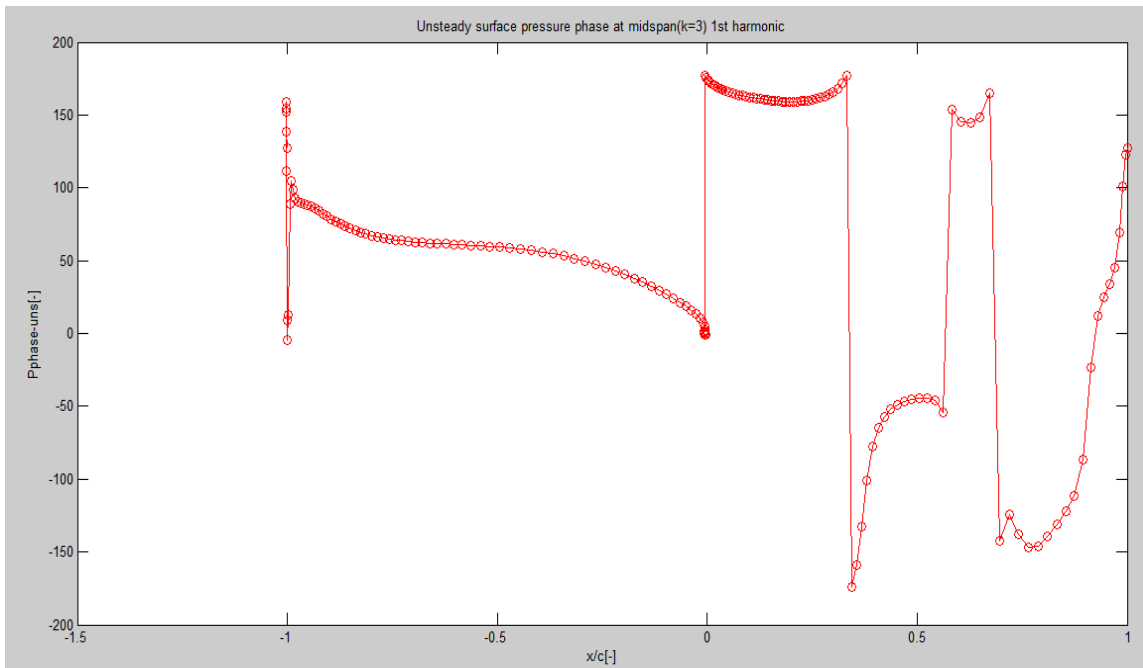


Figure 8.28: Unsteady surface pressure 1<sup>st</sup> harmonic phase at midspan (k=3) for

$$IBPA = 252^\circ$$

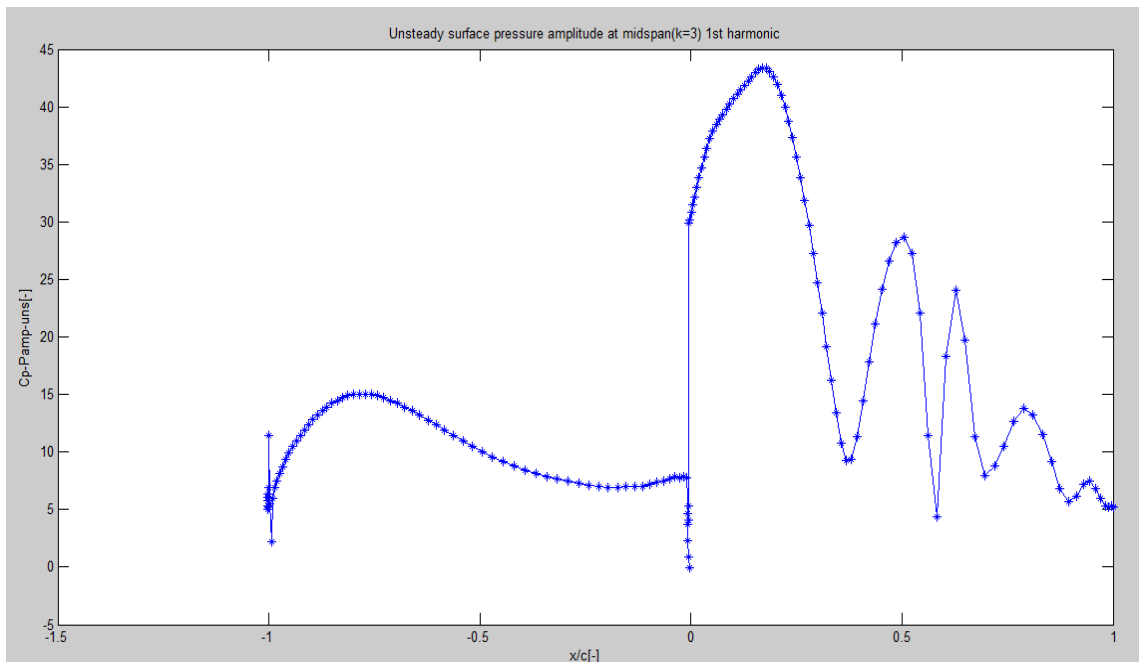


Figure 8.29: Unsteady surface pressure 1<sup>st</sup> harmonic amplitude at midspan ( $k=3$ ) for  $IBPA = 288^\circ$

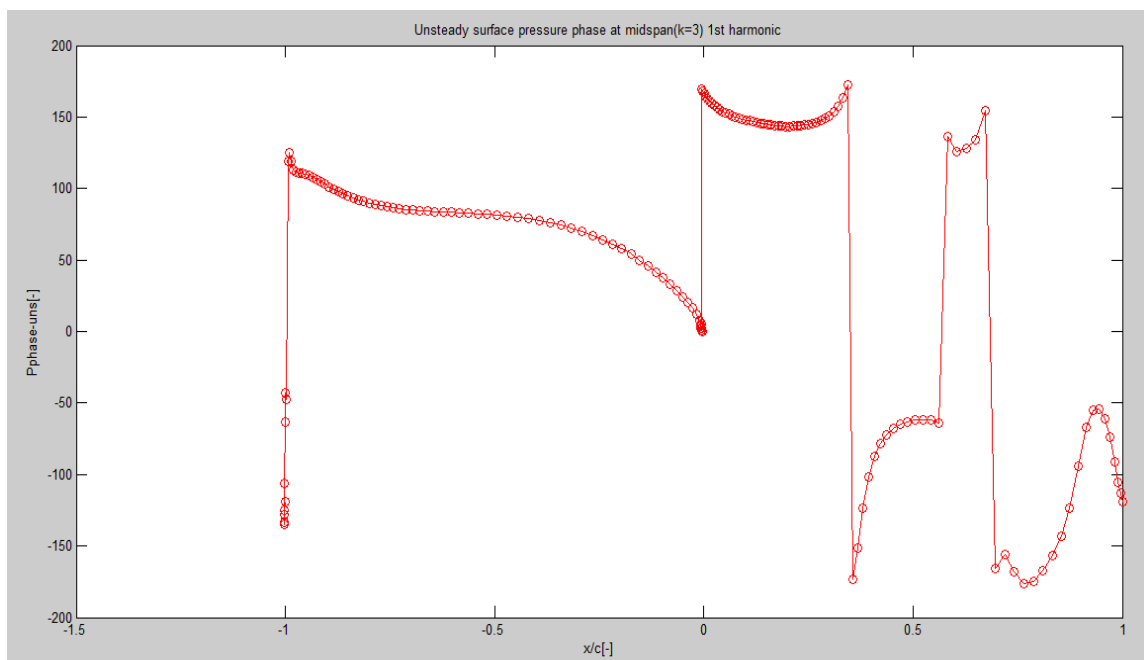


Figure 8.30: Unsteady surface pressure 1<sup>st</sup> harmonic phase at midspan ( $k=3$ ) for  $IBPA = 288^\circ$

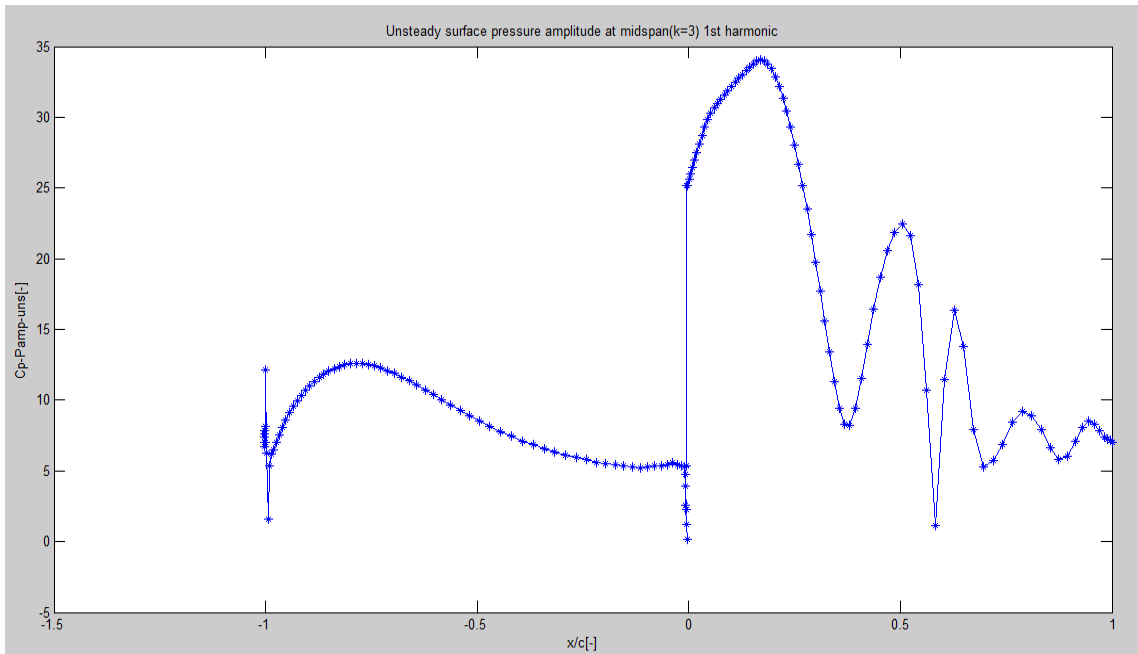


Figure 8.31: Unsteady surface pressure 1<sup>st</sup> harmonic amplitude at midspan (k=3) for  $IBPA = 306^\circ$

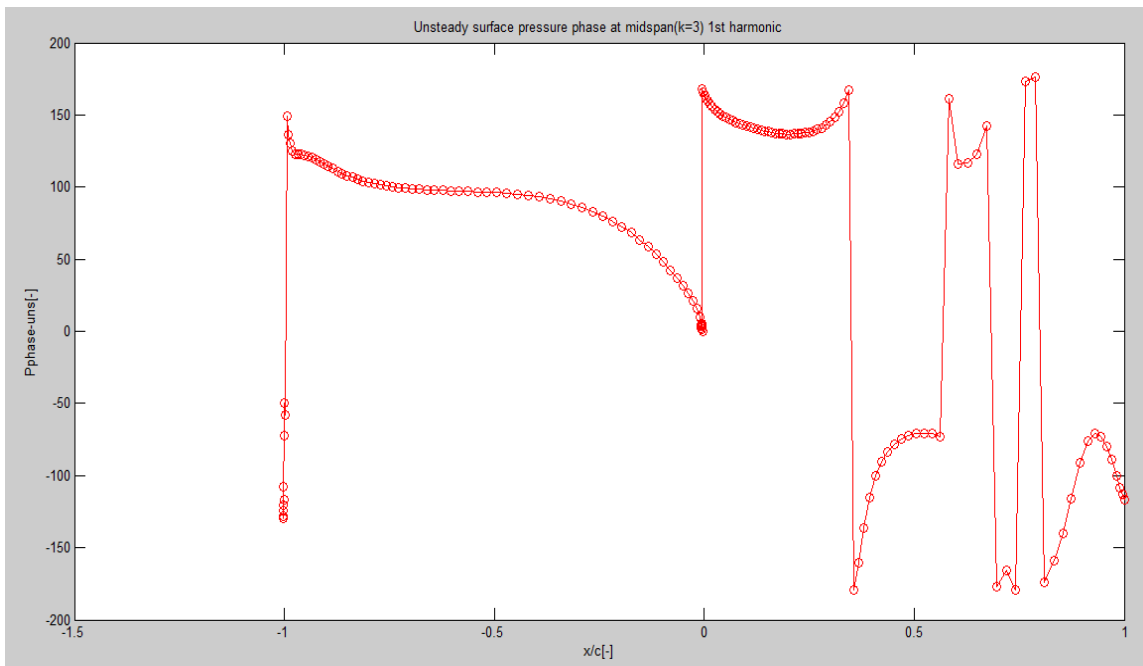


Figure 8.32: Unsteady surface pressure 1<sup>st</sup> harmonic phase at midspan (k=3) for  $IBPA = 306^\circ$

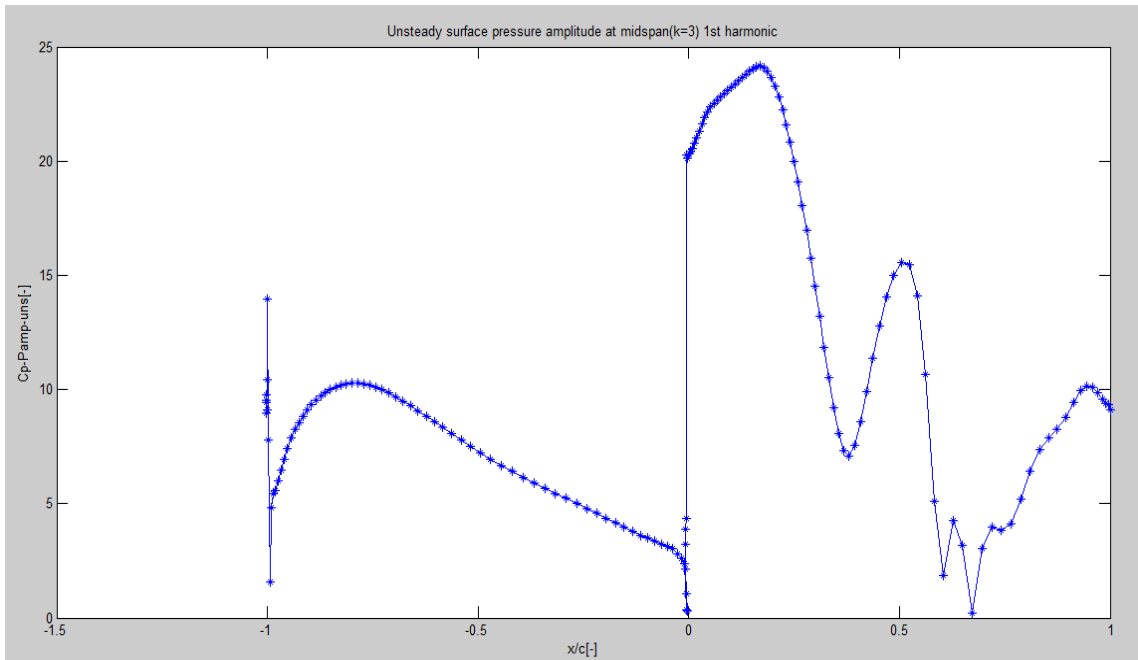


Figure 8.33: Unsteady surface pressure 1<sup>st</sup> harmonic amplitude at midspan (k=3) for  $IBPA = 324^\circ$

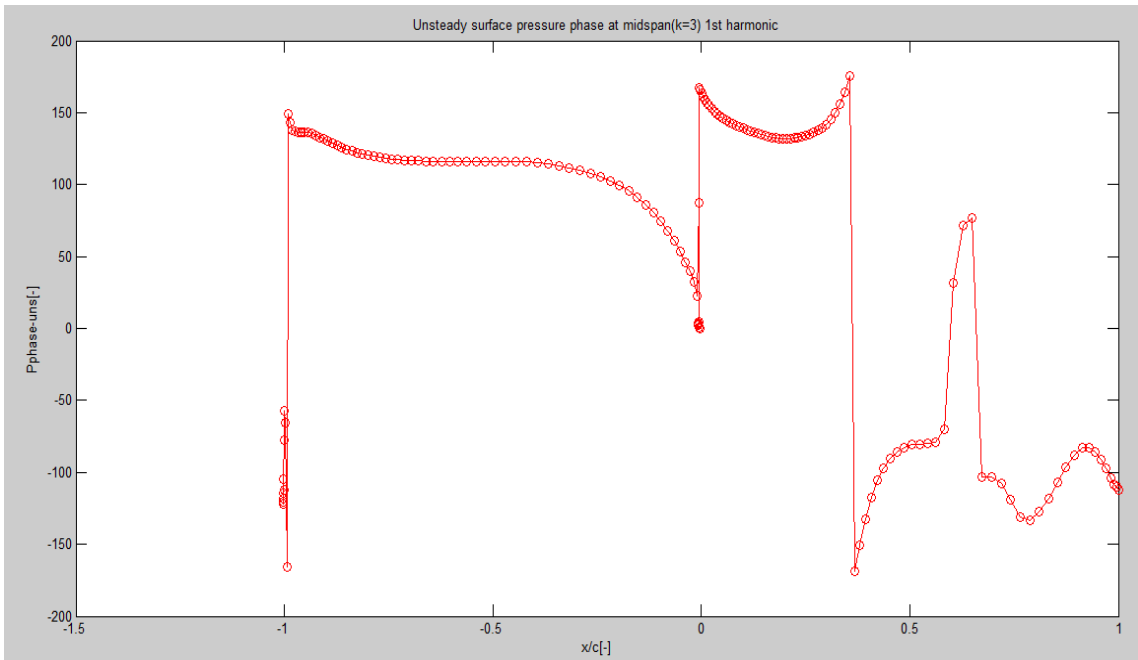


Figure 8.34: Unsteady surface pressure 1<sup>st</sup> harmonic phase at midspan (k=3) for  $IBPA = 324^\circ$

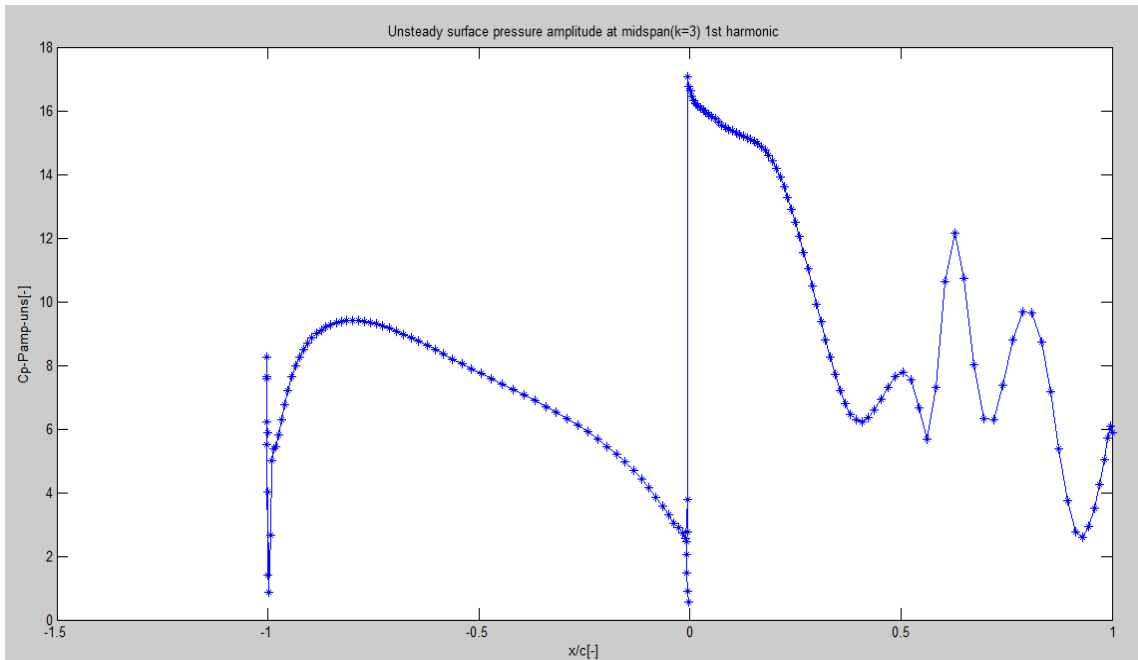


Figure 8.35: Unsteady surface pressure 1<sup>st</sup> harmonic amplitude at midspan (k=3) for  $IBPA = 342^\circ$

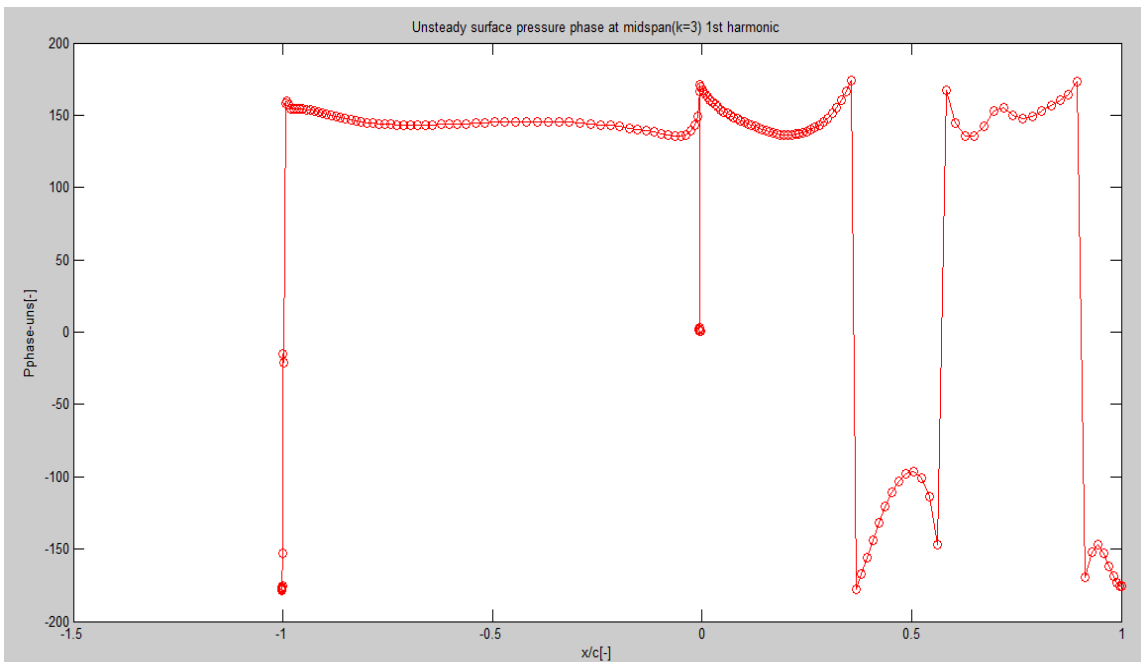


Figure 8.36: Unsteady surface pressure 1<sup>st</sup> harmonic phase at midspan (k=3) for  $IBPA = 342^\circ$

## B Matlab Codes

### generalized\_force.m (Calculate the generalized force)

```
% Initiation
clear all;close all;clc
load ('input.mat');
load ('uns_dis.mat');
load ('output_t1.mat');
load ('output_t2.mat');
load ('output_t3.mat');
load ('output_t4.mat');
load ('output_t5.mat');
load ('output_t6.mat');
load ('output_t7.mat');
Lambda=1.4;
f=139.7;
MGS=1.0;
% Construct output array
output(:,1)=output_t1;
output(:,2)=output_t2;
output(:,3)=output_t3;
output(:,4)=output_t4;
output(:,5)=output_t5;
output(:,6)=output_t6;
output(:,7)=output_t7;
% Construct x & x_uns array, and calculate the bending amplitude
for blk=1:3
    if blk==2
        for k=1:5
            for j=1:25
                for i=1:161
                    x(i,j,k,blk)=input(10+17*25*5*3+(k-1)*161*25+(j-1)*161+i);
                    y(i,j,k,blk)=input(10+17*25*5*3+161*25*5+(k-1)*161*25+(j-1)*161+i);
                    z(i,j,k,blk)=input(10+17*25*5*3+161*25*5*2+(k-1)*161*25+(j-1)*161+i);
                    x_uns(i,j,k,blk)=uns_dis(10+17*25*5*3+(k-1)*161*25+(j-1)*161+i);
```

```

        y_uns(i,j,k,blk)=uns_dis(10+17*25*5*3+161*25*5+(k-1)*161*25+(j-1)*161+i);
        z_uns(i,j,k,blk)=uns_dis(10+17*25*5*3+161*25*5*2+(k-1)*161*25+(j-1)*161+i);
        A_uns(i,j,k,blk)=sqrt(x_uns(i,j,k,blk)^2+y_uns(i,j,k,blk)^2);
    end
end
end
elseif blk==1
    for k=1:5
        for j=1:25
            for i=1:17
                x(i,j,k,blk)=input(10+(k-1)*17*25+(j-1)*17+i);
                y(i,j,k,blk)=input(10+17*25*5+(k-1)*17*25+(j-1)*17+i);
                z(i,j,k,blk)=input(10+17*25*5*2+(k-1)*17*25+(j-1)*17+i);
                x_uns(i,j,k,blk)=uns_dis(10+(k-1)*17*25+(j-1)*17);
                y_uns(i,j,k,blk)=uns_dis(10+17*25*5+(k-1)*17*25+(j-1)*17+i);
                z_uns(i,j,k,blk)=uns_dis(10+17*25*5*2+(k-1)*17*25+(j-1)*17+i);
                A_uns(i,j,k,blk)=sqrt(x_uns(i,j,k,blk)^2+y_uns(i,j,k,blk)^2);
            end
        end
    end
end
else
    for k=1:5
        for j=1:25
            for i=1:17
                x(i,j,k,blk)=input(10+17*25*5*3+161*25*5*3+(k-1)*17*25+(j-1)*17+i);
                y(i,j,k,blk)=input(10+17*25*5*3+161*25*5*3+17*25*5+(k-1)*17*25+(j-1)*17+i);
                z(i,j,k,blk)=input(10+17*25*5*3+161*25*5*3+17*25*5*2+(k-1)*17*25+(j-1)*17+i);
                x_uns(i,j,k,blk)=uns_dis(10+17*25*5*3+161*25*5*3+(k-1)*17*25+(j-1)*17+i);
                y_uns(i,j,k,blk)=uns_dis(10+17*25*5*3+161*25*5*3+17*25*5+(k-1)*17*25+(j-1)*17+i);
                z_uns(i,j,k,blk)=uns_dis(10+17*25*5*3+161*25*5*3+17*25*5*2+(k-1)*17*25+(j-1)*17+i);
                A_uns(i,j,k,blk)=sqrt(x_uns(i,j,k,blk)^2+y_uns(i,j,k,blk)^2);
            end
        end
    end
end
end
end
end
end

```

```

% Construct conservative variables(rho,rhou,rhov,rhow,rhoE) array
for tl=1:7
    for blk=1:3
        if blk==2
            for k=1:5
                for j=1:25
                    for i=1:161
                        rho(i,j,k,blk,tl)=output(10+4+17*25*5*5+4+(k-1)*161*25+(j-1)*161+i,1,tl);
                        rhou(i,j,k,blk,tl)=output(10+4+17*25*5*5+4+161*25*5+(k-1)*161*25+(j-1)*161+i,1,tl);
                        rhov(i,j,k,blk,tl)=output(10+4+17*25*5*5+4+161*25*5*2+(k-1)*161*25+(j-1)*161+i,1,tl);
                        rhow(i,j,k,blk,tl)=output(10+4+17*25*5*5+4+161*25*5*3+(k-1)*161*25+(j-1)*161+i,1,tl);
                        rhoE(i,j,k,blk,tl)=output(10+4+17*25*5*5+4+161*25*5*4+(k-1)*161*25+(j-1)*161+i,1,tl);
                    end
                end
            end
        elseif blk==1
            for k=1:5
                for j=1:25
                    for i=1:17
                        rho(i,j,k,blk,tl)=output(10+4+(k-1)*17*25+(j-1)*17+i,1,tl);
                        rhou(i,j,k,blk,tl)=output(10+4+17*25*5+(k-1)*17*25+(j-1)*17+i,1,tl);
                        rhov(i,j,k,blk,tl)=output(10+4+17*25*5*2+(k-1)*17*25+(j-1)*17+i,1,tl);
                        rhow(i,j,k,blk,tl)=output(10+4+17*25*5*3+(k-1)*17*25+(j-1)*17+i,1,tl);
                        rhoE(i,j,k,blk,tl)=output(10+4+17*25*5*4+(k-1)*17*25+(j-1)*17+i,1,tl);
                    end
                end
            end
        else
            for k=1:5
                for j=1:25
                    for i=1:17
                        rho(i,j,k,blk,tl)=output(10+4+17*25*5*5+4+161*25*5*5+4+(k-1)*17*25+(j-1)*17+i,1,tl);
                        rhou(i,j,k,blk,tl)=output(10+4+17*25*5*5+4+161*25*5*5+4+17*25*5+(k-1)*17*25+(j-1)*17+i,1,tl);
                        rhov(i,j,k,blk,tl)=output(10+4+17*25*5*5+4+161*25*5*5+4+17*25*5*2+(k-1)*17*25+(j-1)*17+i,1,tl);
                        rhow(i,j,k,blk,tl)=output(10+4+17*25*5*5+4+161*25*5*5+4+17*25*5*3+(k-1)*17*25+(j-1)*17+i,1,tl);
                        rhoE(i,j,k,blk,tl)=output(10+4+17*25*5*5+4+161*25*5*5+4+17*25*5*4+(k-1)*17*25+(j-1)*17+i,1,tl);
                    end
                end
            end
        end
    end
end

```

```

        end
    end
end
end
end
end
end
% Calculate rho,u,v,w,E separately
u=rhou./rho;
v=rhov./rho;
w=rhow./rho;
E=rhoE./rho;
% Extract coordinates of leading edge & trailing edge and convert x to x/c
for k=1:5
    indxmin(k)=find(x(:,1,k,2)==min(x(:,1,k,2)));
    xmin(k)=x(indxmin(k),1,k,2);
    ymin(k)=y(indxmin(k),1,k,2);
    zmin(k)=z(indxmin(k),1,k,2);
    indxmax(k)=find(x(:,1,k,2)==max(x(:,1,k,2)));
    xmax(k)=x(indxmax(k),1,k,2);
    ymax(k)=y(indxmax(k),1,k,2);
    zmax(k)=z(indxmax(k),1,k,2);
    alphac(k)=atan((ymax(k)-ymin(k))/(xmax(k)-xmin(k)));
    alphax(:,k)=atan((y(:,1,k,2)-ymin(k))./(x(:,1,k,2)-xmin(k)));
    alpha(:,k)=alphac(k)-alphax(:,k);
    scord(:,k)=sqrt((x(:,1,k,2)-xmin(k)).^2+(y(:,1,k,2)-ymin(k)).^2);
    pscord(:,k)=scord(:,k).*cos(alpha(:,k));
    chord(k)=sqrt((xmax(k)-xmin(k)).^2+(ymax(k)-ymin(k)).^2);
    pchord(:,k)=pscord(:,k)./chord(k);
end
% Calculate the pressure
P=(Lambda-1)*rho.*(E-0.5*(u.^2+v.^2+w.^2));
% Construct Inverse Fourier Transform E matrix
omega1=2*pi*f;
omega2=2*omega1;
omega3=3*omega1;
T=2*pi/omega1;

```

```

t1=0;
t2=T/7;
t3=2*t2;
t4=3*t2;
t5=4*t2;
t6=5*t2;
t7=6*t2;
t=[t1 t2 t3 t4 t5 t6 t7];
for i=1:7
    Ematrix(i,:)=1*cos(omega1*t(i)) cos(omega2*t(i)) cos(omega3*t(i)) sin(omega1*t(i)) sin(omega2*t(i)) sin(omega3*t(i));
end
for i=1:7
    for j=1:7
        if abs(Ematrix(i,j))<=1e-10
            Ematrix(i,j)=0;
        end
    end
end
end
% Covert surface pressure from time domain to frequency domain
for blk=1:3
    if blk==2
        for k=1:5
            for j=1:25
                for i=1:161
                    Pfreq(i,j,k,blk,:)=Ematrix \ reshape(P(i,j,k,blk,:),[],1);
                    Pstd(i,j,k,blk)=Pfreq(i,j,k,blk,1);
                    Cp_std(i,j,k,blk)=(Pstd(i,j,k,blk)-2.0818)/(2.1419-2.0818);
                    A1(i,j,k,blk)=Pfreq(i,j,k,blk,2);
                    B1(i,j,k,blk)=Pfreq(i,j,k,blk,5);
                    Pamp_uns(i,j,k,blk)=sqrt(A1(i,j,k,blk)^2+B1(i,j,k,blk)^2);
                    Cp_Real_uns(i,j,k,blk)=A1(i,j,k,blk)/(0.0601*(A_uns(i,j,k,blk)/chord(k)));
                    Cp_Imag_uns(i,j,k,blk)=B1(i,j,k,blk)/(0.0601*(A_uns(i,j,k,blk)/chord(k)));
                    Cp_Pamp_uns(i,j,k,blk)=Pamp_uns(i,j,k,blk)/(0.0601*(A_uns(i,j,k,blk)/chord(k)));
                    Pphase_uns(i,j,k,blk)=atan2(B1(i,j,k,blk),A1(i,j,k,blk));
                    Pphase_uns(i,j,k,blk)=Pphase_uns(i,j,k,blk)*180/pi;
                end
            end
        end
    end
end

```

```

end
end
else
for k=1:5
for j=1:25
for i=1:17
Pfreq(i,j,k,blk,:)=Ematrix\reshape(P(i,j,k,blk,:),[],1);
Pstd(i,j,k,blk)=Pfreq(i,j,k,blk,1);
Cp_std(i,j,k,blk)=(Pstd(i,j,k,blk)-2.0818)/(2.1419-2.0818);
A1(i,j,k,blk)=-Pfreq(i,j,k,blk,2);
B1(i,j,k,blk)=-Pfreq(i,j,k,blk,5);
Pamp_uns(i,j,k,blk)=sqrt(A1(i,j,k,blk)^2+B1(i,j,k,blk)^2);
Cp_Real_uns(i,j,k,blk)=A1(i,j,k,blk)/(0.0601*(A_uns(i,j,k,blk)/chord(k)));
Cp_Imag_uns(i,j,k,blk)=B1(i,j,k,blk)/(0.0601*(A_uns(i,j,k,blk)/chord(k)));
Cp_Pamp_uns(i,j,k,blk)=Pamp_uns(i,j,k,blk)/(0.0601*(A_uns(i,j,k,blk)/chord(k)));
Pphase_uns(i,j,k,blk)=atan2(B1(i,j,k,blk),A1(i,j,k,blk));
Pphase_uns(i,j,k,blk)=Pphase_uns(i,j,k,blk)*180/pi;
end
end
end
end
end
end
% Calculate non-dimentionalized Generalized Force
GF=zeros(7,3);
Area=AR(x,y,z,x_uns,y_uns,z_uns);
j=1;
for tl=1:7
for blk=1:3
if blk==2
for k=1:4
for i=1:160
FG_AVG(i,j,k,blk)=0.25*(x_uns(i,j,k,blk)+x_uns(i+1,j,k,blk)+x_uns(i+1,j,k+1,blk)+x_uns(i,j,k+1,blk));
GG_AVG(i,j,k,blk)=0.25*(y_uns(i,j,k,blk)+y_uns(i+1,j,k,blk)+y_uns(i+1,j,k+1,blk)+y_uns(i,j,k+1,blk));
HG_AVG(i,j,k,blk)=0.25*(z_uns(i,j,k,blk)+z_uns(i+1,j,k,blk)+z_uns(i+1,j,k+1,blk)+z_uns(i,j,k+1,blk));
P_AVG(i,j,k,blk,tl)=0.25*(P(i,j,k,blk,tl)+P(i+1,j,k,blk,tl)+P(i+1,j,k+1,blk,tl)+P(i,j,k+1,blk,tl));
Aj0x(i,j,k,blk,tl)=Area(i,j,k,blk,tl,4);

```

```

    Aj0y(i,j,k,blk,tl)=Area(i,j,k,blk,tl,5);
    Aj0z(i,j,k,blk,tl)=Area(i,j,k,blk,tl,6);
    GF(tl,blk)=GF(tl,blk)-
P_AVG(i,j,k,blk,tl)*(Aj0x(i,j,k,blk,tl)*FG_AVG(i,j,k,blk)+Aj0y(i,j,k,blk,tl)*GG_AVG(i,j,k,blk)+Aj0z(i,j,k,blk,tl)*HG_AVG(i,j,k
,blk));
    end
    end
else
    for k=1:4
        for i=1:16
            FG_AVG(i,j,k,blk)=0.25*(x_uns(i,j,k,blk)+x_uns(i+1,j,k,blk)+x_uns(i+1,j,k+1,blk)+x_uns(i,j,k+1,blk));
            GG_AVG(i,j,k,blk)=0.25*(y_uns(i,j,k,blk)+y_uns(i+1,j,k,blk)+y_uns(i+1,j,k+1,blk)+y_uns(i,j,k+1,blk));
            HG_AVG(i,j,k,blk)=0.25*(z_uns(i,j,k,blk)+z_uns(i+1,j,k,blk)+z_uns(i+1,j,k+1,blk)+z_uns(i,j,k+1,blk));
            P_AVG(i,j,k,blk,tl)=0.25*(P(i,j,k,blk,tl)+P(i+1,j,k,blk,tl)+P(i+1,j,k+1,blk,tl)+P(i,j,k+1,blk,tl));
            Aj0x(i,j,k,blk,tl)=Area(i,j,k,blk,tl,4);
            Aj0y(i,j,k,blk,tl)=Area(i,j,k,blk,tl,5);
            Aj0z(i,j,k,blk,tl)=Area(i,j,k,blk,tl,6);
            GF(tl,blk)=GF(tl,blk)-
P_AVG(i,j,k,blk,tl)*(Aj0x(i,j,k,blk,tl)*FG_AVG(i,j,k,blk)+Aj0y(i,j,k,blk,tl)*GG_AVG(i,j,k,blk)+Aj0z(i,j,k,blk,tl)*HG_AVG(i,j,k
,blk));
        end
    end
end
end
end
% Use Inverse Fourier Transform to convert Generalized force to frequency
% domain
for blk=1:3
    GFfreq(:,blk)=Ematrix \ GF(:,blk);
end
GF_std=GFfreq(1,2);
GF_Real=GFfreq(2,2)
GF_Imag=GFfreq(5,2)

```

## AR.m (Calculate the element area)

```
function Area = AR(x,y,z,x_uns,y_uns,z_uns)
%UNTITLED Summary of this function goes here
% Detailed explanation goes here
MGS=1.0;
f=139.7;
omega=2*pi*f;
T=2*pi/omega;
for tl=1:7
    x_global(:, :, :, tl)=x+MGS*x_uns*cos(omega*(T/7*(tl-1)));
    y_global(:, :, :, tl)=y+MGS*y_uns*cos(omega*(T/7*(tl-1)));
    z_global(:, :, :, tl)=z+MGS*z_uns*cos(omega*(T/7*(tl-1)));
    for blk=1:3
        if blk==2
            for k=1:4
                for j=1:24
                    for i=1:160
                        x000=x_global(i,j,k,blk,tl);
                        y000=y_global(i,j,k,blk,tl);
                        z000=z_global(i,j,k,blk,tl);
                        x001=x_global(i,j,k+1,blk,tl);
                        y001=y_global(i,j,k+1,blk,tl);
                        z001=z_global(i,j,k+1,blk,tl);
                        x010=x_global(i,j+1,k,blk,tl);
                        y010=y_global(i,j+1,k,blk,tl);
                        z010=z_global(i,j+1,k,blk,tl);
                        x011=x_global(i,j+1,k+1,blk,tl);
                        y011=y_global(i,j+1,k+1,blk,tl);
                        z011=z_global(i,j+1,k+1,blk,tl);
                        x100=x_global(i+1,j,k,blk,tl);
                        y100=y_global(i+1,j,k,blk,tl);
                        z100=z_global(i+1,j,k,blk,tl);
                        x101=x_global(i+1,j,k+1,blk,tl);
                        y101=y_global(i+1,j,k+1,blk,tl);
                        z101=z_global(i+1,j,k+1,blk,tl);
```

```

x110=x_global(i+1,j+1,k,blk,tl);
y110=y_global(i+1,j+1,k,blk,tl);
z110=z_global(i+1,j+1,k,blk,tl);
x111=x_global(i+1,j+1,k+1,blk,tl);
y111=y_global(i+1,j+1,k+1,blk,tl);
z111=z_global(i+1,j+1,k+1,blk,tl);

```

```

Ai0x=-0.5*((y001-y010)*(z011-z000)-(y011-y000)*(z001-z010));
Ai0y=0.5*((x001-x010)*(z011-z000)-(x011-x000)*(z001-z010));
Ai0z=-0.5*((x001-x010)*(y011-y000)-(x011-x000)*(y001-y010));
Aj0x=-0.5*((y101-y000)*(z001-z100)-(y001-y100)*(z101-z000));
Aj0y=0.5*((x101-x000)*(z001-z100)-(x001-x100)*(z101-z000));
Aj0z=-0.5*((x101-x000)*(y001-y100)-(x001-x100)*(y101-y000));
Ak0x=0.5*((y110-y000)*(z010-z100)-(y010-y100)*(z110-z000));
Ak0y=-0.5*((x110-x000)*(z010-z100)-(x010-x100)*(z110-z000));
Ak0z=0.5*((x110-x000)*(y010-y100)-(x010-x100)*(y110-y000));
Ai1x=-0.5*((y101-y110)*(z111-z100)-(y111-y100)*(z101-z110));
Ai1y=0.5*((x101-x110)*(z111-z100)-(x111-x100)*(z101-z110));
Ai1z=-0.5*((x101-x110)*(y111-y100)-(x111-x100)*(y101-y110));
Aj1x=-0.5*((y111-y010)*(z011-z110)-(y011-y110)*(z111-z010));
Aj1y=0.5*((x111-x010)*(z011-z110)-(x011-x110)*(z111-z010));
Aj1z=-0.5*((x111-x010)*(y011-y110)-(x011-x110)*(y111-y010));
Ak1x=0.5*((y111-y001)*(z011-z101)-(y011-y101)*(z111-z001));
Ak1y=-0.5*((x111-x001)*(z011-z101)-(x011-x101)*(z111-z001));
Ak1z=0.5*((x111-x001)*(y011-y101)-(x011-x101)*(y111-y001));

```

```

Area(i,j,k,blk,tl,1)=Ai0x;
Area(i,j,k,blk,tl,2)=Ai0y;
Area(i,j,k,blk,tl,3)=Ai0z;
Area(i,j,k,blk,tl,4)=Aj0x;
Area(i,j,k,blk,tl,5)=Aj0y;
Area(i,j,k,blk,tl,6)=Aj0z;
Area(i,j,k,blk,tl,7)=Ak0x;
Area(i,j,k,blk,tl,8)=Ak0y;
Area(i,j,k,blk,tl,9)=Ak0z;
Area(i,j,k,blk,tl,10)=Ai1x;

```

```

        Area(i,j,k,blk,tl,11)=Ai1y;
        Area(i,j,k,blk,tl,12)=Ai1z;
        Area(i,j,k,blk,tl,13)=Aj1x;
        Area(i,j,k,blk,tl,14)=Aj1y;
        Area(i,j,k,blk,tl,15)=Aj1z;
        Area(i,j,k,blk,tl,16)=Ak1x;
        Area(i,j,k,blk,tl,17)=Ak1y;
        Area(i,j,k,blk,tl,18)=Ak1z;
    end
end
end
else
    for k=1:4
        for j=1:24
            for i=1:16
                x000=x_global(i,j,k,blk,tl);
                y000=y_global(i,j,k,blk,tl);
                z000=z_global(i,j,k,blk,tl);
                x001=x_global(i,j,k+1,blk,tl);
                y001=y_global(i,j,k+1,blk,tl);
                z001=z_global(i,j,k+1,blk,tl);
                x010=x_global(i,j+1,k,blk,tl);
                y010=y_global(i,j+1,k,blk,tl);
                z010=z_global(i,j+1,k,blk,tl);
                x011=x_global(i,j+1,k+1,blk,tl);
                y011=y_global(i,j+1,k+1,blk,tl);
                z011=z_global(i,j+1,k+1,blk,tl);
                x100=x_global(i+1,j,k,blk,tl);
                y100=y_global(i+1,j,k,blk,tl);
                z100=z_global(i+1,j,k,blk,tl);
                x101=x_global(i+1,j,k+1,blk,tl);
                y101=y_global(i+1,j,k+1,blk,tl);
                z101=z_global(i+1,j,k+1,blk,tl);
                x110=x_global(i+1,j+1,k,blk,tl);
                y110=y_global(i+1,j+1,k,blk,tl);
                z110=z_global(i+1,j+1,k,blk,tl);
            end
        end
    end
end

```

```

x111=x_global(i+1,j+1,k+1,blk,tl);
y111=y_global(i+1,j+1,k+1,blk,tl);
z111=z_global(i+1,j+1,k+1,blk,tl);

```

```

Ai0x=-0.5*((y001-y010)*(z011-z000)-(y011-y000)*(z001-z010));
Ai0y=0.5*((x001-x010)*(z011-z000)-(x011-x000)*(z001-z010));
Ai0z=-0.5*((x001-x010)*(y011-y000)-(x011-x000)*(y001-y010));
Aj0x=-0.5*((y101-y000)*(z001-z100)-(y001-y100)*(z101-z000));
Aj0y=0.5*((x101-x000)*(z001-z100)-(x001-x100)*(z101-z000));
Aj0z=-0.5*((x101-x000)*(y001-y100)-(x001-x100)*(y101-y000));
Ak0x=0.5*((y110-y000)*(z010-z100)-(y010-y100)*(z110-z000));
Ak0y=-0.5*((x110-x000)*(z010-z100)-(x010-x100)*(z110-z000));
Ak0z=0.5*((x110-x000)*(y010-y100)-(x010-x100)*(y110-y000));
Ai1x=-0.5*((y101-y110)*(z111-z100)-(y111-y100)*(z101-z110));
Ai1y=0.5*((x101-x110)*(z111-z100)-(x111-x100)*(z101-z110));
Ai1z=-0.5*((x101-x110)*(y111-y100)-(x111-x100)*(y101-y110));
Aj1x=-0.5*((y111-y010)*(z011-z110)-(y011-y110)*(z111-z010));
Aj1y=0.5*((x111-x010)*(z011-z110)-(x011-x110)*(z111-z010));
Aj1z=-0.5*((x111-x010)*(y011-y110)-(x011-x110)*(y111-y010));
Ak1x=0.5*((y111-y001)*(z011-z101)-(y011-y101)*(z111-z001));
Ak1y=-0.5*((x111-x001)*(z011-z101)-(x011-x101)*(z111-z001));
Ak1z=0.5*((x111-x001)*(y011-y101)-(x011-x101)*(y111-y001));

```

```

Area(i,j,k,blk,tl,1)=Ai0x;
Area(i,j,k,blk,tl,2)=Ai0y;
Area(i,j,k,blk,tl,3)=Ai0z;
Area(i,j,k,blk,tl,4)=Aj0x;
Area(i,j,k,blk,tl,5)=Aj0y;
Area(i,j,k,blk,tl,6)=Aj0z;
Area(i,j,k,blk,tl,7)=Ak0x;
Area(i,j,k,blk,tl,8)=Ak0y;
Area(i,j,k,blk,tl,9)=Ak0z;
Area(i,j,k,blk,tl,10)=Ai1x;
Area(i,j,k,blk,tl,11)=Ai1y;
Area(i,j,k,blk,tl,12)=Ai1z;
Area(i,j,k,blk,tl,13)=Aj1x;

```

```
Area(i,j,k,blk,tl,14)=Aj1y;  
Area(i,j,k,blk,tl,15)=Aj1z;  
Area(i,j,k,blk,tl,16)=Ak1x;  
Area(i,j,k,blk,tl,17)=Ak1y;  
Area(i,j,k,blk,tl,18)=Ak1z;  
end  
end  
end  
end  
end  
end  
end
```

## References

- Anderson, D.A., Tannehill, J.C. and Pletcher, R.H. (1984): Computational fluid mechanics and heat transfer.
- Bendiksen, O. O., Kielb, R. E. and Hall K. C. (2010): Turbomachinery Aeroelasticity.
- Bolcs, A. and Fransson, T. H. (1986): Aeroelasticity in Turbomachines: Comparison of Theoretical and Experimental Cascade Results
- Buffum, D. H. (1995): Blade Row Interaction Effects on Flutter and Forced Response. In: AIAA, SAE, ASME, and ASEE, Joint Propulsion Conference and Exhibit, 29th, Monterey, CA; UNITED STATES. pp. 18.
- Castanier, M. P. and Pierre, C. (2006): Modeling Analysis of Mistuned Bladed Disk Vibration: Status and emerging directions. In: Journal of Propulsion and Power, volume 22(2): pp. 284-396.
- Collar, AR (1946): The Expanding Domain of Aeroelasticity. In: Journal of the Royal Aeronautical Society, volume 50(428): pp. 613-636.
- Dowell, E.H. and Clark, R. (2004): A Modern Course in Aeroelasticity. Kluwer Academic Pub.
- Dowell, E.H. and Tang, D. (2002): Nonlinear Aeroelasticity and Unsteady Aerodynamics. In: AIAA Journal, volume 40: pp. 1697-1707. 10.2514/2.1853.
- Ekici, K., Hall, K. C. and Kielb, R. E. (2007): MUSTANG HB v1.2 Installation and User Manual. Department of Mechanical Engineering and Material Science, Duke University, Durham, NC, 27708-0300.
- Fransson, T. H. and Verdon, J. M. (1991): Standard Configurations for Unsteady Flow through Vibrating Axial-Flow Turbomachine-Cascades. Technical Report, Department of Energy Technology, KTH, Stockholm, Sweden.
- Hall, K. C., Ekici, K. and Voytovych, D. M. (2006): Multistage Coupling for Unsteady Flows in Turbomachinery. In: Unsteady aerodynamics, aeroacoustics and aeroelasticity of turbomachines, pp. 217-229

- Hall, K. C., Thomas, J.P. and Clark, W.S. (2002): Computation Of Unsteady Nonlinear Flows In Cascades Using A Harmonic Balance Technique. In: AIAA journal, volume 40(5): pp. 878-886.
- Lane, F. (1956): System Mode Shapes in the Flutter of Compressor Blade Rows. In: Journal of the Aeronautical Sciences, volume 23(1): pp. 54-66.
- McBean, I., Hourigan, K., Thompson, M., Liu, F. (2005): Prediction of Flutter of Turbine Blades in a Transonic Annular Cascade. In: ASME Journal of Fluids Engineering, 127, November: pp. 1053–1058.
- Marshall, J. G. and Imregun, M. (1996): A Review of Aeroelasticity Methods with Emphasis on Turbomachinery Applications. In: Journal of Fluids and Structures, volume 10(3): pp. 237-267. ISSN 0889-9746.
- Meinzer, C. E. (2011): Numerical Investigation of Multi-Row Flutter Interaction with Wake Excitation, Master thesis, Department of Mechanical Engineering and Material Science, Duke University.
- Miyakozawa, T. (2008): Flutter and Forced Response of Turbomachinery with Frequency Mistuning and Aerodynamic Asymmetry. Ph.D. dissertation, Department of Mechanical Engineering and Material Science, Duke University.
- Oates, G.C. (1989): Aircraft propulsion systems technology and design. AIAA.
- Pinelli, L., Poli, F., Arnone, A., and Schipani, C. A. (2009): Time-Accurate 3D Method for Turbomachinery Blade Flutter Analysis. In: 12<sup>th</sup> ISUAAAT, London, UK. I12-S8-3.
- Platzer, M.F. and Carta, F.O. (1987): AGARD Manuel on Aeroelasticity in Axial-Flow Turbomachines. Volume 1: Unsteady Turbomachinery Aerodynamics. Technical Report, Advisory Group for Aerospace Research and Development
- Platzer, M.F. and Carta, F.O. (1988): AGARD manual on aeroelasticity in axial- flow turbomachines. Volume 2: Structural dynamics and aeroelasticity. Technical Report, Advisory Group for Aerospace Research and Development
- Shannon, JF (1945): Vibration Problems in Gas Turbines, Centrifugal and Axial Flow Compressors.

Silkowski, PD and Hall, KC (1998): A Coupled Mode Analysis Of Unsteady Multistage Flows In Turbomachinery. In: Journal of turbomachinery, volume 120(3): pp. 410-421.

Srinivasan, AV (1997): Flutter and Resonant Vibration Characteristics of Engine Blades. In: Journal of engineering for gas turbines and power, volume 119(4): pp. 742-775.

Witteck, D., Micallef, D., Wiedermann, A. and Mailach, R. (2012): Three-Dimensional Viscous Flutter Analysis of a Turbine Cascade in Supersonic Flow. JSASS Pub.